

A STUDY OF 13 POWERFUL CLASSICAL DOUBLE RADIO GALAXIES

P. KHARB, C. P. O’DEA, AND S. A. BAUM

Rochester Institute of Technology, 54 Lomb Memorial Drive, Rochester, NY 14623

R. A. DALY AND M. P. MORY

Department of Physics, Penn State University, Berks Campus, P.O. Box 7009, Reading, PA 19610

M. DONAHUE

Department of Physics and Astronomy, BPS Building, Michigan State University, East Lansing, MI 48824

AND

E. J. GUERRA

Department of Physics and Astronomy, Rowan University, 201 Mullica Hill Road, Glassboro, NJ 08028

Received 2006 September 21; accepted 2007 May 18

ABSTRACT

We have carried out an extensive study of a sample of 13 large, powerful Fanaroff-Riley type II radio galaxies with the Very Large Array in multiple configurations at 330 MHz and 1.4, 5, and 8 GHz. We present the total intensity, polarization, spectral index, and rotation measure maps of the sources. On the whole, the 13 FR II sources have symmetric structures with arm-length ratios close to unity, small misalignment angles, and low values of radio core prominence, suggesting that these radio galaxies lie close to the plane of the sky. We have revisited some well-known radio galaxy correlations using a large combined data set comprising our radio galaxies and others from the literature. We confirm that the hot spot size correlates with the core–hot spot distance. The hot spot spectral index is correlated with and flatter than the lobe spectral index, consistent with the assumptions of spectral aging models. Both the hot spot and lobe spectral index are correlated with redshift. The depolarization asymmetry in the lobes is not correlated with the radio core prominence or misalignment angle, which are statistical indicators of orientation. The “Liu-Pooley” correlation of lobe depolarization with the lobe spectral index is significant in our radio galaxy sample. Furthermore, the lobe with the steeper spectral index and greater depolarization is shorter and fatter. The arm-length ratio seems to be correlated with the misalignment angle between the two sides of the radio source and strongly anticorrelated with the axial ratio, consistent with environmental effects and/or a change in the outflow direction. In this sample, asymmetries in the local environments and/or motion of the outflow axis are likely to be more important than relativistic beaming effects.

Subject headings: galaxies: active — radio continuum: galaxies

Online material: extended figure sets

1. INTRODUCTION

Classical double radio galaxies are active galactic nuclei with regions of synchrotron-emitting plasma that can extend to thousands of kiloparsecs. These Fanaroff-Riley type II radio galaxies (Fanaroff & Riley 1974) are thought to be powered by narrow collimated jets, terminating in high surface brightness regions called “hot spots.” Regions of low surface brightness emission lying between the galaxy center and the hot spots, called radio bridges, are believed to be a result of the accumulation of relativistic particles accelerated at the hot spots over the lifetime of an FR II source that form a low-density cocoon around the jet (see Begelman et al. 1984 for a theoretical review). The ultimate motivation of our project is to study the radio bridges in FR II radio galaxies and do a spectral aging analysis. In this paper we present the first results of our study and describe the global properties of our FR II radio galaxy sample.

In order to comprehend the phenomenology of FR II galaxies, large samples of radio galaxies have hitherto been observed, yielding an extensive database of information. Results from arcsecond-scale radio observations of FR II radio galaxies have been presented by many authors, for example, Laing (1981), Leahy & Williams (1984), Alexander & Leahy (1987), Leahy et al. (1989), Pedelty et al. (1989), Garrington et al. (1991), Liu et al. (1992), Hardcastle

et al. (1998), Ishwara-Chandra et al. (2001), Goodlet et al. (2004), Gilbert et al. (2004), Mullin et al. (2006), and others. Previous studies of the radio bridges have included relatively low-resolution observations ($\sim 3''$ – $4''$) at 151 MHz and 1.4 GHz of the full bridge region (e.g., Leahy et al. 1989), while the higher resolution observations ($\sim 1''$) at 1.4, 5, and 15 GHz have sampled the bridge emission partially (e.g., Liu et al. 1992). However, to empirically address and understand the different physical processes that are important at different radio frequencies, physical locations, and stages of evolution of a source, both low-frequency radio data and high-resolution radio data are required.

To this end, we observed 13 FR II radio galaxies with the Very Large Array (VLA) in multiple configurations at 330 MHz, 1.4 GHz, 5 GHz, and 8 GHz. Here we present images of the total and polarized radio intensity, spectral index between 1.4 and 5 GHz, 0.3 and 1.4 GHz, and rotation measure between 1.4 and 5 GHz. Furthermore, we probe the relationship between different global characteristics of the radio galaxies by augmenting our data with additional galaxy data gleaned from the literature. We will subsequently refer to this extended, eclectic sample as the “combined” data set, while the 13 FR II galaxies will be referred to as such.

The paper is arranged as follows: the radio galaxy sample is described in § 2, while the observations and data reduction are

TABLE 1
THE SAMPLE OF FR II RADIO GALAXIES

Source (1)	IAU Name (2)	z (3)	S_{178} (Jy) (4)	$\log(P_{178})$ (W Hz ⁻¹) (5)	Scale (kpc arcsec ⁻¹) (6)	Θ , P.A. (arcsec, deg) (7)	LAS (arcsec) (8)	LAS (kpc) (9)	Reference (10)
3C 6.1	0013+790	0.8404	14.9	28.68	7.6	26.0, 27.3	31.5	241	9, 12
3C 13	0031+391	1.3510	13.1	29.14	8.5	28.6, 145.1	32.5	276	4, 8
3C 34	0107+315	0.6900	13.0	28.41	7.1	45.1, 82.9	48.7	346	9, 12
3C 41	0123+329	0.7940	11.6	28.51	7.5	23.8, 145.1	27.2	204	9, 12
3C 44	0128+061	0.6600	10.0	28.24	6.9	64.8, 12.8	72.0	502	7
3C 54	0152+435	0.8274	10.5	28.51	7.6	51.1, 23.6	60.2	458	1, 2
3C 114.....	0417+177	0.8150	8.2	28.38	7.6	53.2, 44.3	59.6	451	1, 6
3C 142.1	0528+064	0.4061	18.6	28.00	5.4	52.4, 130.1	55.5	299	7
3C 169.1	0647+452	0.6330	6.6	28.02	6.8	45.9*, 135.7*	53.6	367	9
3C 172	0659+253	0.5191	16.5	28.21	6.2	101.2, 16.6	109.0	676	5, 11
3C 441	2203+292	0.7070	13.7	28.45	7.2	33.3, 149.8	41.7	299	9, 12
3C 469.1	2352+796	1.3360	12.1	29.09	8.5	75.4, 171.1	84.1	712	2
3C 470	2356+437	1.6530	11.0	29.28	8.6	24.9, 37.9	29.8	255	3, 10

NOTES.—Cols. (1) and (2): Common and IAU names of the FR II radio galaxies. Col. (3): Redshifts were obtained from the NASA/IPAC Extragalactic Database (NED). Col. (4): Total flux density at 178 MHz in Jy on the Baars et al. (1977) scale taken from <http://www.3crr.dyn dns.org/cgi/database>; for 5 sources not listed in Laing et al. (1983) we used the 4C flux densities from Gower et al. (1967) multiplied by a factor of 1.09 to convert them to Baars et al. scale following Roger et al. (1973). Col. (5): Logarithm of the total luminosity at 178 MHz. Col. (6): Spatial scale in source corresponding to 1". Col. (7): Angular extent and position angle of the source, measured from the VLA A array 8 GHz maps using the brightest hot spot. The position angle is defined as counterclockwise from north. Asterisk (*) signifies that for 3C 169.1, the northern hot spot was not detected in the 8 GHz image—the 2.5" 5 GHz image was used instead to obtain the extent. Col. (8): Largest angular size measured from the ~2" image at 1.4 GHz. The AIPS task TVDIST was used to measure the entire radio extent (from hot spot to hot spot) of the source. Col. (9): Largest projected linear size of source estimated using values in cols. (7) and (9). Col. (10): References for previous observations (this is not an exhaustive list).

REFERENCES.—(1) MacDonald et al. 1968; (2) Longair 1975; (3) Riley & Pooley 1975; (4) Schilizzi et al. 1982; (5) Strom & Conway 1985; (6) Strom et al. 1990; (7) Bogers et al. 1994; (8) Law-Green et al. 1995; (9) Neff et al. 1995; (10) Best et al. 1997a; (11) Gilbert et al. 2004; (12) Mullin et al. 2006.

discussed in § 3; the source properties are presented in § 4; the correlations are discussed in § 5; and the summary and conclusions follow in § 6. This paper is the first in a series of four papers. In Paper II, we will present the results of the spectral aging analysis, lobe propagation velocities, pressures, beam powers, and ambient gas densities. In Paper III, we will describe the use of these sources for cosmological studies and present the results for a large sample of powerful FR II galaxies. Finally, in Paper IV, we will present a detailed analysis of the radio bridge structure of the sources.

Throughout the paper, we have adopted the cosmology in which $H_0 = 71 \text{ km s}^{-1} \text{ Mpc}^{-1}$, $\Omega_m = 0.27$ and $\Omega_\Lambda = 0.73$. The spectral indices α are defined such that the flux density S_ν at frequency ν , is $S_\nu \propto \nu^{-\alpha}$.

2. THE SAMPLE

The FR II radio galaxies considered for the present study are part of the 3CR sample of radio sources (Bennett 1962). The 13 sources that are a focus of this paper were those for which we were allocated observing time, from a larger sample of powerful FR II sources selected for an extensive study of their radio bridges. These sources satisfy the following criteria: their radio power at 178 MHz is greater than $10^{28} \text{ W Hz}^{-1}$; their angular sizes are larger than $27''$, they span the redshift range of $z \simeq 0.4\text{--}1.65$ and are classified as narrow-line FR II radio galaxies (Hes et al. 1996; Jackson & Rawlings 1997). The largest source in our sample, 3C 172, has an angular extent of $\geq 100''$, which corresponds to a linear size of $\simeq 680 \text{ kpc}$. The large angular sizes ensure that the radio lobes span several beam widths, crucial for the spectral aging study, which will be presented in Paper II. A compilation of the basic parameters for each source is given in Table 1.

3. OBSERVATIONS AND DATA ANALYSIS

The 13 FR II radio galaxies were observed with the A, B, C, and D array configurations of the VLA (Napier et al. 1983) be-

tween 2002 November and 2003 November at 330 MHz, 1.4, 4.8, and 8.4 GHz. Table 2 provides a summary of the VLA observations. The sources were observed in a ~10 minute snapshot mode. In order to be able to extract possible radio frequency interference, which can become significant at low frequencies, the 330 MHz data were observed in the spectral-channel mode. While making the radio maps at 330 MHz, only the central 80% of the spectral channels were averaged. Scheduling constraints resulted in some sources not being observed at some frequencies. For a few sources, VLA archival data existed at one or more frequencies and these were not observed (see Table 3). We used the VLA archival data for these sources, the program IDs of which are listed in Table 3.

The data were reduced using the standard calibration and reduction procedures in the Astronomical Image Processing System (AIPS). 3C 48 was used as the primary flux density calibrator for the experiment. The instrumental polarization and electric vector position angles were calibrated using 0217+738 and 3C 138, respectively. The polarization data at 1.4 GHz were corrected for ionospheric Faraday rotation using the total electron content maps available at CDDIS data archive¹ in the AIPS task TECOR.

After the initial amplitude and phase calibration using the calibrators, the source data were phase and amplitude self-calibrated (Schwab 1980) and imaged in an iterative manner, using the tasks CALIB and IMAGR. In order to improve the UV coverage, we combined the self-calibrated data sets from the various configurations at a given frequency using the AIPS task DBCON and performed additional rounds of phase and amplitude self-calibration on the combined data sets. Table 2 lists the largest angular scale structure that can be imaged well in single-snapshot observations with the different VLA configurations. A quick comparison with the angular sizes of our 13 FR II galaxies listed in Table 1 demonstrates that our sources were imaged reasonably well when the

¹ See <ftp://cddisa.gsfc.nasa.gov>.

TABLE 2
SUMMARY OF VLA OBSERVATIONS

Obs. Date (1)	Configuration (2)	Band (3)	Frequency (MHz) (4)	Bandwidth (MHz) (5)	Integration Time (minutes) (6)	θ_{LAS} (arcsec) (7)
2003 Jun 17	A	P	327.5, 321.5	3.1	8	85.0
		L	1344.9, 1664.9	25	11	19.0
		X	8435.1, 8485.1	25	11	3.5
2003 Nov 29	B	L	1344.9, 1664.9	25	9	60.0
		C	4885.1, 4835.1	50	9	18.0
2002 Nov 4	C	P	327.5, 321.5	3.1	6	2100.0
		L	1344.9, 1664.9	25	9	450.0
		C	4885.1, 4835.1	50	9	150.0
2003 Apr 11	D	C	4885.1, 4835.1	50	8	150.0

NOTES.—Col. (1): Observing date. Col. (2): VLA Array configuration. Col. (3): Observing frequency band. Cols. (4) and (5): Central frequency for the 2 constituent IFs in each frequency band, and bandwidth, respectively. Col. (6): Integration time in minutes. Col. (7): The largest angular scale structure which can be imaged reasonably well in single-snapshot observations (see The VLA Observational Status Summary). The *P*-band data were observed in the spectral-line mode.

data from A, B, and C arrays were combined at the *L* band, B, C, and D arrays were combined at the *C* band, and A and C arrays were combined at the *P* band.

The polarization maps were made by combining the Stokes *Q* and *U* images using the AIPS task COMB. We split our *L*-band data into its constituent Intermediate frequencies (IFs, see Table 2) and used the lower frequency, i.e., 1345 MHz and the averaged *C*-band data at 4860 MHz, to create the spectral index maps using the AIPS task COMB. For the rotation measure maps, we used the three frequencies, 1345, 1665, and 4860 MHz, in the AIPS task RM. When archival data were used, we could still combine the respective *L*-band IFs, which sometimes differed from our frequencies, to the closest frequency in our data. For 3C 142.1 we noticed *RM* flips across the southern lobe, which were a result of the $n\pi$ ambiguity in the polarization angles. We therefore used a guess (integrated) *RM* value of $+84 \text{ rad m}^{-2}$ (Simard-Normandin et al. 1981) in the AIPS task RM for the rotation measure map of 3C 142.1.

We typically recover 95% to 100% of the integrated flux density listed in Kuehr et al. (1996) at the *L* and *C* bands. For 3C 441 and 3C 469.1, between 85% and 90% of the integrated flux density is recovered in our maps. The registration of images for the spectral index and rotation measure maps is better than $\sim 0.1''$. By blanking values in the task COMB, the polarization intensity,

polarization angle and fractional polarization maps were restricted to have $S/N > 3$, output errors less than $\approx 10^\circ$ and 10%, respectively. No Ricean bias correction (e.g., Wardle & Kronberg 1974) was made to the polarized intensity. The mean rotation measure and the dispersion/spread in rotation measure, σ_{RM} was obtained by using the AIPS task IMEAN.

4. RESULTS

The final maps at 1.4 and 5 GHz, restored with a $2.0''$ or $2.5''$ circular Gaussian beam, the 330 MHz maps restored with a $5.0''$ circular Gaussian beam, and the 8 GHz maps with insets for the hot spots, are presented in Figures 13–49. The total intensity contours are superimposed with the fractional polarization vectors. 1.4 GHz polarization maps could not be made for 3C 6.1 and 3C 41 because their respective (archival) data sets did not include scans of a polarization angle calibrator. The dynamic range in the final images (defined as peak brightness/rms noise) varies from 7400 to 400, being typically greater than 3000. The 1.4–5 GHz spectral index and *RM* maps were made at a resolution of $2.0''$ or $2.5''$, while the 0.3–1.4 GHz spectral index maps were made at a resolution of $5.0''$.

The high-resolution A array 8 GHz images reveal the details of the hot spot structure. Most sources show the presence of multiple hot spots. These could be due to the plasma beam moving

TABLE 3
OBSERVATION SUMMARY OF THE SAMPLE

Source	A/P	A/L	A/X	B/L	B/C	C/P	C/L	C/C	D/C
3C 6.1	AH291	AP380	...	N	AJ111	...
3C 13	N	AA150	AL322	N	N	VAH54
3C 34	N	AG247	AL322	N	N	N	N	N	AP380
3C 41	AH291	AP380	...	AG220
3C 44	N	N	N	N	N	N	N	N	...
3C 54	N	N	N	N	N	N	N	N	N
3C 114	N	N	N	N	N	N	N	N	N
3C 142.1	N	AH480	N	N	N	N	N	N	N
3C 169.1	N	N	N	N	N	N	N	N	N
3C 172	N	N	AP361	N	N	N	N	N	N
3C 441	N	N	N	N	N	N	N	N	N
3C 469.1	N	N	N	N	N	N	N	N	N
3C 470	AB917	N	AL322	N	N	AH343	...

NOTES.—(N) New observations made by us (Program ID-AO170); (AH291, AA150, etc.) program IDs for archival observations; (ellipses) no observations due to scheduling constraints.

TABLE 4
PROPERTIES OF HOT SPOTS

Source (1)	Morph. (2)	Comp. (3)	Size (θ''_{maj} , θ''_{min} , P.A.) (4)	I_{peak}^8 (mJy beam $^{-1}$) (5)	$I_{\text{peak}}^{1.4}$ (mJy beam $^{-1}$) (6)	I_{peak}^5 (mJy beam $^{-1}$) (7)	$\alpha_{1.4}^5$ (2 $''$) (8)	$\alpha_{1.4}^{0.3}$ (5 $''$) (9)
3C 6.1	Multiple	NH1	0.39, 0.25, 134.69	46.7	1217.0	435.1	0.85	...
		NH2	0.33, 0.24, 99.64	26.4
		SH	0.49, 0.44, 77.25	17.1	891.5	324.9	0.83	...
3C 13	Single	NH	0.23, 0.09, 130.63	57.2	1066.0	270.1	1.13	0.86
		SH	0.22, 0.17, 161.55	17.8	499.3	91.6	1.41	1.09
3C 34	Multiple	EH1	0.56, 0.47, 169.23	2.7	145.7	57.8	0.82	0.74
		EH2	1.24, 0.87, 9.55	1.8
		WH	0.39, 0.26, 179.44	1.5	38.3	15.0	0.86	0.70
3C 41	Multiple	NH	0.46, 0.22, 20.53	8.0	446.9	178.8	0.73	...
		SH1	0.42, 0.32, 120.46	33.2	981.8	502.1	0.55	...
		SH2	0.33, 0.23, 76.19	33.3
3C 44	Multiple	NH1	0.30, 0.22, 68.96	4.3	198.5	63.2	0.89*	0.91
		NH2	0.45, 0.28, 153.92	2.7
		SH	0.26, 0.17, 44.66	22.7	429.9	137.1	0.89*	0.81
3C 54	Single	NH	0.19, 0.16, 31.99	7.5	289.6	105.7	0.79*	0.74
		SH	0.18, 0.10, 28.75	68.9	592.6	228.9	0.73*	0.71
3C 114.....	Single	NH	0.33, 0.23, 104.83	2.2	108.5	37.5	0.82*	0.79
		SH	0.30, 0.15, 142.78	6.7	206.5	69.7	0.83*	0.81
3C 142.1	Single	NH	0.42, 0.17, 41.45	1.8	376.8	123.3	0.89	0.83
		SH	0.46, 0.25, 67.12	1.6	183.3	66.3	0.77	0.82
3C 169.1	Single	NH	49.6	18.2	0.80*	0.82
		SH	0.41, 0.23, 50.37	1.6	153.8	57.5	0.77*	0.77
3C 172	Multiple	NH1	0.99, 0.76, 174.07	3.4	394.5	119.8	0.93*	0.73
		NH2	0.72, 0.49, 42.54	1.9
		NH3	1.22, 0.42, 173.03	1.9
		NH4	0.79, 0.58, 66.43	1.64
		SH	0.35, 0.23, 124.89	11.1	486.2	153.9	0.89*	0.71
3C 441	Single	NH	0.29, 0.18, 98.68	31.9	424.8	186.1	0.64*	0.84
		SH	0.30, 0.17, 110.01	1.6	226.8	68.6	0.95*	0.98
3C 469.1	Multiple	NH1	0.44, 0.30, 1.12	2.6	549.7	131.5	1.13*	0.97
		NH2	1.16, 0.77, 67.51	1.4
		NH3	0.69, 0.26, 27.40	1.8
		SH1	0.80, 0.53, 60.79	4.2	395.6	114.8	0.96*	0.83
		SH2	0.42, 0.33, 28.95	2.2
3C 470	Multiple	NH	0.30, 0.13, 15.80	20.1	156.5	62.5	0.71	0.59
		SH1	0.22, 0.18, 57.18	38.6	1201.0	318.7	1.02	0.91
		SH2	0.91, 0.43, 33.06	17.0

NOTES.—Hot spot properties derived from the high-resolution 8 GHz images. Col. (2): Morphology of the hot spot region—whether single or multiple hot spots. Col. (3): NH, SH, EH, and WH denote northern, southern, eastern, and western hot spots, respectively; NH2 is the second brightest hot spot, and so on. Col. (4): Major and minor axes of the deconvolved hot spot sizes, estimated using AIPS task JMFIT. Col. (5): Peak surface brightness of hot spot at 8 GHz derived by JMFIT. Cols. (6) and (7): Peak surface brightness of hot spot at 1.4 and 5.0 GHz, respectively, from the 2.0 $''$ (or 2.5 $''$) total intensity map (data from both IFs were averaged). Cols. (8) and (9): Hot spot spectral index between 1.4 and 5 GHz and between \sim 330 MHz and 1.4 GHz, respectively. Asterisks (*) indicate that maps at 2.5 $''$ were used.

about along the cavity wall as in the “dentist’s drill” model (Scheuer 1982). Alternatively, multiple hot spots could be interpreted as “splatter-spots” formed by a jet with a variable direction (Williams & Gull 1985). Table 4 presents selected characteristics of the hot spots in our 13 FR II galaxies. Our high-resolution 8 GHz images reveal that the brightest hot spots at either end, which probably are the current acceleration sites of particles, lie roughly along a line connecting the hot spots and the core for each of the 13 sources.

Radio bridges are detected in all but two sample radio galaxies, viz., 3C 13 and 3C 470. These sources are the most luminous and the most distant in our sample and are likely to be strongly affected by $(1+z)^4$ surface brightness dimming. Therefore, more sensitive observations are required to detect the radio bridges in these sources. The spectral index maps show a gradual steepening of the radio spectra away from the hot spots with some spectral index variations superimposed, in agreement with previous studies (e.g., Myers & Spangler 1985; Alexander 1987; Alexander &

Leahy 1987). Some quantitative estimates of the radio lobe properties are tabulated in Table 5.

The majority of the sources exhibit a regular bridge structure, with some distortions becoming apparent at very low surface brightness. We have classified distortions using the radio morphology classification of Leahy & Williams (1984): Type 1 (hereafter LW1) morphology describes a bridge with no distortions but a marked decrease in the bridge surface brightness toward the center; Type 2 (hereafter LW2) describes a bridge that bends away from the central galaxy only on one side; Type 3 (LW3) describes a bridge that bends away from the galaxy on both sides in a cross shape; Type 4 (LW4) is a radio bridge that bends on both sides in the same direction away from the host galaxy; and Type 5 (LW5) describes a bridge that is continuous across the galaxy that is displaced toward the steepest edge of the radio source. The bridge types are presented in Table 5.

The radio core prominence (R_c) is the ratio of the flux density from the radio core (S_{core}) to the extended radio lobe emission (S_{ext}).

TABLE 5
PROPERTIES OF THE RADIO LOBES

Source (1)	$\Theta_{N,S}$ (arcsec, arcsec) (2)	Q (3)	ζ (deg) (4)	$\langle RM \rangle$ (rad m ⁻²) (5)	σ_{RM} (rad m ⁻²) (6)	DP N, S (7)	Error in DP (8)	$\alpha_{5}^{1,4}$ N, S (9)	$\alpha_{1.4}^{0,3}$ N, S (10)	AR N, S (11)	$\log(l/l_{ej})$ (12)
3C 6.1	13.89, 12.09	1.15	2.4	1.121, 1.123	...	2.74, 2.65	...
3C 13*	16.46, 12.11	1.36	3.4	60.49, ...	28.04, ...	0.73, 1.43	0.37, 0.5	1.278, 1.539	0.983, 1.121
3C 34†	23.98, 21.10	1.14	3.0	-62.30, -63.16	19.13, 7.73	0.91, 0.75	0.07, 0.15	1.281, 1.311	0.955, 0.942	4.79, 3.81	-0.056
3C 41	12.53, 11.32	1.11	1.5	0.996, 1.095	...	3.21, 2.68	-0.044
3C 44	40.15, 24.69	1.63	5.9	4.01, 14.60	11.93, 31.23	1.79, 1.00	0.25, 0.19	1.294, 1.451	0.876, 1.172	7.55, 5.82	...
3C 54	26.59, 24.71	1.07	8.9	-78.95, -70.15	3.90, 14.11	1.27, 1.23	0.36, 0.40	1.093, 1.161	0.919, 1.030	3.69, 4.08	-0.032
3C 114	25.43, 27.73	1.09	0.1	-2.10, -6.50	12.70, 17.80	0.39, 0.59	0.27, 0.01	1.267, 1.247	1.031, 1.205	4.32, 4.68	0.037
3C 142.1	18.30, 34.14	1.87	3.4	83.02, 85.01	19.03, 12.16	0.62, 0.94	0.13, 0.17	1.179, 1.018	0.886, 0.752	1.98, 5.20	...
3C 169.1	19.19, 27.69	1.44	14.6	9.22, 11.29	9.63, 15.40	0.99, 0.89	0.07, 0.08	1.057, 1.105	0.888, 0.876	2.05, 3.39	...
3C 172	47.33, 53.49	1.13	7.8	25.87, 1.72	13.68, 34.55	1.09, 1.54	0.07, 0.50	0.859, 0.772	0.753, 0.770	4.29, 5.14	...
3C 441*	9.67, 23.66	2.45	4.8	75.05, 68.23	9.97, 16.23	0.44, 0.76	0.02, 0.35	1.129, 1.176	1.002, 1.024	1.78, 4.41	-0.389
3C 469.1	36.44, 38.99	1.07	2.1	19.60, 8.99	14.70, 16.34	1.26, 1.09	0.12, 0.07	1.280, 1.262	1.277, 0.994	7.30, 6.41	0.028
3C 470	14.36, 10.54	1.36	3.7	..., -7.68	..., 32.10	..., 1.23	..., 0.5	0.708, 1.118	0.670, 0.920	...,

NOTES.—Col. (1): Source names. Col. (2): Angular extent of source from the hot spot to the radio core, for the northern and the southern side, respectively, obtained using the high-resolution 8 GHz maps. Sources with an asterisk (*) in col. (1) did not show a radio core in the 8 GHz image—host galaxy positions for 3C 13 and 3C 441 were obtained from McCarthy et al. (1997) and Fermi et al. (1997), respectively. Col. (3): Arm-length ratio, derived by taking the ratio of the two angular extents listed in col. (2). Col. (4): Misalignment angle in degrees, derived by taking the difference between position angles obtained for both sides of the source. Col. (5): Mean value of rotation measure (RM) for the northern and the southern side of the source, respectively. Col. (6): Dispersion in RM for the radio lobes. Col. (7): Depolarization parameter for the northern and southern lobes, respectively. A higher value of DP implies lower lobe depolarization. Col. (8): Error in depolarization estimated by taking a difference in the DP obtained by the C band and the two IFs in the L band, respectively. Col. (9): Average spectral index between 1.4 and 5 GHz, for the northern and southern lobes, respectively. Col. (10): Average lobe spectral index between 330 MHz and 1.4 GHz. Col. (11): Axial ratio for both the radio lobes. “N, S” stands for the northern and southern side of source. Col. (12): Logarithm of the arm-length ratio of the jet to the counterjet side. Double dagger (‡) signifies that for 3C 34, all the estimates are for the eastern and western lobe, respectively.

In the rest frame of the source, $R_c = (S_{\text{core}}/S_{\text{ext}})(1+z)^{\alpha_{\text{core}}-\alpha_{\text{ext}}}$, where z is the redshift of the source and α is the spectral index, assumed to be 0 and 1 for the core and extended emission, respectively. Due to Doppler beaming effects in the radio core (which is the unresolved base of the relativistic jet), R_c can be used as a statistical indicator of beaming and therefore orientation (Kapahi & Saikia 1982; Orr & Browne 1982). We have derived R_c using the radio core flux densities from the high-resolution 8 GHz maps (where the core is clearly delineated) and lobe flux densities from the 1.4 GHz maps (see Table 6). The lobe flux density is primarily all the extended radio emission minus the radio core and therefore includes the emission from the hot spots and jets. We find that the core prominence in our 13 FR II radio galaxies is small— R_c varies from 4.7×10^{-5} to 0.0029. This is consistent with the picture of these radio galaxies oriented close to the plane of the sky.

In Table 5 we have tabulated the mean values of the rotation measure (RM) and the corresponding dispersion (σ_{RM}) in the radio lobes of our 13 FR II galaxies. The mean RM was averaged over the two lobes. We have estimated the lobe depolarization parameter, DP , as $DP = m_l/m_h$, where m_l and m_h are the fractional polarizations at high and low frequencies, respectively. A higher value of DP implies lower depolarization. We created DP maps using the lower frequency L -band (IF1) and the C -band fractional polarization maps in AIPS using the task COMB. We used these maps to obtain a mean lobe DP by putting a box around each lobe (using AIPS verbs TVWIN and IMSTAT).

Note that a few sources have $DP > 1$. While the degree of polarization will occasionally increase with wavelength by chance due to Faraday effects, a close examination of our maps revealed that the high DP values were mostly obtained for those sources that showed polarization at 1.4 GHz only in the hot spots, where the systematic errors are expected to be the highest (e.g., 3C 13, 3C 54-North, 3C 469.1-North, 3C 470). Residual instrumental polarization errors and errors in the position-angle zero

point contribute to the total error in DP , especially since data from multiple configurations has been combined to get the polarization maps. The DP errors quoted in Table 5 were estimated by taking the difference in the DP obtained using the L band IF1 or IF2, and the C band, respectively. In our discussions of lobe depolarization we have therefore excluded all values of DP that are not estimated over the radio lobes.

The spectral index for the lobes in Table 5 was obtained by putting a box around the lobe in the spectral index map and getting a mean value. The hot spot spectral index was taken as the value in this map corresponding to the total intensity peak position at the hot spot. The arm-length ratio (Q) is the ratio of the angular extent of the larger radio lobe (core to hot spot) to the smaller. Another fundamental structural parameter is the axial ratio (AR), which is the ratio of the length to width of the radio lobe. The axial ratio was estimated for our radio galaxies following Leahy & Williams (1984)—the width was estimated of a section of the radio lobe roughly halfway between the hot spot and the core and defined as $2/\sqrt{3}$ times the FWHM of the Gaussian function fitted to the lobe surface brightness. We used the 1.4 GHz maps to get the widths and the 8 GHz maps to get accurate lengths. Table 5 presents the arm-length and axial ratios for the sample FR II radio galaxies.

5. RADIO GALAXY PROPERTIES AND CORRELATIONS

In the following sections we describe some global properties of the 13 FR II galaxies. Furthermore, we have revisited some well-known correlations for FR II radio galaxies using the “combined” data set comprising our sample galaxies and other FR II radio galaxies taken from the literature.

5.1. Data from the Literature

In order to understand the properties of FR II radio galaxies better, we augmented our data with similar radio galaxy data from the literature. The additional data come primarily from Leahy &

TABLE 6
PROPERTIES OF THE RADIO COMPONENTS

Source (1)	Frequency (GHz) (2)	S_ν (N lobe) (Jy) (3)	S_ν (S lobe) (Jy) (4)	S_ν (Core) (mJy) (5)	S_8 (Core) (mJy) (6)	Log R_c (7)	Lobe Type (8)	Jet-Side N, S (9)
3C 6.1	5.0	0.58	0.51	...	7.52	-2.90	LW1	..., ...
	1.4	1.75	1.49	10.14				
	0.33				
3C 13	5.0	0.29	0.11	...	<0.29 [†]	-4.19, ...
	1.4	1.25	0.61	...				
	0.33	4.56	3.16	...				
3C 34	5.0	0.22	0.16	1.91	0.69	-3.47	LW1	..., Jet
	1.4	0.69	0.54	3.23				
	0.33	2.79	2.38	...				
3C 41	5.0	0.44	0.86	...	2.38	-3.40	LW3	..., Jet ^a
	1.4	1.29	2.05	...				
	0.33				
3C 44	5.0	0.12	0.21	0.21	0.25	-3.94	LW1	..., ...
	1.4	0.48	0.79	...				
	0.33	1.58	3.11	...				
3C 54	5.0	0.21	0.36	...	0.36	-3.96	LW1	..., Jet
	1.4	0.65	1.11	...				
	0.33	2.03	3.66	...				
3C 114.....	5.0	0.13	0.14	12.38	5.41	-2.53	LW1	..., Jet?
	1.4	0.47	0.52	13.85				
	0.33	1.81	1.96	...				
3C 142.1	5.0	0.51	0.38	4.97	1.17	-3.57	LW1	..., ...
	1.4	1.88	1.28	7.95				
	0.33	6.89	3.97	...				
3C 169.1	5.0	0.14	0.21	0.81	0.75	-3.40	LW1	..., ...
	1.4	0.44	0.68	5.13				
	0.33	1.42	2.12	...				
3C 172	5.0	0.39	0.51	...	0.29	-4.18	LW5	..., ...
	1.4	1.29	1.55	...				
	0.33	3.79	4.14	...				
3C 441	5.0	0.55	0.23	...	<0.19 [†]	-4.32	LW3	Jet, ...
	1.4	1.65	0.79	...				
	0.33	5.60	3.25	...				
3C 469.1	5.0	0.19	0.22	4.08	1.58	-3.40	LW1	..., Jet?
	1.4	0.85	0.84	4.77				
	0.33	3.69	2.81	...				
3C 470	5.0	0.07	0.47	1.85	0.55	-3.97, ...
	1.4	0.17	1.75	...				
	0.33	0.42	6.43	...				

NOTES.—Cols. (1) and (2): Source name and the observing frequency in GHz, respectively. Cols. (3) and (4): Radio flux density in the northern and southern radio lobe, respectively, obtained by putting a box around the lobe region and using the AIPS verb IMSTAT. Col. (5): Radio core flux density in mJy. Col. (6–8) GHz core flux density in mJy. Dagger (†) indicates sources where core was not detected, an upper limit is derived assuming the core flux density to be below 5 times the rms noise level. Col. (7): Logarithm of the K -corrected radio core prominence parameter, defined as the ratio of (8 GHz) core to (1.4 GHz) lobe flux density (see § 4). Col. (8): Lobe type (see § 4). Col. (9): The side of the source on which a jetlike feature was observed. These tend to be faint and only visible in the gray-scale images (see Fig. 52). Tentative features are denoted with a question mark.

^a The jet in 3C 41 was noted by Mullin et al. (2006). Note that all estimates for 3C 34 are for the eastern and western lobe, respectively.

Williams (1984), Leahy et al. (1989), Pedelty et al. (1989), Garrington et al. (1991), Liu & Pooley (1991b), Hardcastle et al. (1998), and Goodlet et al. (2004) (see Table 7). We emphasize here that the data from the literature is inhomogeneous and chosen on the basis of the availability of the relevant physical parameters that we wished to examine in samples of (primarily 3C) FR II radio galaxies observed at a resolution of a few arcseconds. We have excluded radio-loud quasars from our analysis and restricted our selection to powerful FR II radio galaxies at a redshift-range matching our sample. The combined data set includes a few broad-line radio galaxies.

When not listed explicitly in the above-mentioned references, the arm-length ratios and misalignment angles were directly estimated (using a ruler and protractor) from the maps presented in

these papers. Therefore, the angle estimates have errors of the order of a few degrees, while the error in the arm-length ratios is expected to be less than 10%. When no radio core was observed in the maps, the position of the center of the host galaxy was used for the core position. The host galaxy positions were procured either from the papers directly or through the NASA/IPAC Extragalactic Database (NED).² For the 13 FR IIs, radio core prominence was derived using the 8 GHz core and 1.4 GHz lobe flux densities. If similar data were not available in the literature, we converted flux densities from other frequencies to 1.4 GHz for lobe and 8 GHz for core emission by assuming a spectral index of 1 and 0, respectively.

² See <http://nedwww.ipac.caltech.edu/>.

TABLE 7
DATA FROM THE LITERATURE

Source (1)	z (2)	Reference (3)
3C 16	0.405	Goodlet et al. (2004)
3C 20	0.174	Hardcastle et al. (1998)
3C 27	0.184	Leahy et al. (1989)
3C 42	0.395	Goodlet et al. (2004)
3C 46	0.437	Goodlet et al. (2004)
3C 52	0.285	Leahy & Williams (1984)
3C 55	0.734	Leahy et al. (1989)
3C 65	1.176	Goodlet et al. (2004)
3C 68.2	1.575	Leahy et al. (1989)
3C 79	0.2559	Hardcastle et al. (1998)
3C 98	0.0306	Hardcastle et al. (1998)
3C 103	0.330	Leahy & Williams (1984)
3C 105	0.089	Hardcastle et al. (1998)
3C 111	0.048	Leahy & Williams (1984)
3C 123	0.2177	Hardcastle et al. (1998)
3C 132	0.214	Hardcastle et al. (1998)
3C 135	0.1273	Hardcastle et al. (1998)
3C 136.1	0.064	Leahy & Williams (1984)
3C 139.2	...	Leahy & Williams (1984)
3C 153	0.2771	Hardcastle et al. (1998)
3C 165	0.295	Leahy & Williams (1984)
3C 166	0.244	Leahy & Williams (1984)
3C 171	0.2384	Hardcastle et al. (1998)
3C 173.1	0.292	Hardcastle et al. (1998)
3C 184.1	0.1182	Hardcastle et al. (1998)
3C 192	0.0598	Hardcastle et al. (1998)
3C 197.1	0.1301	Hardcastle et al. (1998)
3C 200	0.458	Garrington et al. (1991)
3C 217	0.897	Pedetty et al. (1989)
3C 223	0.1368	Hardcastle et al. (1998)
3C 223.1	0.1075	Hardcastle et al. (1998)
3C 234	0.184	Leahy & Williams (1984)
3C 239	1.781	Liu & Pooley (1991b)
3C 244	...	Leahy & Williams (1984)
3C 247	0.748	Liu & Pooley (1991b)
3C 252	1.100	Goodlet et al. (2004)
3C 263.1	0.824	Liu & Pooley (1991b)
3C 265	0.811	Goodlet et al. (2004)
3C 266	1.275	Liu & Pooley (1991b)
3C 267	1.140	Goodlet et al. (2004)
3C 268.1	0.970	Goodlet et al. (2004)
3C 274.1	0.422	Leahy & Williams (1984)
3C 277.2	0.766	Pedetty et al. (1989)
3C 280	0.996	Goodlet et al. (2004)
3C 284	0.239	Leahy & Williams (1984)
3C 285	0.079	Leahy & Williams (1984)
3C 288	0.246	Liu & Pooley (1991b)
3C 289	0.967	Liu & Pooley (1991b)
3C 294	1.779	Liu & Pooley (1991b)
3C 299	0.367	Goodlet et al. (2004)
3C 300	0.270	Leahy & Williams (1984)
3C 322	1.681	Leahy et al. (1989)
3C 324	1.206	Goodlet et al. (2004)
3C 327	0.1039	Hardcastle et al. (1998)
3C 330	0.550	Leahy et al. (1989)
3C 337	0.635	Pedetty et al. (1989)
3C 341	0.448	Goodlet et al. (2004)
3C 349	0.205	Hardcastle et al. (1998)
3C 352	0.806	Garrington et al. (1991)
3C 353	0.0304	Hardcastle et al. (1998)
3C 356	1.079	Pedetty et al. (1989)
3C 368	1.131	Pedetty et al. (1989)
3C 401	0.201	Hardcastle et al. (1998)
3C 403	0.059	Hardcastle et al. (1998)

TABLE 7—Continued

Source (1)	z (2)	Reference (3)
3C 405	0.056	Leahy & Williams (1984)
3C 424	0.127	Hardcastle et al. (1998)
3C 436	0.2145	Hardcastle et al. (1998)
3C 438	0.290	Hardcastle et al. (1998)
3C 452	0.0811	Hardcastle et al. (1998)
3C 457	0.428	Goodlet et al. (2004)
4C 14.11	0.206	Hardcastle et al. (1998)
4C 14.27	0.392	Goodlet et al. (2004)
4C 53.16	0.064	Garrington et al. (1991)
4C 74.16	0.81	Garrington et al. (1991)
6C 0943+39	1.040	Goodlet et al. (2004)
6C 1011+36	1.040	Goodlet et al. (2004)
6C 1129+37	1.060	Goodlet et al. (2004)
6C 1256+36	1.127	Goodlet et al. (2004)
6C 1257+36	1.000	Goodlet et al. (2004)

NOTE.—Col. (1): source name; col. (2): redshift; col. (3): reference.

5.2. Hot Spot Sizes

A strong correlation has previously been noticed between linear sizes of FR II radio galaxies and their hot spot sizes (e.g., Hardcastle et al. 1998). We find that our 13 FR II radio galaxies follow the same trend. In Figure 1 we have plotted the hot spot size (of the brightest hot spot at each end) against the core–hot spot distance. Here we have considered only the 8 GHz measurements for the hot spot sizes from Hardcastle et al. (1998) and excluded the broad-line radio galaxies from the analysis. The size of an individual hot spot was defined as the geometric mean of the largest and smallest angular sizes (see Table 4).

Using the least absolute deviation method (implemented in the LADFIT routine in IDL), we fitted a linear model in the log-log space to the combined data set and obtained a slope of 0.72 ± 0.06 . Note that by fitting a linear model to the combined data set using chi-square minimization (implemented in the LINFIT routine in IDL), we obtain a slope of 0.52 ± 0.08 (Perucho & Martí (2003) have found the slope of the radio galaxy correlation to be 0.40 ± 0.11). However, since the use of the chi-square error statistic can result in a poor fit due to an undesired sensitivity to outlying data, we consider the slope of the correlation to be close to 0.7. Thus, the following relation holds for the hot spot-size r_h and core–hot spot distance l of the radio galaxy: $r_h \propto l^{0.7}$.

This correlation provides support for suggestions that the hot spot sizes scale with source linear size (see Hardcastle et al. 1998; Laing 1989; Bridle et al. 1994). This is consistent with the hot spot maintaining ram pressure balance as the source propagates through a medium with declining ambient density (Carvalho & O’Dea 2002b). Carvalho & O’Dea (2002a, 2002b) discuss the results of two-dimensional axisymmetric numerical simulations of light, supersonic jets propagating into different density atmospheres and compare them with the predictions of three types of self-similar models. Of the self-similar models discussed, type I corresponds to the jet moving with a constant speed in a constant density atmosphere (e.g., Begelman & Cioffi 1989; Daly 1990); the type II model corresponds to jet motion in a medium where the ambient density falls off as d^{-2} (e.g., Daly 1990), where d is the distance from the source, while the type III model assumes a power-law density distribution with an exponent δ (e.g., Kaiser & Alexander 1997).

Following the relations between hot spot size, expansion time and the core–hot spot distance for type III models in Carvalho &

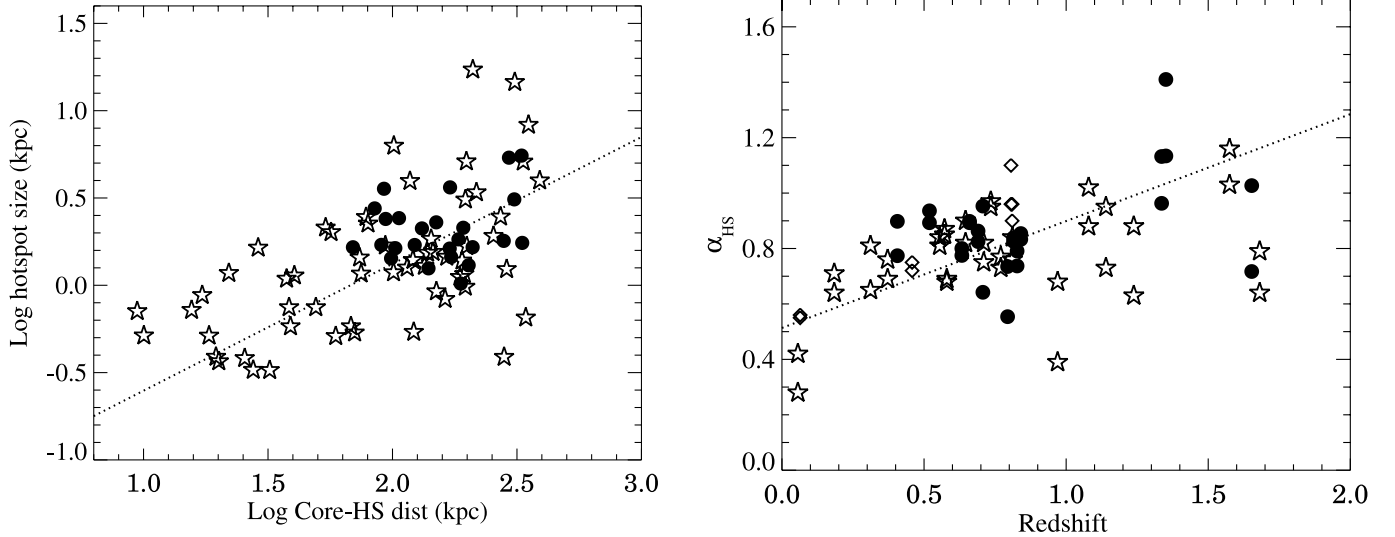


FIG. 1.—*Left*: Log-log plot of the hot spot size vs. the core–hot spot distance of the sources. Filled circles denote our sample FR II sources; open stars denote radio galaxies from Hardcastle et al. (1998). The slope of the correlation is ~ 0.7 . *Right*: The hot spot spectral index vs. redshift. The filled circles denote the hot spots for our 13 FR II sources, open stars are hot spot values from Leahy et al. (1989), while diamonds are from Garrington et al. (1991). The slope of the correlation is ~ 0.4 .

O’Dea (2002a), i.e., $r_h^2 \propto t^{(\delta+4)/(5-\delta)}$ and $l \propto t^{3/(5-\delta)}$, the derived exponent of 0.7 for the r_h - l relation translates to a δ of 0.2. This implies that the jet propagates in a nearly constant ambient density medium ($\rho_a \propto d^{-0.2}$). This inference is consistent with the sources being located in the cores of protoclusters or clusters of galaxies, which have a roughly constant ambient gas density. Indeed, a couple of our 13 FR II radio galaxies seem to reside in such environments (see notes on individual sources in the Appendix). This is supported by the previous studies of Cygnus A (Carilli et al. 1991), 3C 295 (Perley & Taylor 1991), and the study of Wellman et al. (1997). Finally, with a δ of 0.2, the hot spot advance speed is proportional to $t^{-0.4}$, thereby implying a decelerating source.

5.3. Spectral Index versus Redshift for Hot Spots and Lobes

The hot spot spectral index (α_{HS}) is found to strongly correlate with redshift (z)—the spectra become steeper at higher redshifts

(Fig. 1). This is consistent with the findings of Wellman et al. (1997), Dennett-Thorpe et al. (1999), Blundell et al. (1999), and Ishwara-Chandra & Saikia (2000). We find that the following approximate relation holds— $\alpha_{\text{HS}} \propto z^{0.4}$, with the absolute deviation in the exponent being ~ 0.03 . Note that the α_{HS} for our sources and from Garrington et al. (1991) have been estimated between 1.4 and 5 GHz, while the spectral index from Leahy et al. (1989) were derived between 151 MHz and 1.4 GHz. Excluding the data from Leahy et al. (1989) yields a slope of 0.43 ± 0.04 . The chi-square minimization method (LINFIT in IDL) results in a slope of 0.22 ± 0.05 for all the data, and 0.26 ± 0.07 when the data from Leahy et al. (1989) is excluded.

A correlation between spectral index and redshift is already well established for the integrated extended emission in FR II galaxies (e.g., Laing & Peacock 1980; Chambers et al. 1990; Athreya & Kapahi 1999; De Breuck et al. 2000). In Figure 2, we have plotted the z - α correlation for our combined radio galaxy

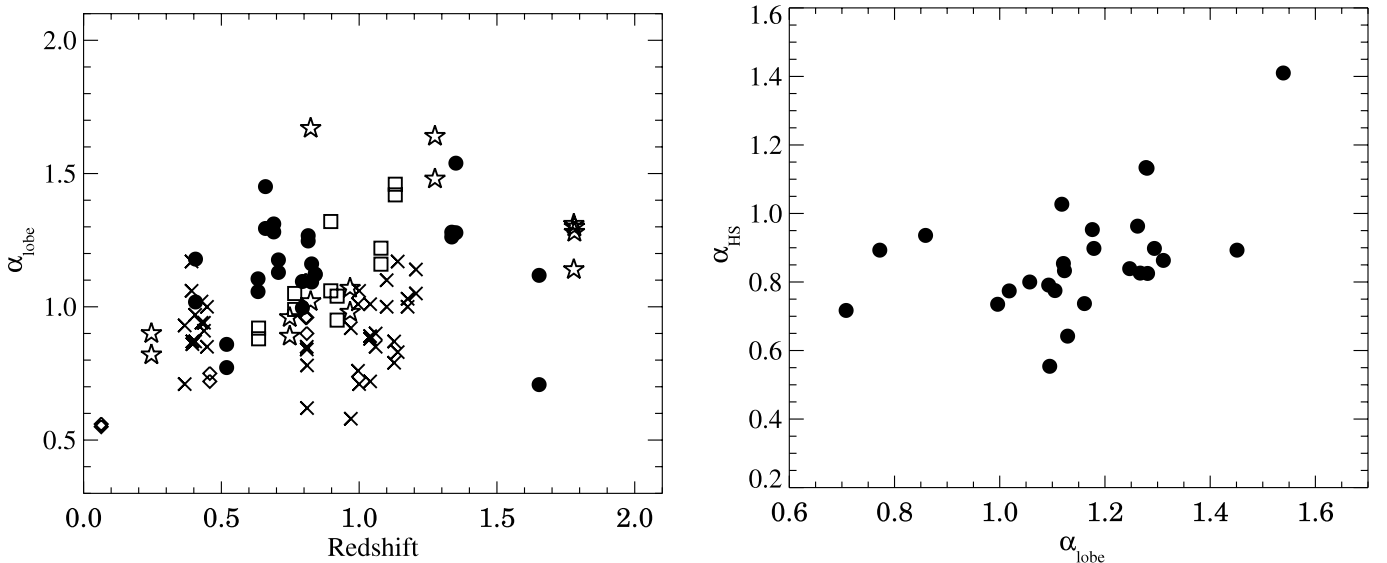


FIG. 2.—*Left*: Lobe spectral index vs. redshift. The filled circles denote our 13 radio galaxies, stars are galaxies from Liu & Pooley (1991b), squares from Pedelty et al. (1989), crosses from Goodlet et al. (2004), and diamonds from Garrington et al. (1991). *Right*: Hot spot spectral index vs. lobe spectral index for our 13 FR II radio galaxies.

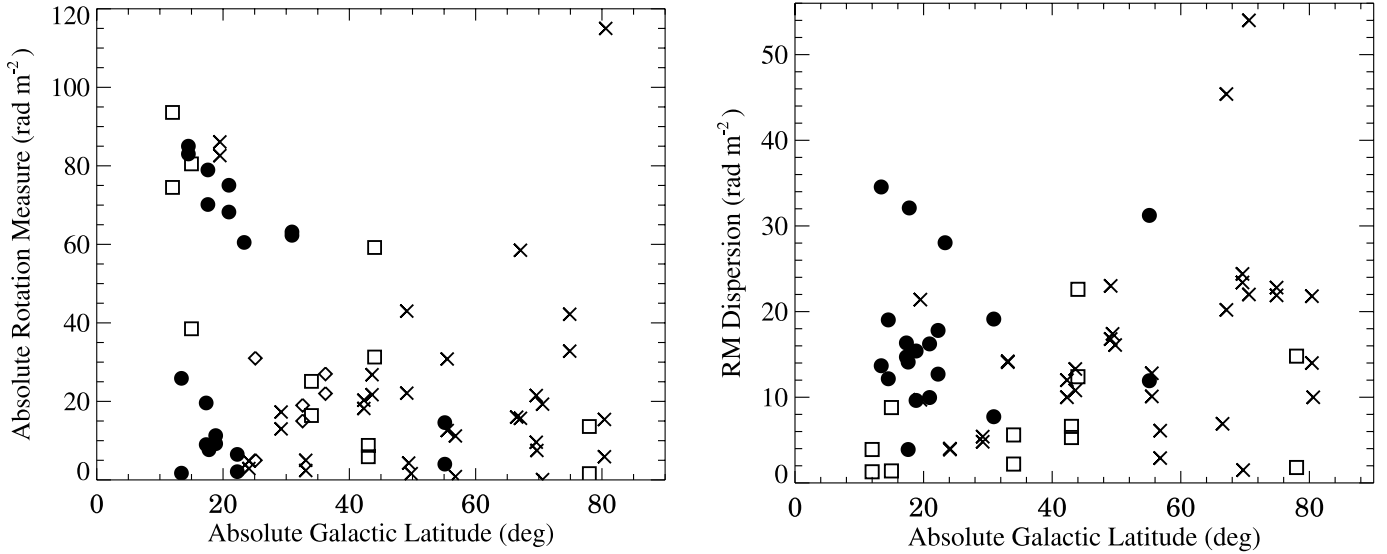


FIG. 3.—*Left*: Absolute mean rotation measure for each of the two radio lobes vs. the absolute Galactic latitude. *Right*: The rotation measure dispersion in the two lobes vs. the absolute Galactic latitude. Filled circles denote our sample FR II radio galaxies, stars and crosses denote radio galaxies from Liu & Pooley (1991b) and Goodlet et al. (2004), respectively, while squares and diamonds are galaxies from Pedelty et al. (1989) and Garrington et al. (1991), respectively.

data set. We do not find a correlation between the spectral index *difference* between the lobes and redshift, consistent with Goodlet & Kaiser (2005).

It has been pointed out that although a simple redshifting of the curved spectrum contributes to the z - α relation (e.g., Gopal-Krishna 1988; Lacy et al. 1993), it cannot account for the whole effect (e.g., Lacy et al. 1993; Blundell et al. 1999). It has been proposed that the hot spot spectral index is affected by inverse-Compton cooling owing to scattering with microwave background photons, which is a strong function of redshift (e.g., Rees & Setti 1968; Krolik & Chen 1991; Wellman et al. 1997). It has also been suggested that enhanced synchrotron losses in more powerful hot spots could also produce a spectral steepening at higher luminosity (e.g., Blundell et al. 1999; Dennett-Thorpe et al. 1999). Blundell et al. (1999) had examined three complete samples with successively fainter flux limits, in order to break the luminosity-redshift degeneracy. They reached the conclusion that the rest-frame spectral indices have a stronger dependence on luminosity than on redshift, except at GHz frequencies. Based on the finding that the extremely steep-spectrum radio galaxies in the local universe inevitably reside at the centers of rich galaxy clusters (e.g., Baldwin & Scott 1973), Klamer et al. (2006) have postulated that z - α correlation could be a result of a higher fraction of radio galaxies being located, as a function of redshift, in environments with densities similar to nearby rich clusters.

The hot spot spectral index correlates with the lobe spectral index (Fig. 2, *right*). Furthermore, the lobe spectral index is systematically steeper than the hot spot spectral index. These two results provide support to the spectral aging model in the radio lobes. Electrons are injected into the lobe with the spectral index of the hot spots. They subsequently age, making the spectra steeper.

5.4. The Rotation Measures and Dispersion

The mean rotation measure (RM) across the lobes of 11 of our 13 FR IIs varies from ~ 10 to 80 rad m^{-2} . On comparison with integrated RM measurements of Simard-Normandin et al. (1981) we find that our observed RM values are comparable to that expected from our Galaxy. The error in the rotation measure is

typically less than 5 rad m^{-2} . The rotation measure dispersion (σ_{RM}) is typically less than 20 rad m^{-2} for our sources. For two of the sources with σ_{RM} greater than 30 rad m^{-2} , viz., 3C 13 and 3C 470, large systematic errors were probably present in their bright hot spots.

Pedelty et al. (1989) had found a weak correlation between the rotation measures across the radio lobes and source Galactic latitudes, with the higher values of rotation measure occurring at lower Galactic latitudes. We find that such a correlation is significant at the 99% level (Spearman-Rank and Kendall's-tau correlation tests) for the combined radio galaxy data set (Fig. 3). The rotation measure dispersion and Galactic latitude are not correlated (see Table 8). These results suggest that the large-scale rotation measure is likely dominated by the Galactic foreground, whereas the small-scale structure in rotation measure (σ_{RM}) is produced in the source and/or its environment for these relatively high-latitude sources (e.g., Kronberg et al. 1972; Simonetti et al. 1984; Leahy 1987).

Figure 4 shows the rotation measure dispersion plotted against the depolarization measure. We find no correlation between these two parameters (see Table 8). The lack of a correlation is consistent with the possibility that both the RM dispersion and depolarization result from a partially resolved foreground screen, associated with the radio source but in front of it (Tribble 1991; Johnson et al. 1995; Goodlet & Kaiser 2005). However, this cannot be demonstrated unequivocally for these sources.

5.5. The Depolarization Asymmetry in Radio Lobes

Several strong correlations have been observed with lobe depolarization asymmetries in FR II radio galaxies. In sources with strong one-sided jets, the jet side tends to depolarize less rapidly with increasing wavelength, also referred to as the ‘‘Laing-Garrington’’ effect (Laing 1988; Garrington et al. 1988). Furthermore, the more depolarized lobe has a steeper spectrum (the ‘‘Liu-Pooley’’ effect) and smaller angular distance between the core and the hot spot (Laing 1988; Liu & Pooley 1991a, 1991b). Also, an asymmetry exists in the distribution of the emission-line gas in radio galaxies, with more emission-line gas lying on that side of the radio source for which the depolarization is stronger (McCarthy & van Breugel 1989).

TABLE 8
CORRELATION STATISTICS

Property 1	Property 2	Spearman Statistic	Spearman Prob.	Kendall Statistic	Kendall Prob.
Significant Correlations					
r_h	l	0.537	1.6E-7	0.373	5.3E-7
α_{lobe}	z	0.355	0.0002	0.243	0.0003
α_{HS}	z	0.393	0.0007	0.299	0.0002
$DP_N - DP_S$	$\alpha_N - \alpha_S$	-0.466	0.001	-0.317	0.002
$\alpha_N - \alpha_S$	N-S length ratio	-0.445	0.001	-0.296	0.003
AR	Q	-0.352	0.003	-0.250	0.002
$DP_N - DP_S$	N-S length ratio	0.448	0.002	0.315	0.002
α_{HS}	α_{lobe}	0.508	0.007	0.361	0.009
Marginal Correlations					
Q	ζ	0.306	0.010	0.206	0.012
$ RM $	$ b ^\dagger$	-0.287	0.014	-0.205	0.011
$DP_N - DP_S$	$AR_N - AR_S$	0.669	0.024	0.550	0.018
DP	z	-0.237	0.024	-0.160	0.024
ζ	R_c	0.367	0.038	0.234	0.059
$ \alpha_N - \alpha_S $	R_c	-0.452	0.009	-0.308	0.013
No Correlations					
σ_{RM}	$ b ^\ddagger$	0.205	0.100	0.141	0.095
$\alpha_N - \alpha_S$	z	-0.162	0.275	-0.116	0.249
AR	ζ	-0.128	0.294	-0.084	0.308
DP	AR	0.167	0.414	0.132	0.341
$ DP_N - DP_S $	ζ	0.095	0.539	0.043	0.677
Q	R_c	-0.092	0.615	-0.060	0.624
ζ	z	-0.092	0.454	-0.065	0.431
$ DP_N - DP_S $	R_c	-0.122	0.550	-0.080	0.565
$ \alpha_N - \alpha_S $	ζ	-0.049	0.745	-0.034	0.734
$DP_N - DP_S$	z	-0.032	0.762	-0.028	0.695
DP	σ_{RM}	-0.014	0.919	-0.009	0.921
Q	z	0.002	0.981	0.012	0.882

NOTES.—The correlations arranged according to decreasing probability. Cols. (1) and (2): The parameters examined for a correlation: ($|RM|$) absolute value of rotation measure; ($|b|$) absolute Galactic latitude; (DP) depolarization; (Q) arm-length ratio; (ζ) misalignment angle; (AR) axial ratio; (R_c) radio core prominence; (r_h) hot spot size; (l) core-hot spot distance; (α_{HS}) hot spot spectral index between 1.4 and 5 GHz; (α_{lobe}) lobe spectral index between 1.4 and 5 GHz; (z) redshift. Cols. (3) and (5): Spearman's (rho) and Kendall's (tau) rank correlation coefficient. Cols. (4) and (6): Probability that the two properties in cols. (1) and (2) are not correlated, using Spearman's (rho) and Kendall's (tau) rank correlation tests, respectively. A small value indicates a significant correlation. Dagger (\dagger) signifies that the correlation is significant at the 99.99% significance level, when the single high RM value from Goodlet et al. (2004) is excluded. Double dagger (\ddagger) signifies that there is no correlation (Spearman prob. = 0.196) when the two high σ_{RM} values from Goodlet et al. (2004) are excluded.

Most of the 13 FR II radio galaxies have an arm-length ratio close to unity (Table 5). The misalignment angles are typically less than 8° . Furthermore, the radio core prominence in these 13 FR IIs is small, $-4.3 \leq \log R_c \leq -2.5$ (see Table 6). The small misalignment angles and radio core prominence suggest that our 13 FR II galaxies are largely plane-of-sky objects. This is consistent with the absence of bright radio jets in these radio galaxies. This makes them useful for a spectral aging study (Paper II).

5.5.1. The Laing-Garrington Effect

The jet-sidedness–depolarization relation cannot be unambiguously examined for our 6 FR II radio galaxies with mostly tentative jet detections. As the Laing-Garrington effect is suggested to be a consequence of Doppler beaming, we examined the difference in lobe depolarization with respect to the (statistical) orientation indicators—the radio core prominence and the misalignment angle, for the larger combined data set (Fig. 5). We find

that the lobe-to-lobe differences in depolarization are not correlated with either the radio core prominence or the misalignment angle. The lack of a correlation is consistent with the picture of these radio galaxies lying close to the plane of the sky. However, it must be noted that Garrington et al. (1991) failed to see a correlation between depolarization asymmetry ratio and core strength, even in quasars. This is probably due to the large scatter in core prominence relation and the fact that this test is intrinsically less sensitive than one that compares quantities pertaining to two lobes. The lack of any correlation between the sidedness of faint jets with depolarization in a radio galaxy sample with weak jets has been noted by Laing (1993).

5.5.2. The Liu-Pooley Effect

Liu & Pooley (1991a) found evidence for a correlation between the depolarization measure and lobe spectral index. They found that the radio lobe with the flatter spectrum is associated

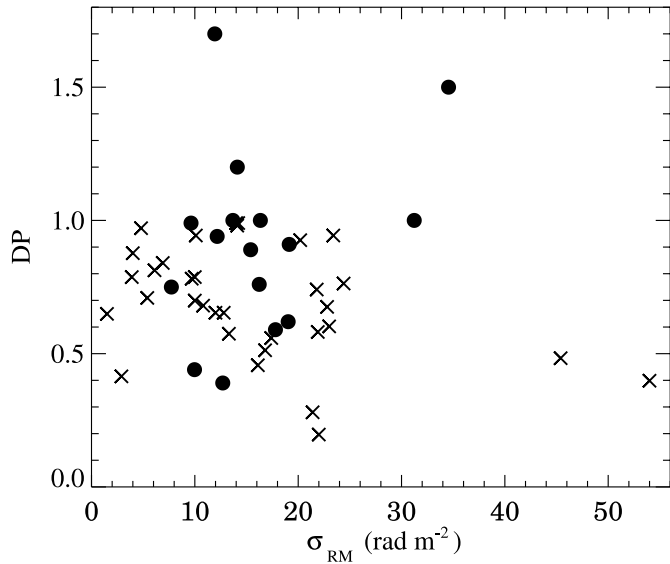


FIG. 4.—Two depolarization parameters DP and σ_{RM} plotted against each other. Filled circles denote our sample FR II radio galaxies, while crosses denote radio galaxies from Goodlet et al. (2004).

with lower depolarization. Among the 13 sample FR IIs, 11 sources have lobe depolarization measure and spectral index estimates, while only 7 have depolarization estimates for both the lobes (see Table 5). Six out of these 7 sources show lower depolarization in the lobe with the flatter spectral index. We examined the Liu-Pooley correlation with the combined data set and found that the correlation is significant at the 99.99% significance level (Fig. 6). This is a significant improvement from the original radio galaxy (excluding quasars) correlation, which was observed at the $\sim 80\%$ significance level (also see Ishwara-Chandra et al. 2001).

Liu & Pooley (1991a) have pointed out that the line-of-sight effects that derive from the orientation of the jet do not give a clear explanation for the $DP-\alpha$ correlation (see also Dennett-Thorpe et al. 1997). They concluded that differences in the medium surrounding the two radio lobes influence both the spectrum

and the depolarization. A denser medium around one radio lobe would result in greater confinement of the lobe, thereby decreasing the expansion losses and possibly increasing the radiative losses, resulting in a steeper spectral index and greater depolarization. McCarthy et al. (1991) have indeed demonstrated that the emission-line gas is intrinsically asymmetric in powerful radio sources, and the differences in the density of the surrounding medium is sufficient to explain the observed arm-length ratios in radio galaxies (however, see Best et al. 1995). We do find the presence of the “alignment effect” (McCarthy 1993), in 4 of our 13 FR II radio galaxies (see the Appendix).

With the intention of singling out factors that could contribute to the $DP-\alpha$ correlation, we examined the dependence of lobe depolarization and spectral index with (possible) orientation and environmental indicators. We find that the lobe depolarization difference is correlated with the north-to-south arm-length ratio (see Fig. 6), (as found by Pedetty et al. 1989; Laing 1996), in the sense that the shorter side of the source is more depolarized. This is in keeping with the idea of greater confinement around the shorter lobe by the source environment, which leads to greater depolarization (Liu & Pooley 1991b). We also find a tentative correlation between the difference in the lobe depolarization and the difference in axial ratios at a significance level greater than 99.8% (see Fig. 7). No trend is observed between the depolarization and axial ratio taken for each lobe separately. More data are clearly required to reexamine these relations. The trend between lobe depolarization difference and the axial ratio difference implies that shorter and/or fatter lobes are more depolarized. Again this is consistent with the picture of greater confinement around the lobes by the source environment, which gives rise to fatter lobes and depolarization.

We find that the absolute lobe-to-lobe difference in spectral index does not correlate with the misalignment angle but shows a marginal correlation with the radio core prominence—core-dominant sources seem to have smaller differences in their lobe spectral indices (see Fig. 8 and Table 8). However, if relativistic beaming was indeed present in these radio galaxies, one would expect a correlation in the opposite sense. We confirm the significant correlation of the lobe spectral index difference with the north-to-south arm-length ratio, i.e., the shorter lobe has the steeper spectral index (Fig. 7).

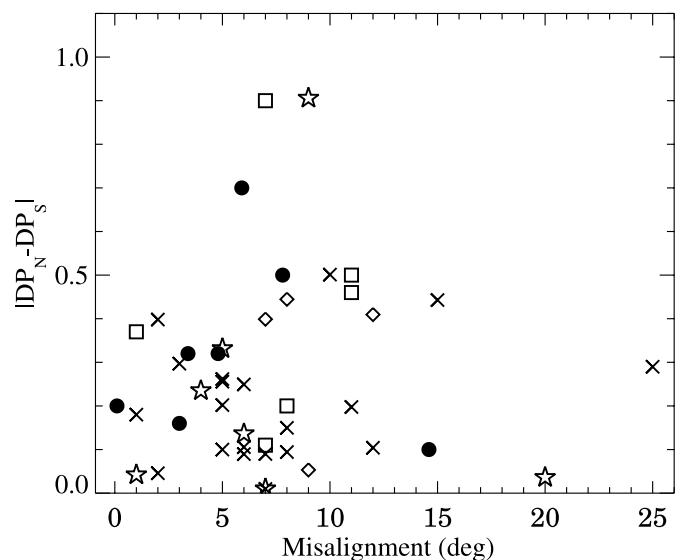
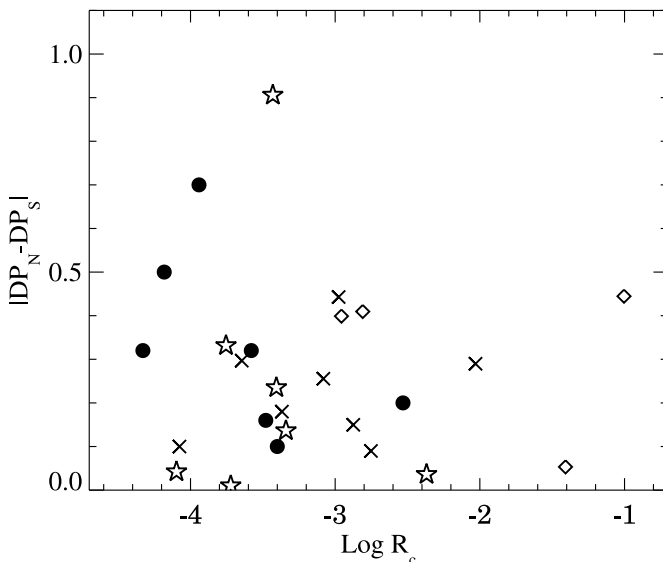


FIG. 5.—Absolute north-to-south lobe difference in depolarization vs. the radio core prominence (*left*) and misalignment angle (*right*). Filled circles denote our sample FR II radio galaxies, stars and crosses denote radio galaxies from Liu & Pooley (1991b) and Goodlet et al. (2004), respectively, while squares and diamonds are galaxies from Pedetty et al. (1989) and Garrington et al. (1991), respectively.

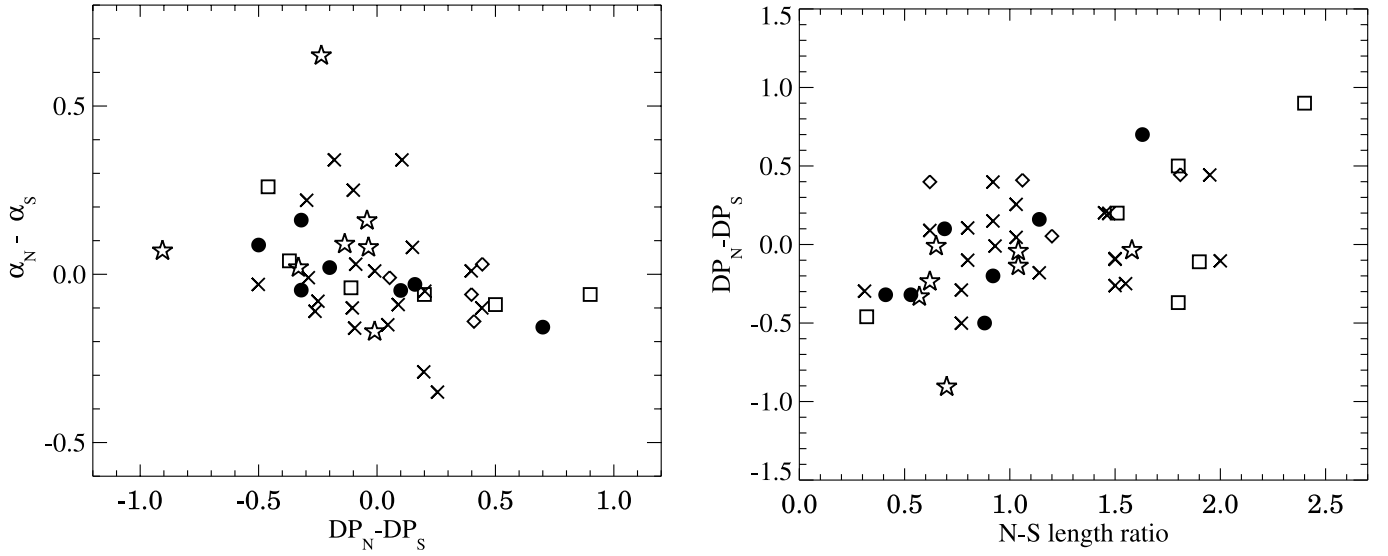


FIG. 6.—*Left*: North-to-south lobe difference in the spectral index vs. the depolarization parameter. *Right*: North-to-south lobe difference in depolarization vs. the north-to-south arm-length ratio. Filled circles denote our sample FR II radio galaxies, stars and crosses denote radio galaxies from Liu & Pooley (1991b) and Goodlet et al. (2004), respectively, while squares and diamonds are galaxies from Pedelty et al. (1989) and Garrington et al. (1991), respectively.

5.6. Structural Asymmetries and Trends with Redshifts

Although the 13 FR IIs have largely symmetric structures, trends with structural asymmetries emerge when the larger combined data set is considered (see Gopal-Krishna & Wiita 2004 for a review on structural asymmetries). We find a correlation between the arm-length ratio and misalignment angle at the 99.9% significance level for the combined radio galaxy sample (Fig. 10)—sources whose lobes are asymmetric in length show greater misalignment between the two sides. This effect has been previously observed by, for example, Macklin (1981) and Kapahi & Saikia (1982). This correlation could suggest that the environmental asymmetries that give rise to the arm-length ratio could also be contributing to the misalignment angles in these radio galaxies, as also suggested by Macklin (1981).

The amount of misalignment also places a limit on the systematic jet axis stability and/or the dentist drill effect. If a source

has two or more hot spots on one side of the source, and these two hot spots plus the core (or these two hot spots and the hot spot on the other side of the source) aligned to within some angle, say 1° , then the outflow axis must not change by more than an amount θ in a time δt . The quantity θ is the accuracy with which the hot spots and the core line up and δt is equal to or larger than the separation of the two hot spots on one side of the source divided by the speed of light. Thus, if the separation of the two hot spots on one side is 10 kpc, and all of the hot spots line up to better than a degree, the wobble of the outflow axis must be less than about 10^{-14} rad s^{-1} . Wobbling could also produce substructure within the hot spots with a characteristic size that is proportional to the core-hot spot separation, and this could impact the overall hot spot size. As the misalignment angles are typically less than 10° in our 13 FR II radio galaxies, we infer that the wobble of the outflow axis in these sources is less than 10^{-13} rad s^{-1} . This argument is based on the relative positions of

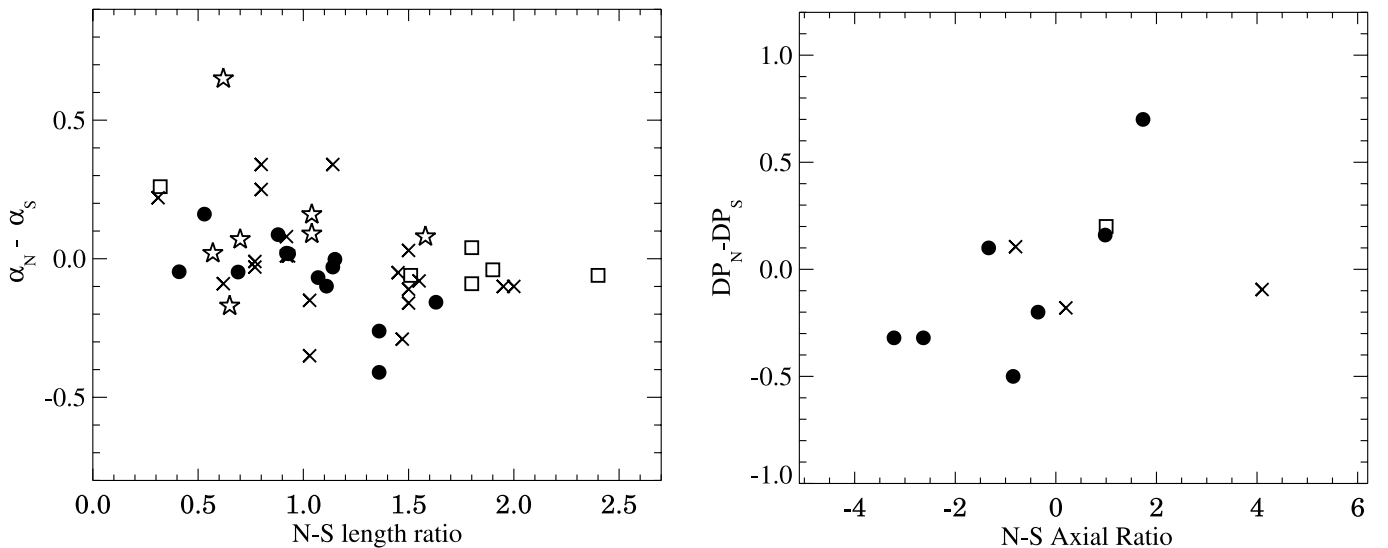


FIG. 7.—*Left*: North-to-south lobe difference in the spectral index vs. the north-to-south arm-length ratio. *Right*: North-to-south lobe depolarization difference vs. the axial ratio difference between the radio lobes. More data are clearly required to reexamine this correlation. Filled circles denote our sample FR II radio galaxies, stars and crosses denote radio galaxies from Liu & Pooley (1991b) and Goodlet et al. (2004), respectively, while squares and diamonds are galaxies from Pedelty et al. (1989) and Garrington et al. (1991), respectively.

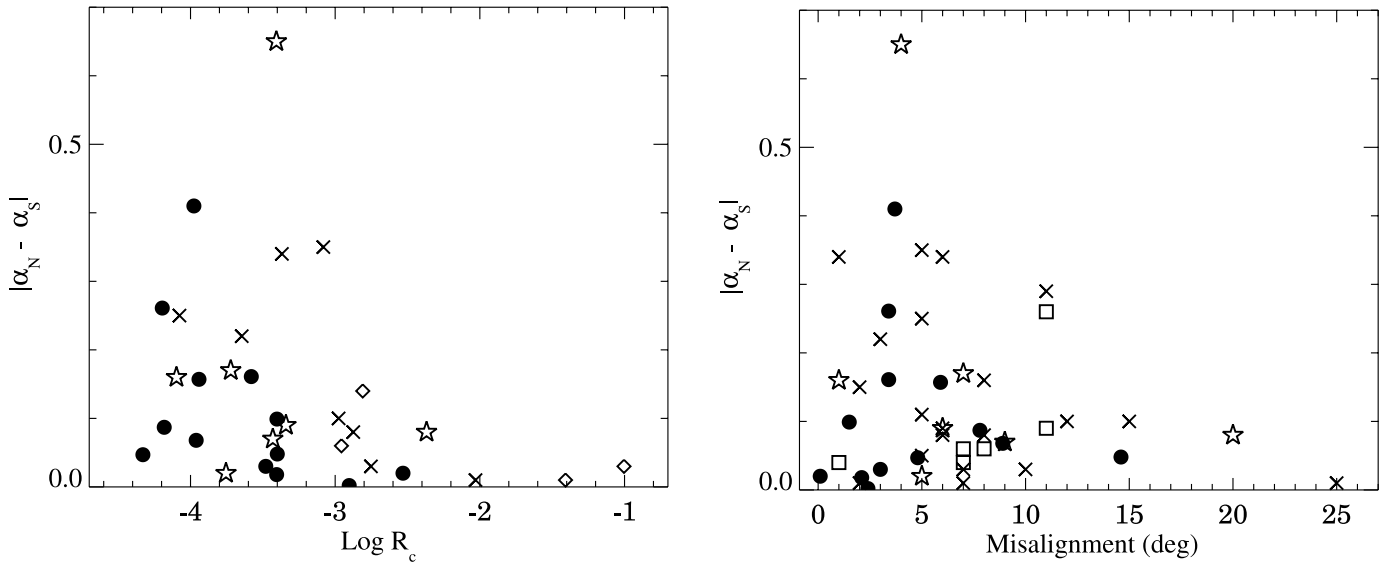


FIG. 8.—Absolute north-to-south lobe difference in the spectral index vs. the radio core prominence (*left*) and misalignment angle (*right*). Filled circles denote our sample FR II radio galaxies, stars and crosses denote radio galaxies from Liu & Pooley (1991b) and Goodlet et al. (2004), respectively, while squares and diamonds are galaxies from Pedelty et al. (1989) and Garrington et al. (1991), respectively.

the hot spots and the core and does not account for possible light travel time effects. These effects will be small if the source is close to the plane of the sky.

The radio core prominence is plotted with respect to the arm-length ratio and misalignment angle in Figure 9. We observe a weak correlation between core prominence R_c and misalignment angle ζ but none between R_c and arm-length ratio Q (see Table 8). The radio core prominence-misalignment angle (R_c - ζ) correlation has previously been observed by, for example, Kapahi & Saikia (1982) and Hough & Readhead (1989). This correlation could be suggestive of the presence of relativistic beaming effects in the core due to orientation in the combined radio galaxy sample. On the other hand, there could be an environmental contribution to both the radio core prominence and misalignment angle. For example, the interaction of the jet as it is launched, with the surrounding nuclear environment could give rise to a brighter radio

core along with changes in its direction of propagation, resulting in greater misalignment angles.

We find an anticorrelation between the arm-length ratios and axial ratios for the radio galaxies. In Figure 10, we have plotted the axial ratios for each lobe separately, with respect to the arm-length ratio, for the combined radio galaxy data set. The (anti-)correlation implies that sources that have a fatter lobe on one side are also the most asymmetric in length. This effect is also clearly visible in the radio maps. If one radio lobe is shorter than the other, it could perhaps be due to a difference in the surrounding medium that slows down the expansion and confines one radio lobe preferentially. The overpressured radio plasma expands laterally when the jet meets resistance in the forward direction, thus producing fatter lobes. A larger variation in outflow direction can also lead to larger misalignment, fatter lobes, and smaller axial ratios. The axial ratios and misalignment angles are, however, not correlated

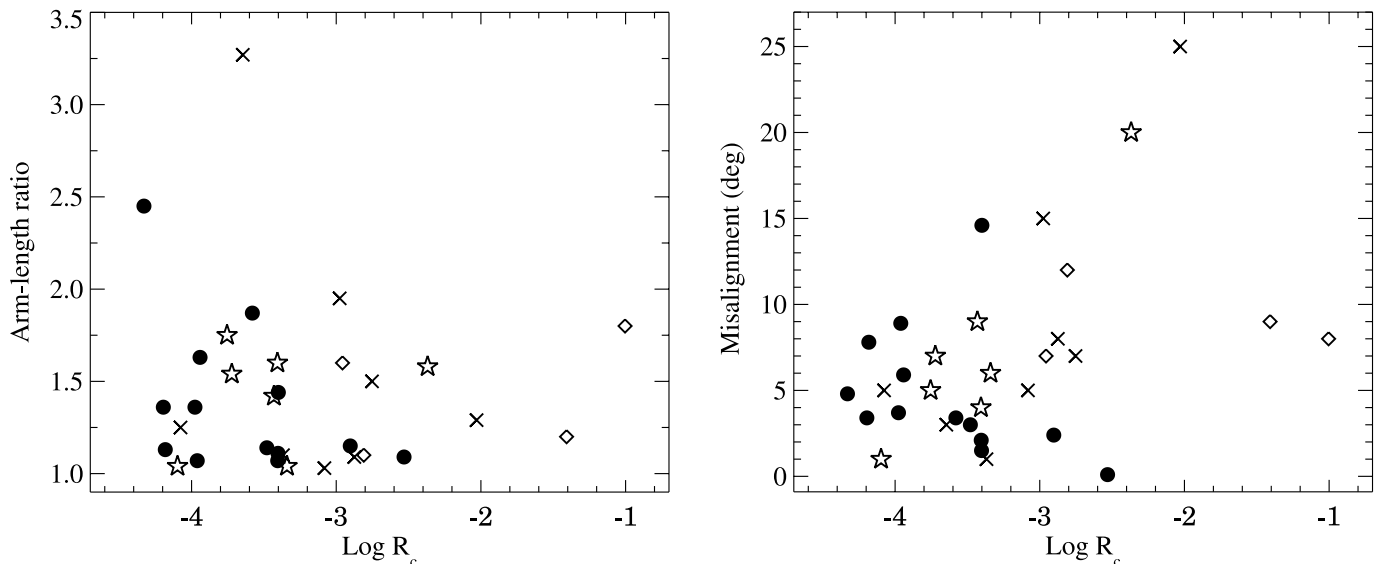


FIG. 9.—*Left*: Arm-length ratio vs. the radio core prominence parameter. *Right*: Misalignment angle vs. the radio core prominence. Filled circles denote our sample FR II radio galaxies, stars and crosses denote radio galaxies from Liu & Pooley (1991b) and Goodlet et al. (2004), respectively, and diamonds are galaxies from Garrington et al. (1991).

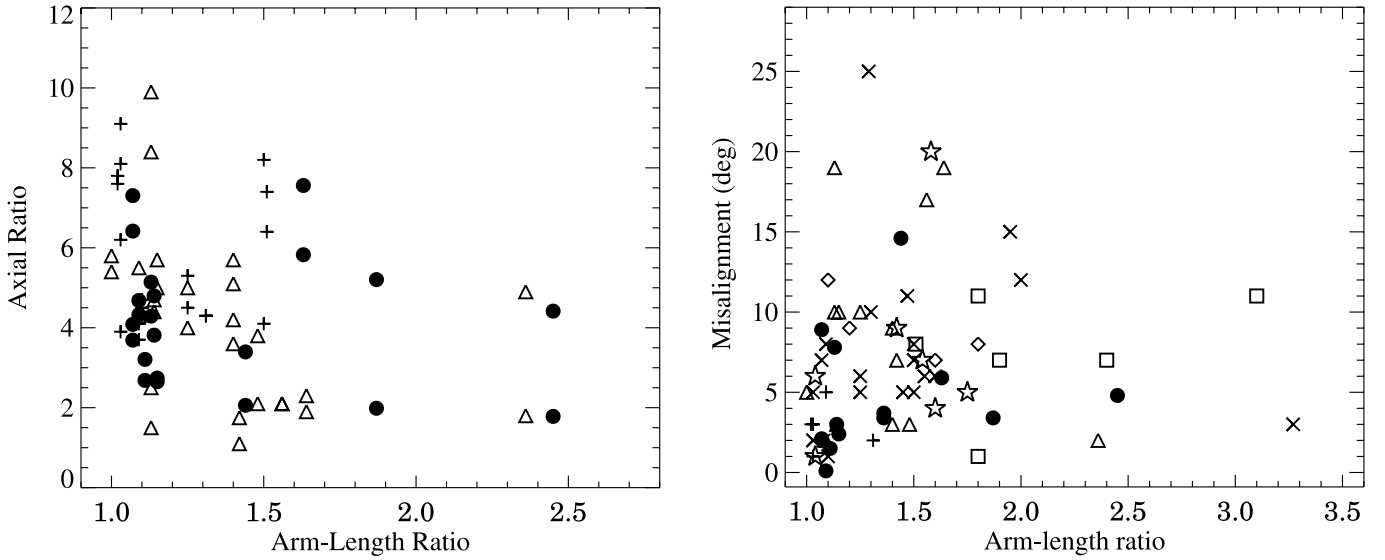


FIG. 10.—*Left*: Axial ratio for each radio lobe vs. the arm-length ratio. *Right*: Misalignment angle vs. arm-length ratio. The filled circles denote the radio galaxies from our sample, stars represent data from Liu & Pooley (1991b), squares from Pedelty et al. (1989), crosses from Goodlet et al. (2004), diamonds from Garrington et al. (1991), triangles from Leahy & Williams (1984), and plus signs from Leahy et al. (1989).

(see Table 8). The lack of a correlation does not diminish the importance of the variation in outflow direction, because symmetric motions like the precession of the entire black hole–double-jet system, could result in zero misalignment but still increase the axial ratios.

The anticorrelation between axial ratio and arm-length ratio and the correlation between depolarization and axial ratio (Fig. 7) leads to an interesting new result. While it has been known for a long time that the shorter lobe is more depolarized in these radio galaxies, we find that shorter lobe is also the fatter one. This explains the correlation between depolarization and axial ratio. In a nutshell, we find that the shorter lobe is fatter, is more depolarized, and has a steeper spectrum.

We do not find any correlation between misalignment angle and redshift, nor between arm-length ratio and redshift (Fig. 11). Barthel & Miley (1988) had found a tentative correlation between misalignment angle and redshift, but Kapahi & Kulkarni

(1990) and Best et al. (1995) did not find such a correlation, consistent with our result.

We find a correlation between the lobe depolarization DP and redshift (Fig. 12). Kronberg et al. (1972) and Goodlet & Kaiser (2005) have also found that the lobes of high-redshift galaxies are more depolarized than their local counterparts. This would indicate that source environments vary with redshift, which would be consistent with the increasing alignment of emission line gas with the radio source with increasing redshift (e.g., McCarthy 1993; Best et al. 2000; Inskip et al. 2002; Privon et al. 2008). However, Morris & Tabara (1973) discovered that lobe depolarization showed a stronger dependence on the radio luminosity rather than on redshift. Goodlet & Kaiser (2005) have also found that lobe depolarization depends on both radio luminosity and redshift. We do not find a correlation between the depolarization difference between the lobes and redshift (see Table 8). Goodlet & Kaiser (2005) have reported the presence of this correlation,

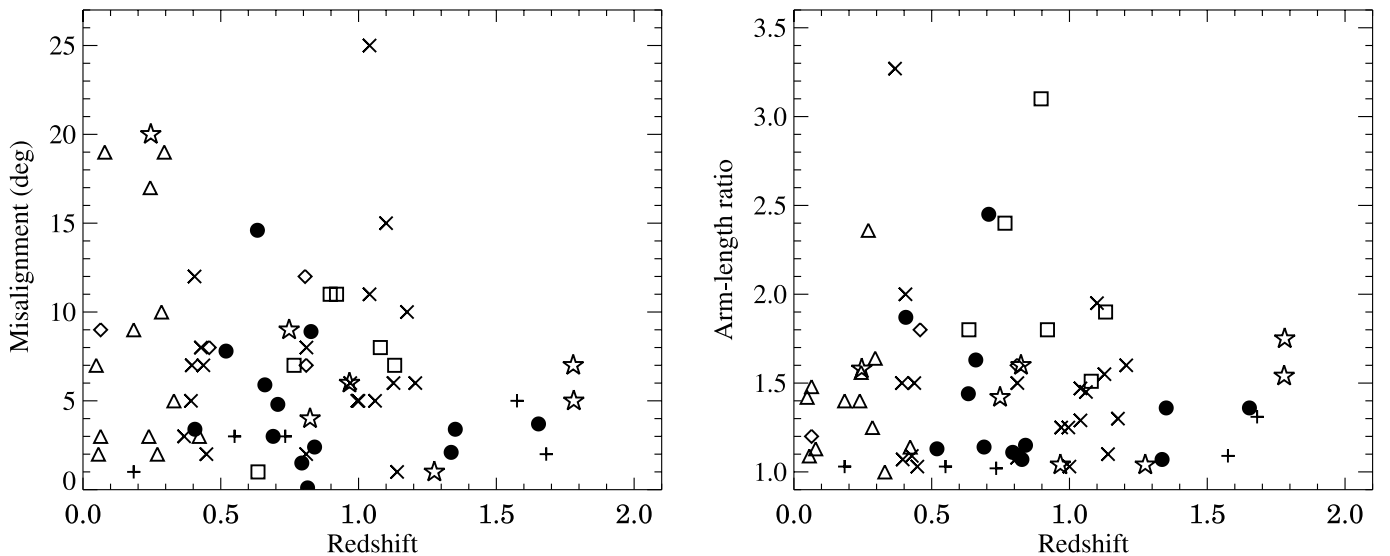


FIG. 11.—Misalignment angle (*left*) and arm-length ratio (*right*) vs. redshift. The filled circles denote our 13 radio galaxies, stars represent galaxies from Liu & Pooley (1991b), squares from Pedelty et al. (1989), crosses from Goodlet et al. (2004), diamonds from Garrington et al. (1991), triangles from Leahy & Williams (1984), and plus signs from Leahy et al. (1989). No correlation is observed between the parameters.

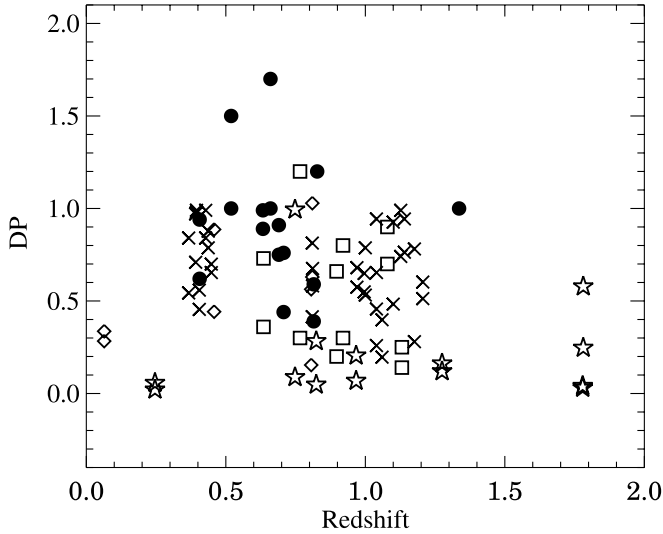


FIG. 12.—Depolarization for each radio lobe vs. redshift. The filled circles denote our 13 radio galaxies, stars represent galaxies from Liu & Pooley (1991b), squares from Pedely et al. (1989), crosses from Goodlet et al. (2004), and diamonds from Garrington et al. (1991).

contrary to our finding. We note, however, that our sample size is twice as large as Goodlet’s sample and spans a larger redshift range.

6. SUMMARY AND CONCLUSIONS

We have observed 13 large and powerful FR II radio galaxies with multiple arrays of the Very Large Array at the frequencies 330 MHz, 1.4, 5, and 8 GHz. Extended radio bridges are detected in all but two FR II galaxies (3C 13 and 3C 470). The rotation measures between 1.4 and 5 GHz are small, comparable to the expected Galactic contribution. The spectral index maps between 1.4 and 5 GHz show a gradual steepening of the radio spectra away from the hot spots with some spectral index variations superimposed, in agreement with previous studies.

The 13 FR II radio galaxies do not show the presence of bright jets and the core-to-lobe flux density ratio, i.e., the radio core prominence is typically small ($-4 \leq \log R_c \leq -2$), indicating that these sources lie close to the plane of the sky. This is also consistent with the small misalignment angles, which are less than 8° in all but one source. These characteristics make our sample useful for a spectral aging analysis, which will be presented in Paper II.

We have supplemented our small sample with similar radio galaxy data gleaned from the literature and examined some well-known radio galaxy correlations.

1. We confirm that the hot spot size r_h is correlated with the core-hot spot distance l of the source and follows the relation $r_h \propto l^{0.7}$. This is consistent with the hot spot maintaining ram pressure balance as the source propagates through a medium with declining ambient density. This result is further consistent with a self-similar model of a jet propagating in a medium where the ambient density ρ_a falls off with distance from source d as $\rho_a \propto d^{-0.2}$. This could be due to the jets spanning hundreds of kiloparsecs in these sources, propagating through a roughly constant medium such as that which might be found in the core of a cluster or protocluster of galaxies.

2. The hot spot spectral index varies with redshift as $\alpha_{\text{HS}} \propto z^{0.4}$, consistent with previous studies on radio galaxies. A simple redshifting of the curved spectrum along with an increase in

inverse-Compton cooling due to scattering with microwave background photons at larger redshifts, could be responsible for this correlation. Alternatively, enhanced synchrotron losses in more powerful hot spots could be producing a spectral steepening at higher luminosity. This correlation could also be a result of a higher fraction of radio galaxies being located, as a function of redshift, in environments with densities similar to nearby rich clusters.

3. The hot spot spectral index is correlated with and flatter than the lobe spectral index, consistent with the assumptions of spectral aging models.

4. We find that the trend between the lobe depolarization and orientation, i.e., the “Laing-Garrington effect” is weak in these radio galaxies, suggesting that orientation/Doppler effects are not strong in them—these galaxies lie largely in the plane of the sky.

5. The correlation between lobe depolarization and lobe spectral index, i.e., the “Liu-Pooley effect,” gains in statistical significance—radio lobes with a flatter spectrum exhibit lower depolarization.

6. The lobe depolarization difference is correlated with the north-to-south arm-length ratio, in the sense that the shorter side of the source is more depolarized. This strongly suggests that lobe depolarization depends significantly on environmental asymmetries in radio galaxies. The weak correlation between the lobe depolarization and the axial ratio difference is consistent with this inference.

7. In agreement with previous studies, we find that the lobe spectral index and depolarization are correlated with redshift. While the lobe spectral index–redshift correlation follows from points 2 and 3 above, the lobe depolarization–redshift correlation could suggest a variation in the source environments. However, this effect cannot be differentiated from the dependence of depolarization on radio luminosity.

8. Based on the small misalignment angles in our 13 FR II radio galaxies, we infer that the wobble of the outflow axis in these sources is less than $10^{-13} \text{ rad s}^{-1}$.

9. We observe a weak correlation between the radio core prominence and misalignment angle but none between core prominence and arm-length ratio. This is consistent with both core prominence and misalignment angle being orientation indicators, and the arm-length ratio being more sensitive toward asymmetries in the environment. The radio core prominence and misalignment can, however, also be correlated if the inner jet interacts with the ambient medium, resulting in brighter radio cores and larger misalignment angles.

10. The arm-length ratio seems to be significantly correlated with the misalignment angle between the two sides of the radio source but anticorrelated with the axial ratio. This is again suggestive of environmental asymmetries close to the radio sources. Such asymmetries can cause a variation in the outflow direction, which can result in larger misalignments. Variation in the jet direction can also result in fatter radio lobes and lower axial ratios.

11. We find that the shorter lobe is fatter, is more depolarized, and has a steeper spectrum.

To summarize, the FR II radio galaxy attributes can be influenced by many factors such as their local environment and asymmetries in the gas in the interstellar and intergalactic medium, and relativistic beaming effects. Changes in the outflow direction and variations in the beam power with time, may also be playing a role. Radio core prominence and misalignment angles can be used as statistical indicators of orientation, while the arm-length and axial ratios can serve to highlight environmental asymmetries in large radio galaxy samples. However, the environmental contribution to the

orientation indicators, and the presence of variable motion of the outflow axis, cannot be ignored.

We would like to express our thanks to the referee for a careful assessment of our work, which has significantly improved this paper. We thank Joel C. Carvalho for stimulating discussions on this work. This work was supported in part by the US National Science

Foundation under grant AST-0507465 (R. A. D.). The National Radio Astronomy Observatory is a facility of the National Science Foundation operated under cooperative agreement by Associated Universities, Inc. This research has made use of the NASA/IPAC Extragalactic Database (NED), which is operated by the Jet Propulsion Laboratory, California Institute of Technology, under contract with the National Aeronautics and Space Administration.

Facilities: VLA (A, B, C, and D array configurations)

APPENDIX

NOTES ON INDIVIDUAL SOURCES

The final maps at 1.4 and 5 GHz, restored with a $2.0''$ or $2.5''$ circular Gaussian beam, the 330 MHz maps restored with a $5.0''$ circular Gaussian beam, and the 8 GHz maps with insets for the hot spots are presented in Figures 13–49. Rotation measure and spectral images are shown in Figure Sets 50 and 51.

3C 6.1.—The *Hubble Space Telescope* (*HST*) observations with WFPC2/F702W by McCarthy et al. (1997) show the optical galaxy to be compact with the lower isophotes extending at P.A. $\sim 30^\circ$, roughly aligned with the radio axis (Pooley & Henbest 1974). The overall radio morphology could be classified as type LW1. The spectral index $\alpha_{5,0}^{1.4}$ shows a general steepening away from the hot spot and toward the core.

3C 13.—The *HST* observations of this source show the optical galaxy to be extended over nearly $4''$ with two tail-like structures to the south and east of the nucleus (McCarthy et al. 1997). The extended emission in both the nucleus and on the $1''$ scale is aligned with the radio axis at a P.A. of 145° . Best et al. (1997a, 1998) find that the infrared emission from the host galaxy is also strongly aligned with the radio axis. Our radio image shows clear hot spots but no radio core in this high-redshift source (Fig. 15). More sensitive observations are required to be able to image the full radio bridge.

3C 34.—This source lies in a compact cluster of galaxies (McCarthy et al. 1995). The *HST* observations of McCarthy et al. (1997) find that the central galaxy is diffuse with a low surface brightness. Best et al. (1997b) have proposed that the aligned optical emission observed in the *HST* images of 3C 34 is associated with a region of massive star formation, induced by the passage of the radio jet through a galaxy within the surrounding cluster. In Figure 18 we see that 3C 34 shows twin hot spots on the eastern side. The polarization image shows extensive structure and changes in the orientation of the magnetic field. The 5 GHz gray scale image shows a faint jet on both sides of the core with the jet on the western side being brighter closer to the core.

3C 41.—The *HST* observations of McCarthy et al. (1997) and Best et al. (1997a) show that the optical galaxy is compact and symmetrical. The *K*-band image of the galaxy indicates that it is misaligned by about 25° with the radio axis (Best et al. 1997a, 1998). We observe extended radio bridge region in this source, but the radio core is observed only in the 8 GHz image (see Fig. 21). The high-resolution image at 8 GHz also shows a complex hot spot region. The radio morphology shows a LW3-type distortion, although the southern lobe seems to turn back toward the core close to it. The spectral index map shows a flatter spectral index extending through the center of the northern lobe, perhaps suggesting the presence of the radio jet (Fig. 51.3).

3C 44.—This galaxy lies in a cluster (Spinrad 1986; McCarthy et al. 1995). The *HST* observations show that the galaxy is either composed of two components oriented north-south or, more likely, is bisected by a dust lane running east-west (McCarthy et al.

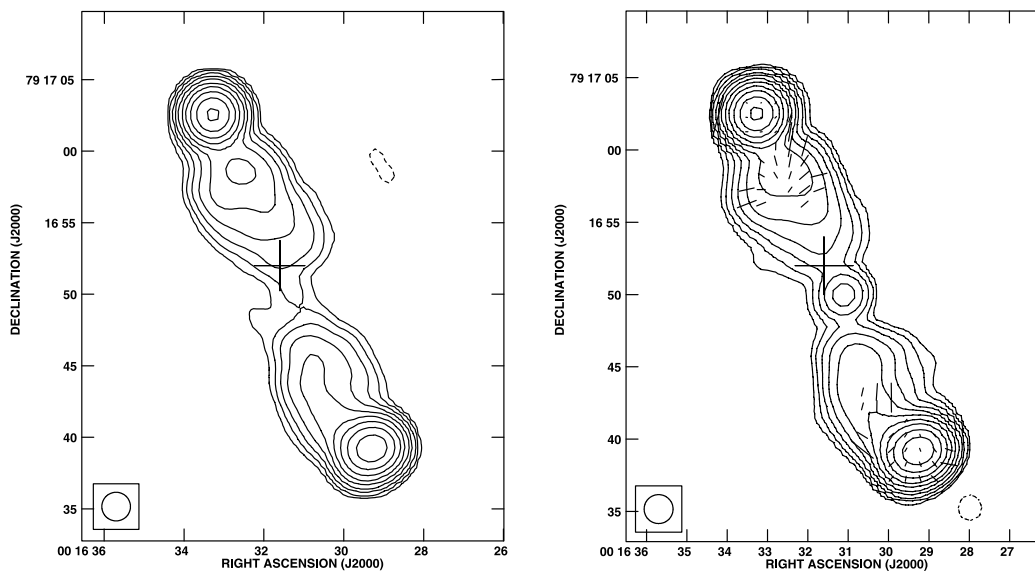


FIG. 13.—Total intensity image of 3C 6.1 at (left) 1.66 GHz and (right) 4.86 GHz, at a resolution of $2''$ with fractional polarization vectors superimposed. The peak surface brightness and contour levels increasing in steps of 2 are (left) 1.2 Jy beam^{-1} , ($-0.17, 0.17, \dots, 90\%$ of peak brightness, (right) $419.9 \text{ mJy beam}^{-1}$, ($-0.085, 0.085, \dots, 90\%$ of peak brightness, $1''$ vector = 17% polarization.

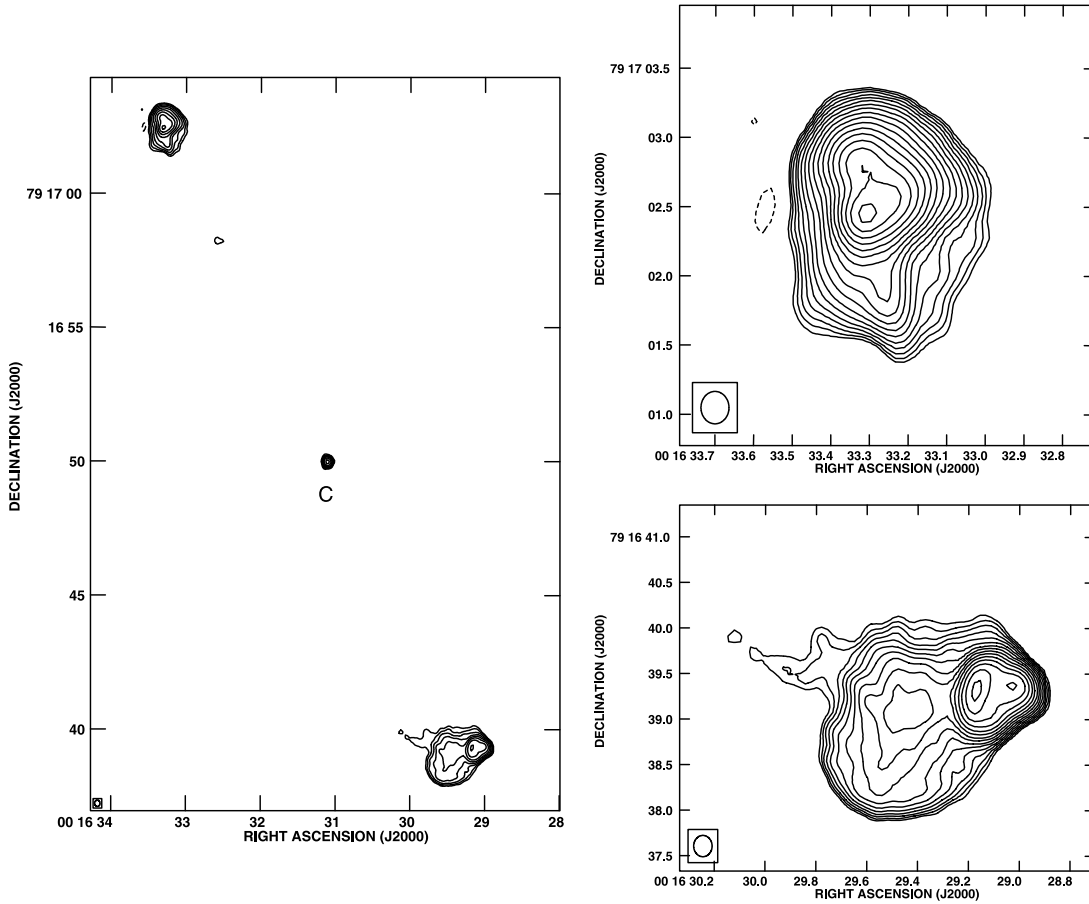


FIG. 14.—Total intensity image of 3C 6.1 at 8.4 GHz. The peak surface brightness and contour levels increasing in steps of $2(\sqrt{2})$ for the closeup views of the hot spot regions) are $49.2 \text{ mJy beam}^{-1}$ and $(-0.35, 0.35, \dots, 90)\%$ of peak brightness, respectively.

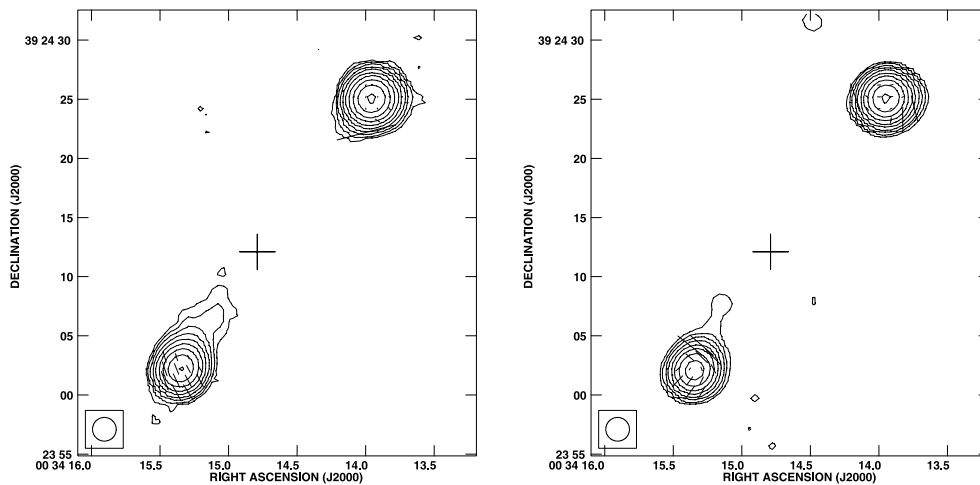


FIG. 15.—Total intensity image of 3C 13 at (left) 1.46 GHz and (right) 4.86 GHz, at a resolution of $2''$ with fractional polarization vectors superimposed. The peak surface brightness and contour levels increasing in steps of 2 are (left) $1.06 \text{ Jy beam}^{-1}$, $(-0.17, 0.17, \dots, 90)\%$ of peak brightness, $1''$ vector = 7% polarization, (right) $270.0 \text{ mJy beam}^{-1}$, $(-0.17, 0.17, \dots, 90)\%$ of peak brightness, $1''$ vector = 7% polarization.

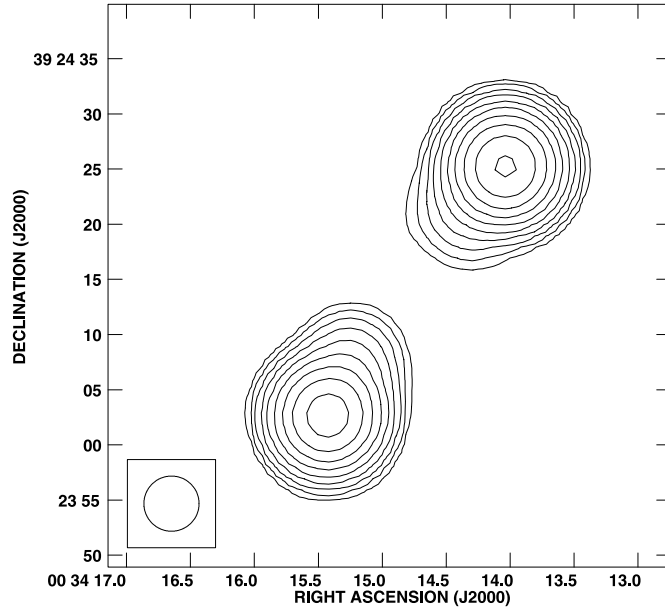


FIG. 16.— Total intensity image of 3C 13 at 327.6 MHz. The peak surface brightness and contour levels increasing in steps of 2 are 4.3 Jy beam^{-1} , $(-0.17, 0.17, \dots, 90)\%$ of peak brightness.

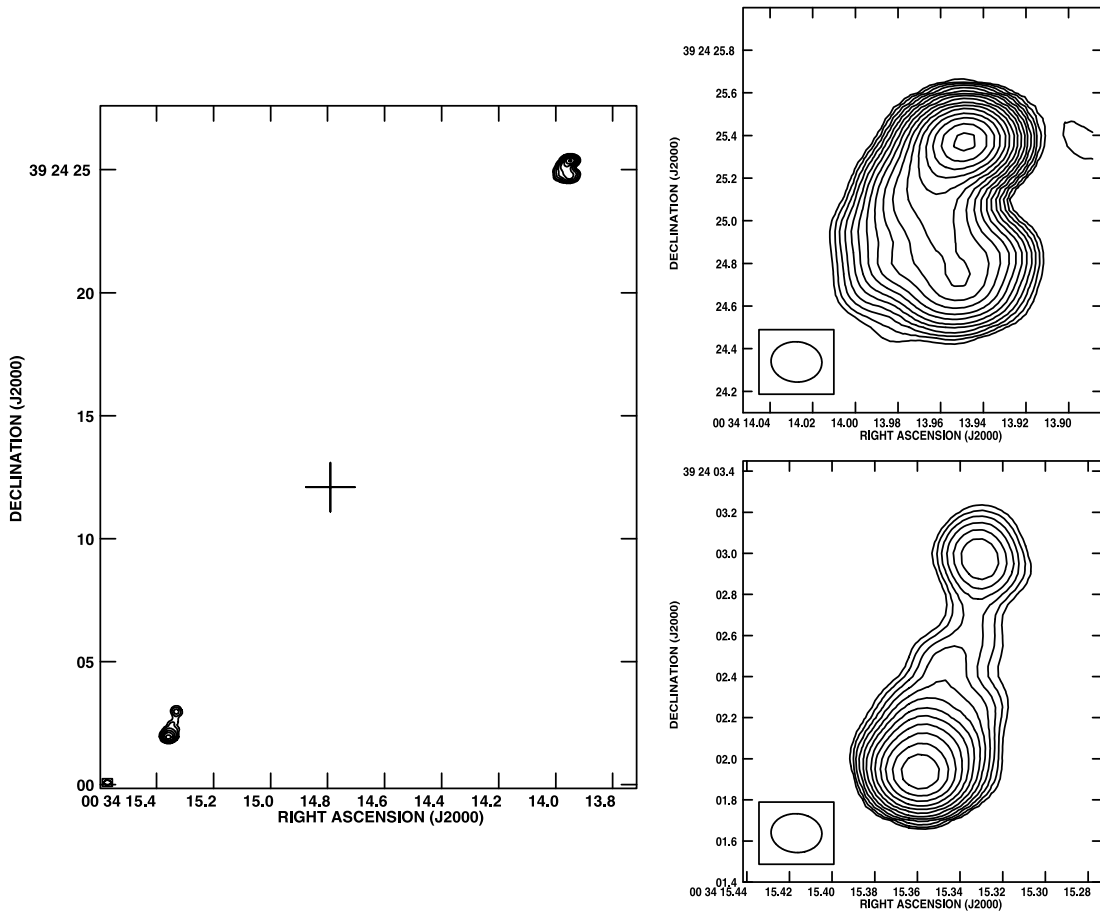


FIG. 17.— Total intensity image of 3C 13 at 8.4 GHz. The peak surface brightness and contour levels increasing in steps of $2(\sqrt{2})$ (for the closeup views of the hot spot regions) are $60.3 \text{ mJy beam}^{-1}$, $(-0.7, 0.7, \dots, 90)\%$ of peak brightness.

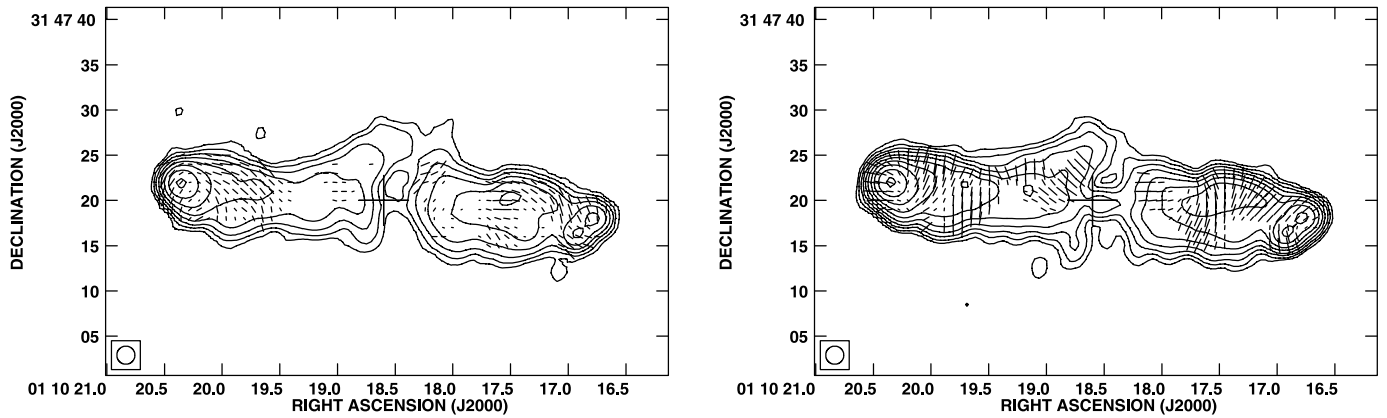


FIG. 18.—Total intensity image of 3C 34 at (*left*) 1.66 GHz and (*right*) 4.86 GHz, at a resolution of $2''$ with fractional polarization vectors superimposed. The peak surface brightness and contour levels increasing in steps of 2 are (*left*) $135.5 \text{ mJy beam}^{-1}$, $(-0.7, 0.7, \dots, 90)\%$ of peak brightness, $1''$ vector = 20% polarization, (*right*) $57.8 \text{ mJy beam}^{-1}$, $(-0.17, 0.17, \dots, 90)\%$ of peak brightness, $1''$ vector = 17% polarization.

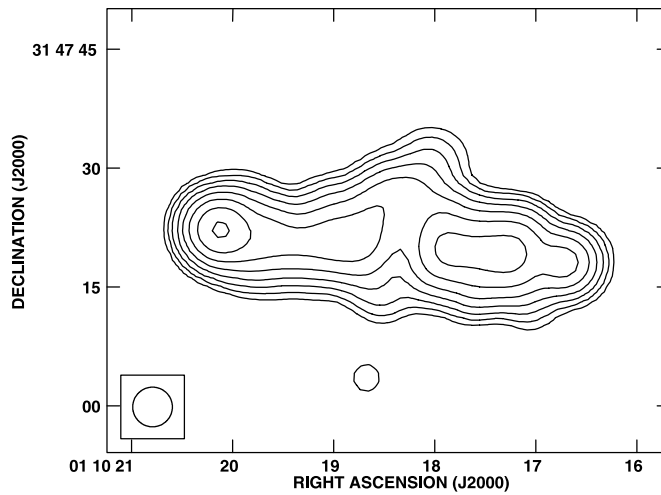


FIG. 19.—Total intensity image of 3C 34 at 327.6 MHz. The peak surface brightness and contour levels increasing in steps of 2 are $913.8 \text{ mJy beam}^{-1}$, $(-0.7, 0.7, \dots, 90)\%$ of peak brightness.

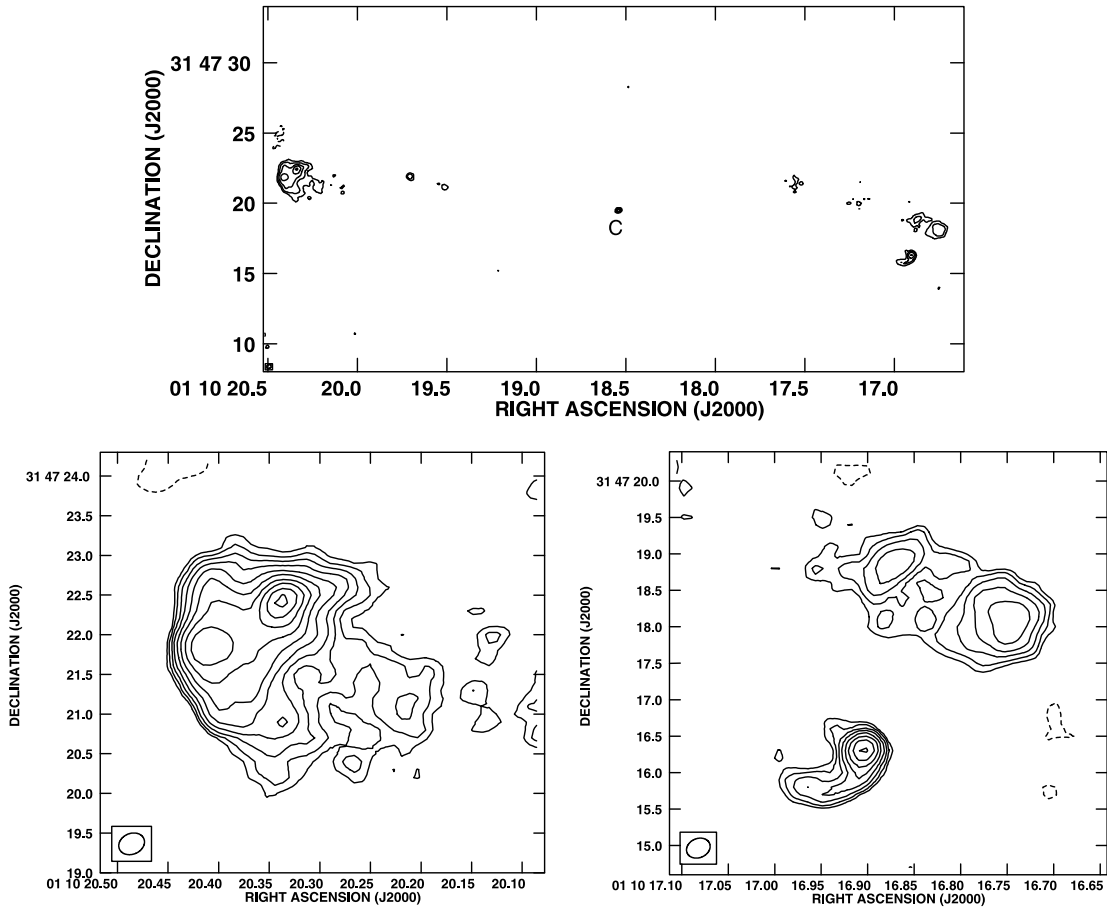


FIG. 20.—Total intensity image of 3C 34 at 8.4 GHz. The peak surface brightness and contour levels increasing in steps of $2(\sqrt{2})$ for the closeup views of the hot spot regions) are $3.4 \text{ mJy beam}^{-1}$, ($-5.6, 5.6, \dots, 90$)% of peak brightness. The lowest contour level in the hot spot blowup is 4% of the peak brightness.

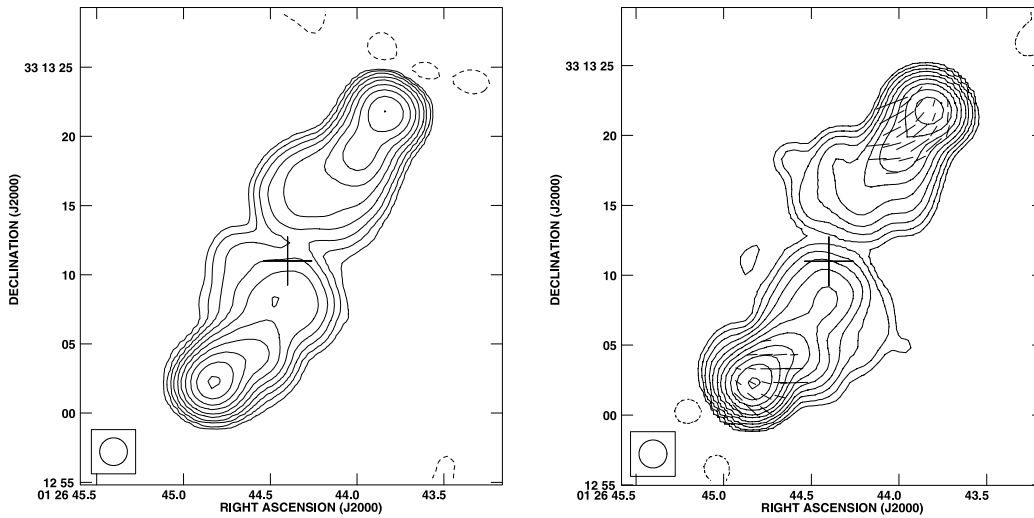


FIG. 21.—Total intensity image of 3C 41 at (left) 1.34 GHz and (right) 4.86 GHz, at a resolution of $2''$ with fractional polarization vectors superimposed. The peak surface brightness and contour levels increasing in steps of 2 are (left) $977.0 \text{ mJy beam}^{-1}$, ($-0.17, 0.17, \dots, 90$)% of peak brightness, (right) $502.6 \text{ mJy beam}^{-1}$, ($-0.085, 0.085, \dots, 90$)% of peak brightness, $1''$ vector = 10% polarization.

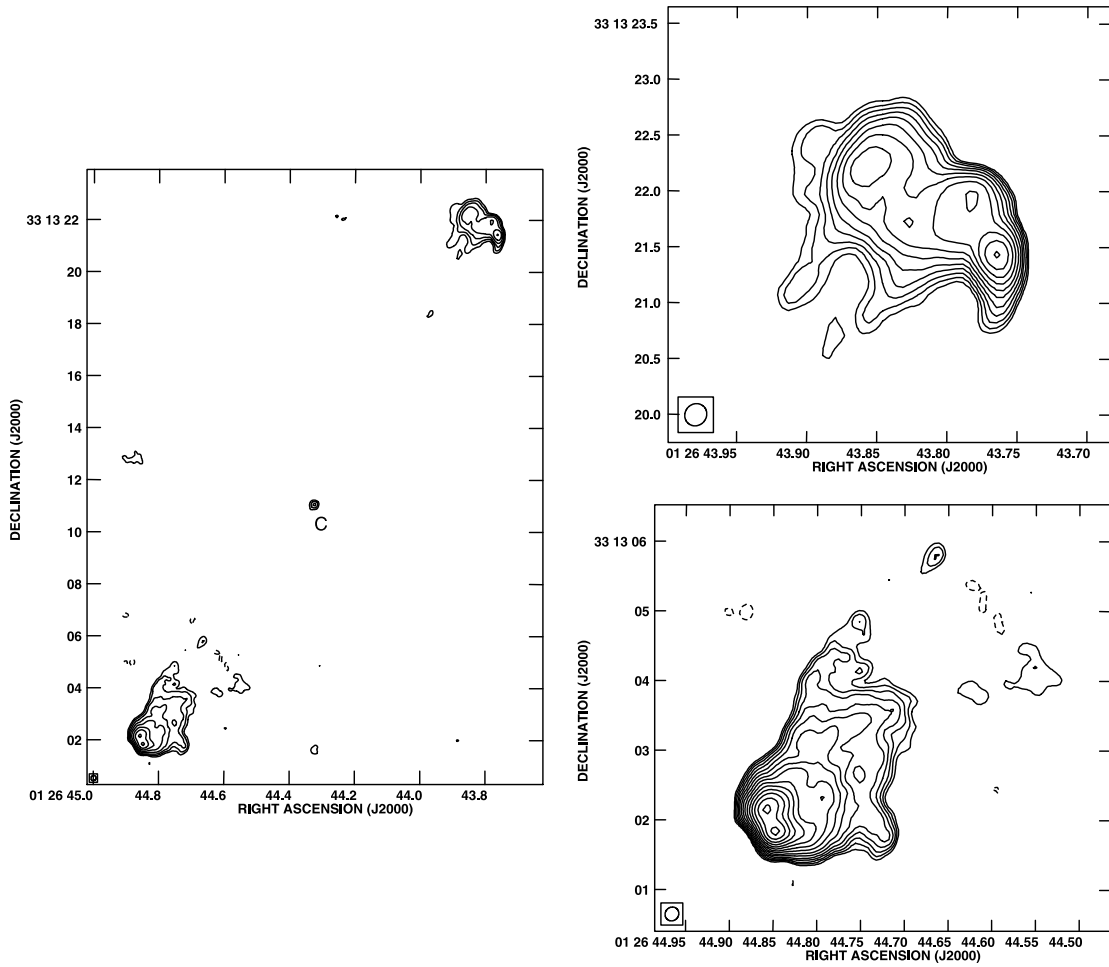


FIG. 22.— Total intensity image of 3C 41 at 8.4 GHz. The peak surface brightness and contour levels increasing in steps of $2(\sqrt{2})$ for the closeup views of the hot spot regions) are $38.2 \text{ mJy beam}^{-1}$ and $(-0.7, 0.7, \dots, 90)\%$ of peak brightness, respectively. The lowest contour level in the hot spot blowup is 0.5% of the peak brightness.

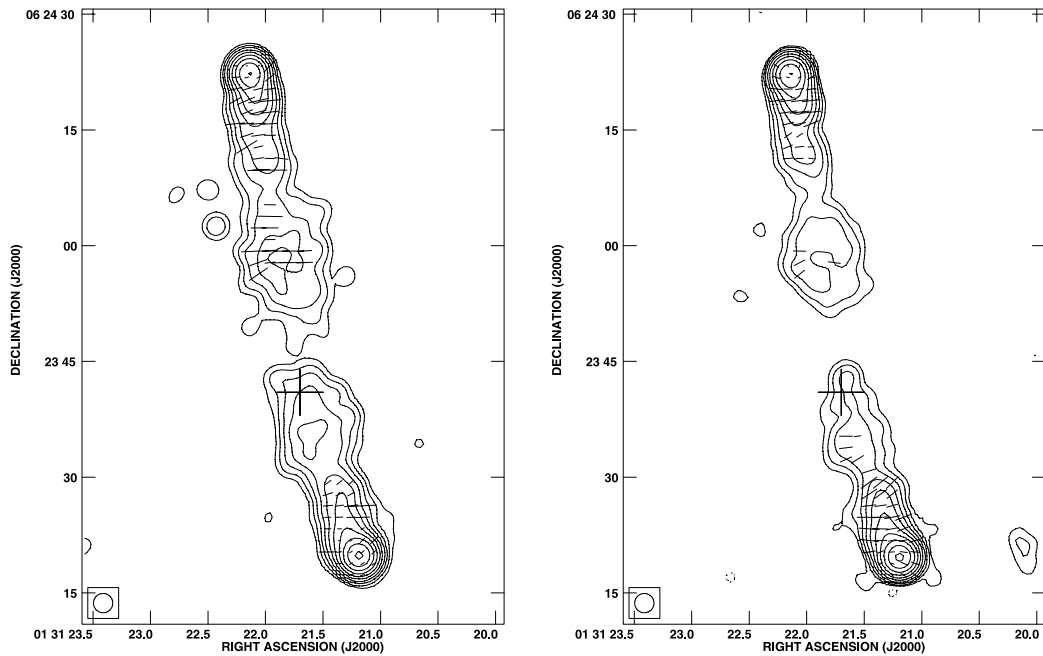


FIG. 23.— Total intensity image of 3C 44 at (left) 1.66 GHz and (right) 4.86 GHz, at a resolution of $2.5''$ with fractional polarization vectors superimposed. The peak surface brightness and contour levels increasing in steps of 2 are (left) $432.1 \text{ mJy beam}^{-1}$, $(-0.17, 0.17, \dots, 90)\%$ of peak brightness, $1''$ vector = 13% polarization, (right) $136.1 \text{ mJy beam}^{-1}$, $(-0.17, 0.17, \dots, 90)\%$ of peak brightness, $1''$ vector = 10% polarization.

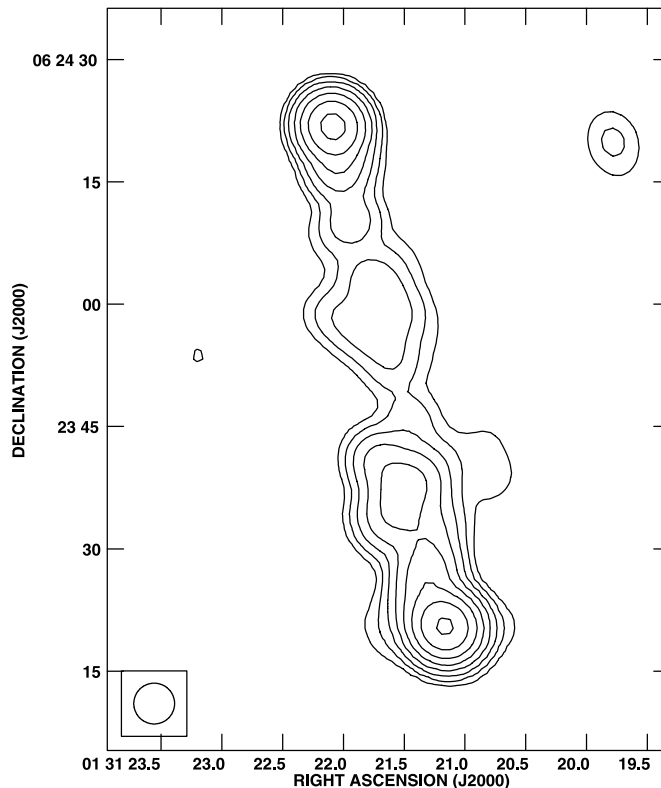


FIG. 24.—Total intensity image of 3C 44 at 327.6 MHz. The peak surface brightness and contour levels increasing in steps of 2 are 1.6 Jy beam^{-1} , $(-0.7, 0.7, \dots, 90)\%$ of peak brightness.

1997). Figure 23 shows that this source exhibits a LW1-type radio morphology. We detect a weak radio core at the position, R.A. = $01^{\text{h}}31^{\text{m}}21.6459^{\text{s}}$, decl. = $06^{\circ}23'43.1048''$. There is a bright radio source on the eastern side about $50''$ from the core in 3C 44. The spectral index shows a general steepening away from the hot spots (Fig. 51.1). 3C 44 shows a hint of a jetlike structure extending toward the southern hot spot in the 5 GHz image (Fig. 52).

3C 54.—The *HST* observations reveal a compact nucleus in this galaxy with an extension to the southwest in P.A. 220° (McCarthy et al. 1997). There is a compact object near the end of the $2''$ extension from the nucleus. It is unclear if the extension is a bridge, tidal tail, or jet. There is another companion object a few arcseconds to the southeast. In Figure 26 we see that this source shows a LW1-type lobe morphology. No radio core is observed. The northern hot spot shows two components in the 5 GHz image. 3C 54 shows a jetlike structure extending toward the southern hot spot in the 5 GHz image.

3C 114.—The low surface brightness optical galaxy of 3C 114 is poorly detected in the *HST* observations (McCarthy et al. 1997). A faint compact nucleus with several clumps within the central few arcseconds is observed in this source. The radio bridge region and core are clearly detected in our observations (Fig. 29). 3C 114 shows a jetlike structure extending toward the southern hot spot in the 5 GHz image. However, the jetlike feature is more prominent on the northern side in the 1.4 GHz image.

3C 142.1.—Extended [O II] emission in an elongated east-west structure $\sim 5''$ across has been observed for 3C 142.1 by Hes et al. (1996). The radio source lies close to a P.A. $\sim 40^{\circ}$, not aligned with the emission-line region. We see clear extended radio lobes in 3C 142.1. (Fig. 32). The southern lobe shows a nearly constant spectral index across it (Fig. 51.7). This is an interesting source with a bridge structure that is different from most sources. It does not show the classic surface brightness decline from the hot spot toward the core, has a roughly constant spectral index and a complex hot spot structure.

3C 169.1.—McCarthy et al. (1997) have observed two galaxies in this system, both with extended structure. The host galaxy of 3C 169.1 shows a clear extension to the east with a number of faint clumps within the central arcsecond. The two components lie along the radio axis, and the companion object has an extension pointing toward the radio galaxy. In Figure 35 we see that the northern hot spot is much fainter than the southern hot spot. The northern hot spot is not detected in the 8 GHz image.

3C 172.—The *HST* image of 3C 712 shows that it lies in a complex system—four objects are detected in the optical image (McCarthy et al. 1997). There are two galaxies lying to the southwest that appear to be associated with 3C 172, and they lie along the axis of the radio source. We find that this source has an interesting radio structure (see Fig. 38). The bridge appears to pull away to the west side of the source. The polarization image suggests that the magnetic field has been carried to the side of the radio bridge along with the relativistic plasma. However, the 8 GHz image indicates that the two brightest hot spots and the weak radio core lie roughly along a line. 3C 172 shows a jetlike feature closer to the northern hot spot in the 5 GHz image.

3C 441.—The *HST* observations of 3C 441 by McCarthy et al. (1997) and Best et al. (1997a) show that the host galaxy is compact and lies in a cluster. The optical galaxy shows a slight extension to the northwest, along the radio axis. The *HST* image shows a diffuse object located $12''$ north and $8''$ west of the core galaxy. We find that this source has a complex radio morphology, especially in the northern radio lobe and hot spot (Fig. 41). The maps suggest that the jet has shifted position moving from the west to the present

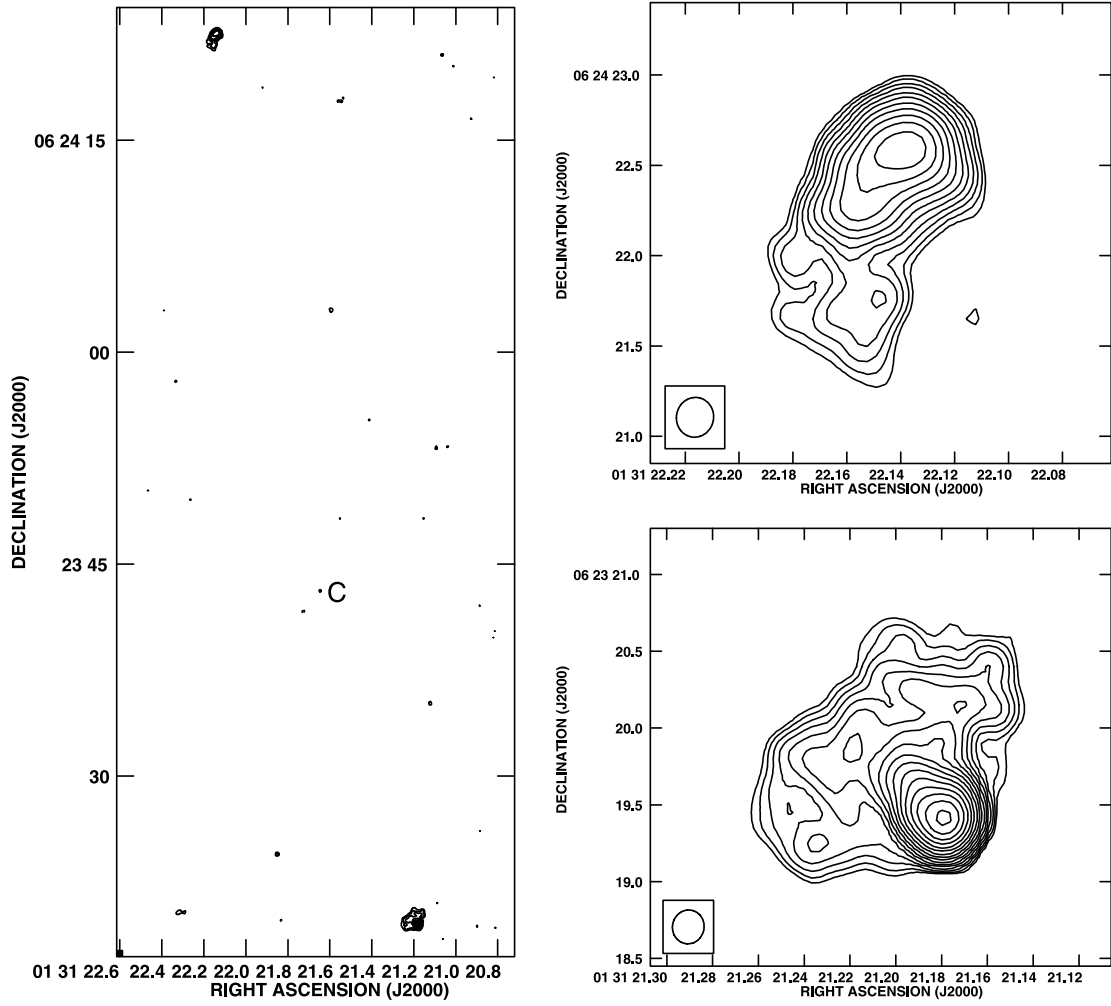


FIG. 25.— Total intensity image of 3C 44 at 8.4 GHz. The peak surface brightness and contour levels increasing in steps of $2(\sqrt{2})$ for the closeup views of the hot spot regions) are $24.3 \text{ mJy beam}^{-1}$, $(-0.7, 0.7, \dots, 90)\%$ of peak brightness. The lowest contour level in the hot spot blowup is 0.5% of the peak brightness.

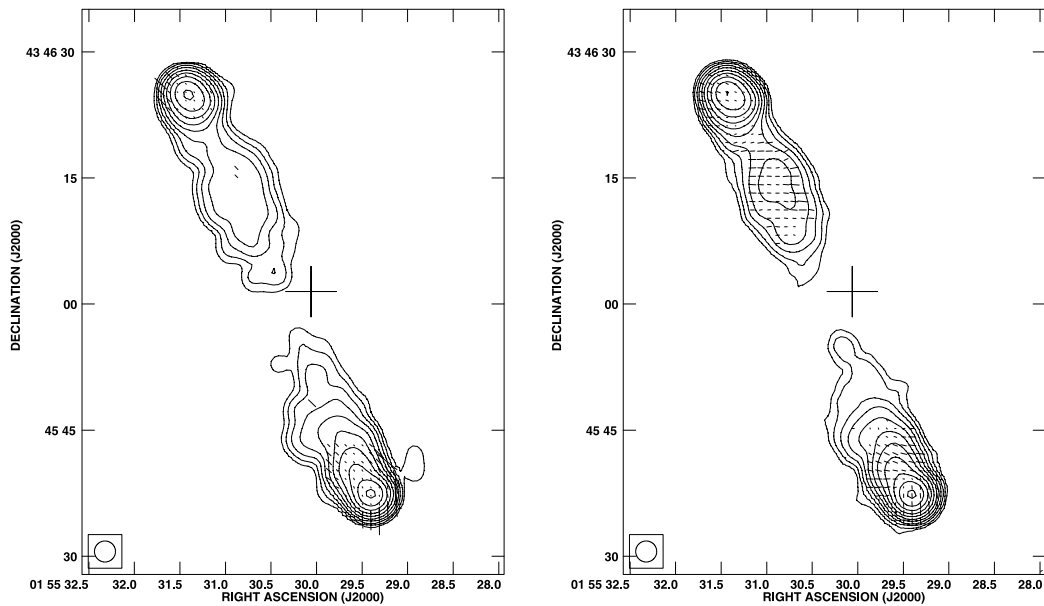


FIG. 26.— Total intensity image of 3C 54 at (left) 1.34 GHz and (right) 4.86 GHz, at a resolution of $2.5''$ with fractional polarization vectors superimposed. The peak surface brightness and contour levels increasing in steps of 2 are (left) $581.9 \text{ mJy beam}^{-1}$, $(-0.17, 0.17, \dots, 90)\%$ of peak brightness, $1''$ vector = 25% polarization, (right) $227.8 \text{ mJy beam}^{-1}$, $(-0.085, 0.085, \dots, 90)\%$ of peak brightness, $1''$ vector = 25% polarization.

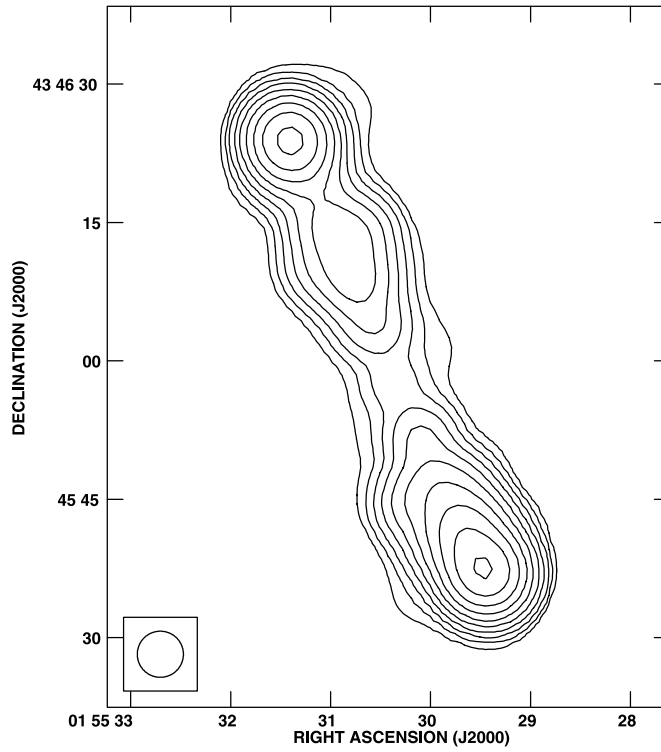


FIG. 27.— Total intensity image of 3C 54 at 327.6 MHz. The peak surface brightness and contour levels increasing in steps of 2 are 2.1 Jy beam^{-1} , $(-0.17, 0.17, \dots, 90)\%$ of peak brightness.

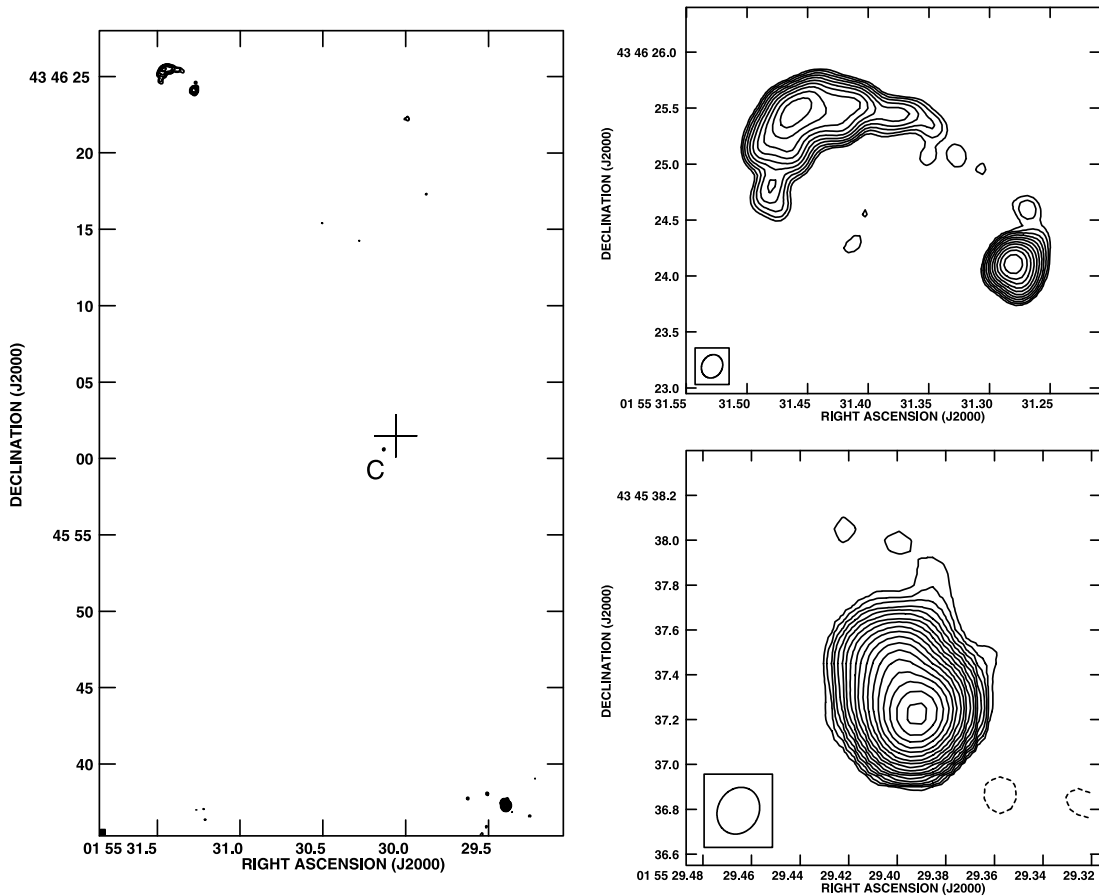


FIG. 28.— Total intensity image of 3C 54 at 8.4 GHz. The peak surface brightness and contour levels increasing in steps of $2(\sqrt{2})$ (for the closeup views of the hot spot regions) are $69.6 \text{ mJy beam}^{-1}$, $(-0.35, 0.35, \dots, 90)\%$ of peak brightness. The lowest contour level in the hot spot blowup is 0.25% of the peak brightness.

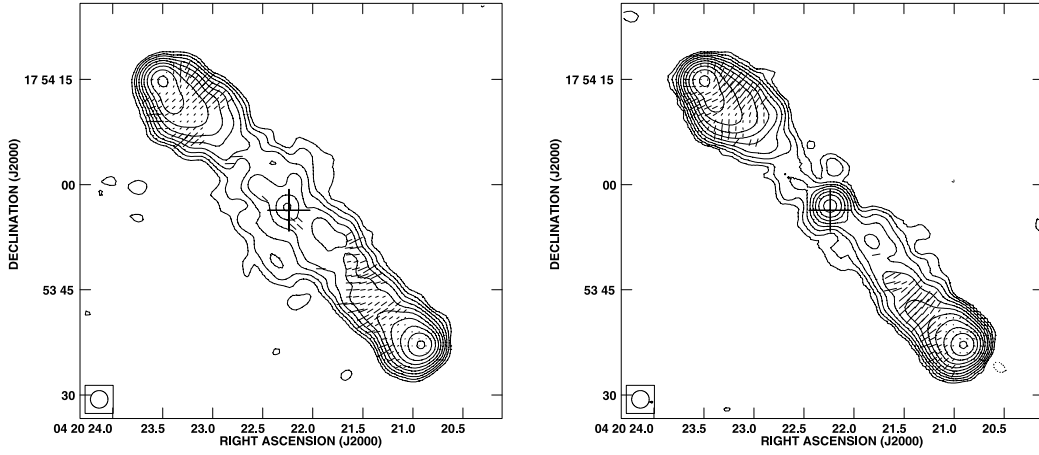


FIG. 29.— Total intensity image of 3C 114 at (*left*) 1.66 GHz and (*right*) 4.86 GHz, at a resolution of $2.5''$ with fractional polarization vectors superimposed. The peak surface brightness and contour levels increasing in steps of 2 are (*left*) $203.7 \text{ mJy beam}^{-1}$, $(-0.17, 0.17, \dots, 90)\%$ of peak brightness, $1''$ vector = 17% polarization, (*right*) $69.5 \text{ mJy beam}^{-1}$, $(-0.085, 0.085, \dots, 90)\%$ of peak brightness, $1''$ vector = 17% polarization.

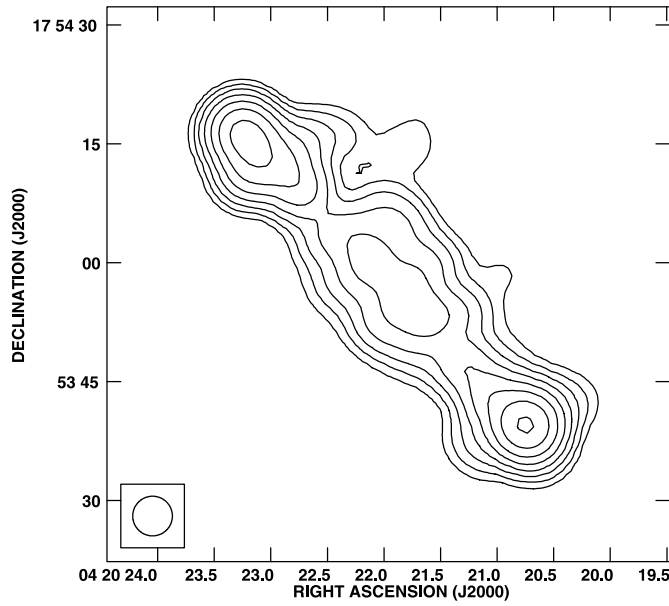


FIG. 30.— Total intensity image of 3C 114 at 327.6 MHz. The peak surface brightness and contour levels increasing in steps of 2 are $898.5 \text{ mJy beam}^{-1}$, $(-0.7, 0.7, \dots, 90)\%$ of peak brightness.

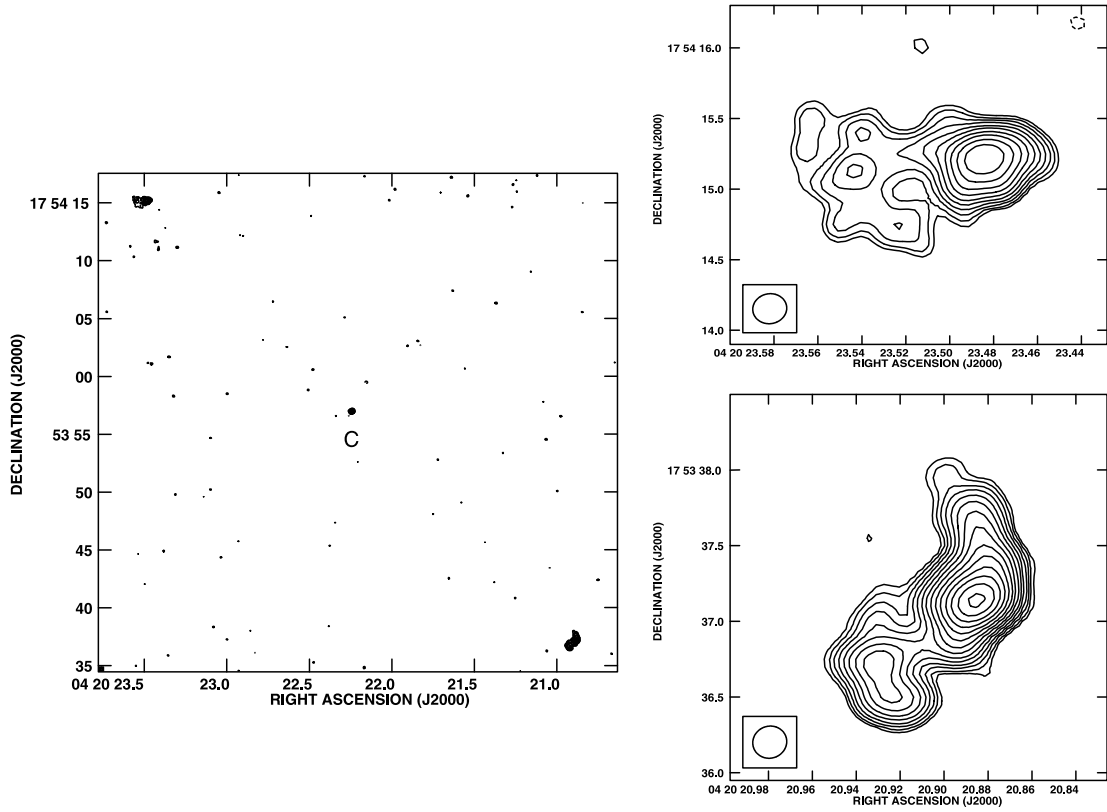


FIG. 31.—Total intensity image of 3C 114 at 8.4 GHz. The peak surface brightness and contour levels increasing in steps of $2(\sqrt{2})$ for the closeup views of the hot spot regions) are $7.3 \text{ mJy beam}^{-1}$, $(-1.4, 1.4, \dots, 90)\%$ of peak brightness. The lowest contour level in the hot spot blowup is 1% of the peak brightness.

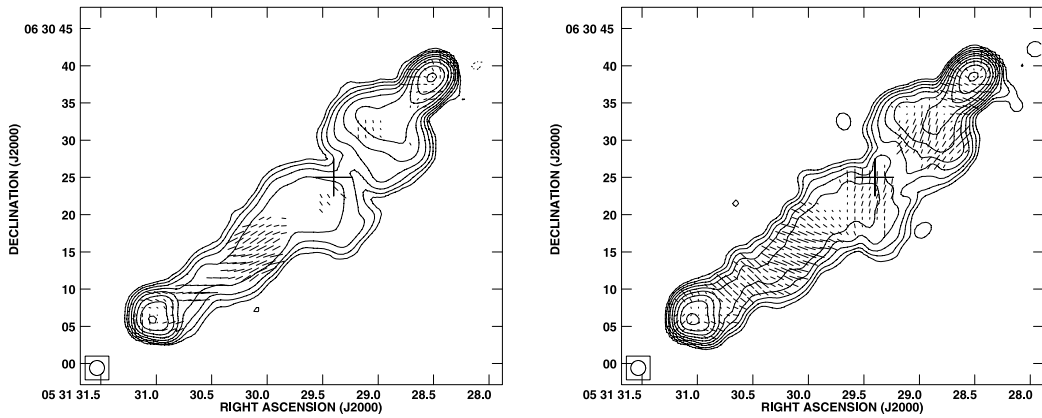


FIG. 32.—Total intensity image of 3C 142.1 at (*left*) 1.34 GHz and (*right*) 4.86 GHz, at a resolution of $2''$ with fractional polarization vectors superimposed. The peak surface brightness and contour levels increasing in steps of 2 are (*left*) $378.8 \text{ mJy beam}^{-1}$, $(-0.35, 0.35, \dots, 90)\%$ of peak brightness, $1''$ vector = 20% polarization, (*right*) $123.0 \text{ mJy beam}^{-1}$, $(-0.17, 0.17, \dots, 90)\%$ of peak brightness, $1''$ vector = 25% polarization.

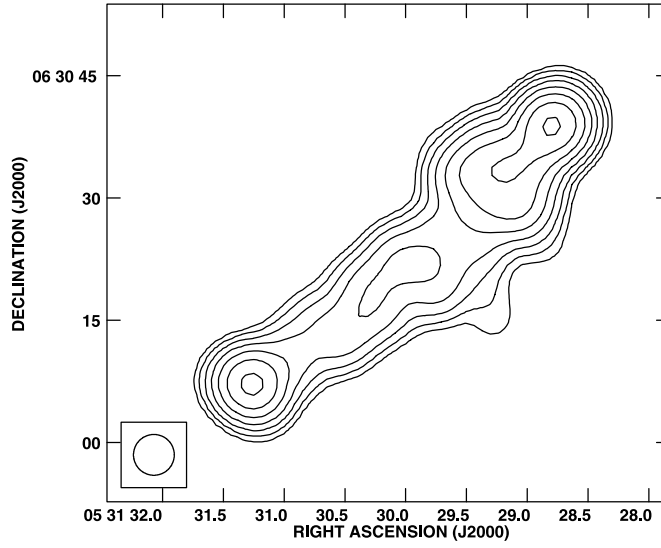


FIG. 33.— Total intensity image of 3C 142.1 at 327.6 MHz. The peak surface brightness and contour levels increasing in steps of 2 are 2.6 Jy beam^{-1} , $(-0.7, 0.7, \dots, 90)\%$ of peak brightness.

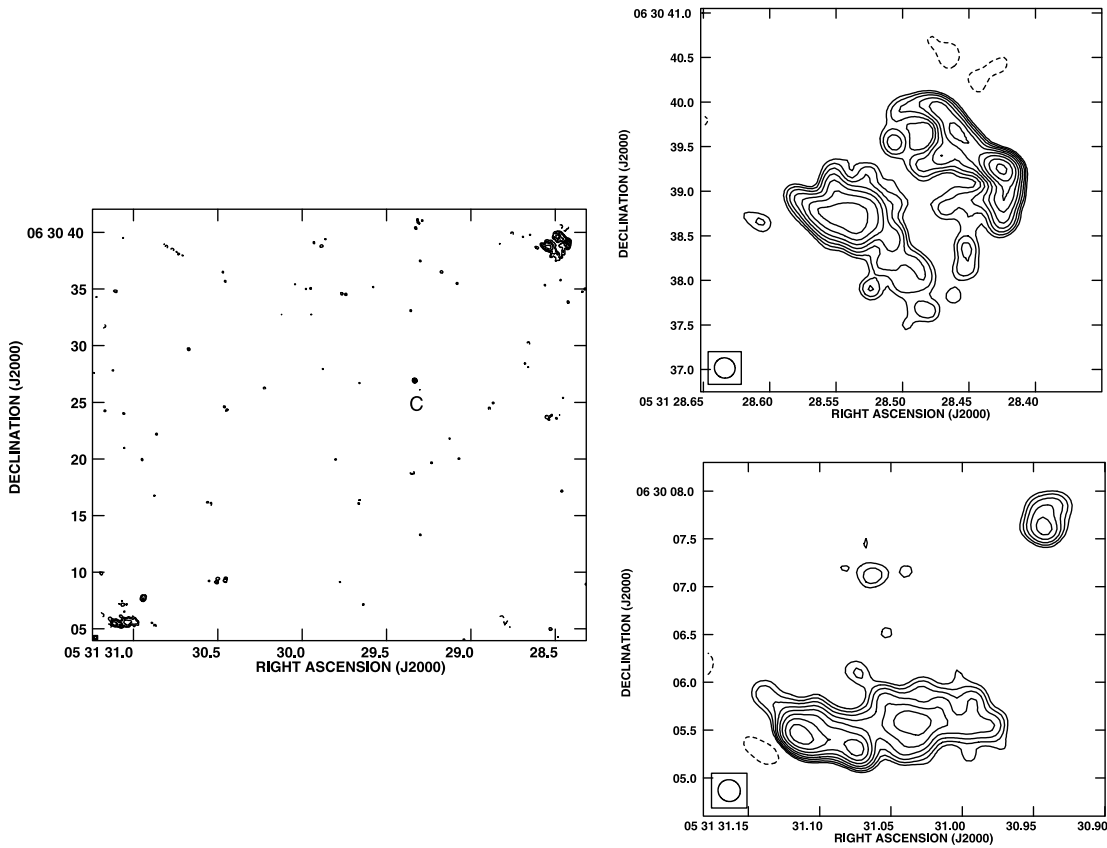


FIG. 34.— Total intensity image of 3C 142.1 at 8.4 GHz. The peak surface brightness and contour levels increasing in steps of $2(\sqrt{2})$ for the closeup views of the hot spot regions are $2.1 \text{ mJy beam}^{-1}$, $(-5.6, 5.6, \dots, 90)\%$ of peak brightness.

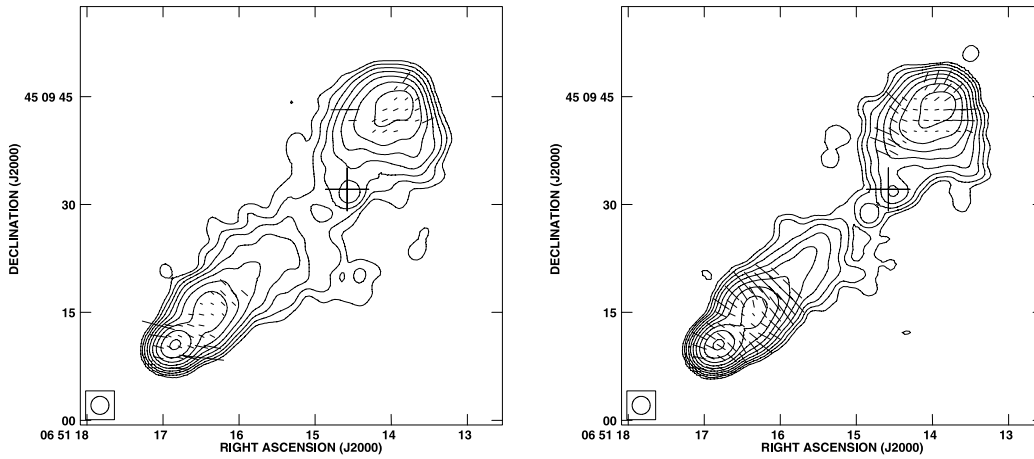


FIG. 35.—Total intensity image of 3C 169.1 at (*left*) 1.66 GHz and (*right*) 4.86 GHz, at a resolution of $2.5''$ with fractional polarization vectors superimposed. The peak surface brightness and contour levels increasing in steps of 2 are (*left*) $153.2 \text{ mJy beam}^{-1}$, $(-0.35, 0.35, \dots, 90\%)$ of peak brightness, $1''$ vector = 10% polarization, (*right*) $56.7 \text{ mJy beam}^{-1}$, $(-0.17, 0.17, \dots, 90\%)$ of peak brightness, $1''$ vector = 10% polarization.

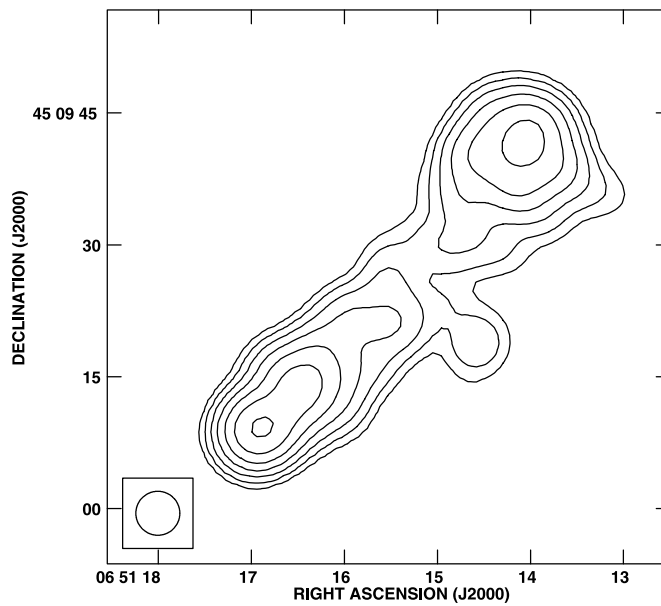


FIG. 36.—Total intensity image of 3C 169.1 at 327.6 MHz. The peak surface brightness and contour levels increasing in steps of 2 are $744.1 \text{ Jy beam}^{-1}$, $(-1.4, 1.4, \dots, 90\%)$ of peak brightness.

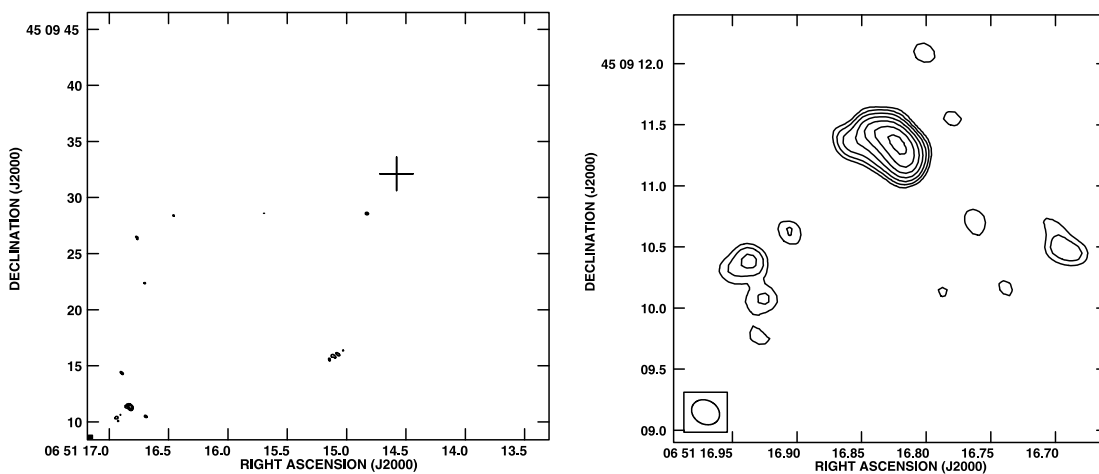


FIG. 37.—Total intensity image of 3C 169.1 at 8.4 GHz. The peak surface brightness and contour levels increasing in steps of 2 ($\sqrt{2}$ for the closeup views of the hot spot regions) are $1.5 \text{ mJy beam}^{-1}$, $(-16, 16, 32, 64)\%$ of peak brightness. The lowest contour level in the hot spot blowup is 11.2% of the peak brightness.

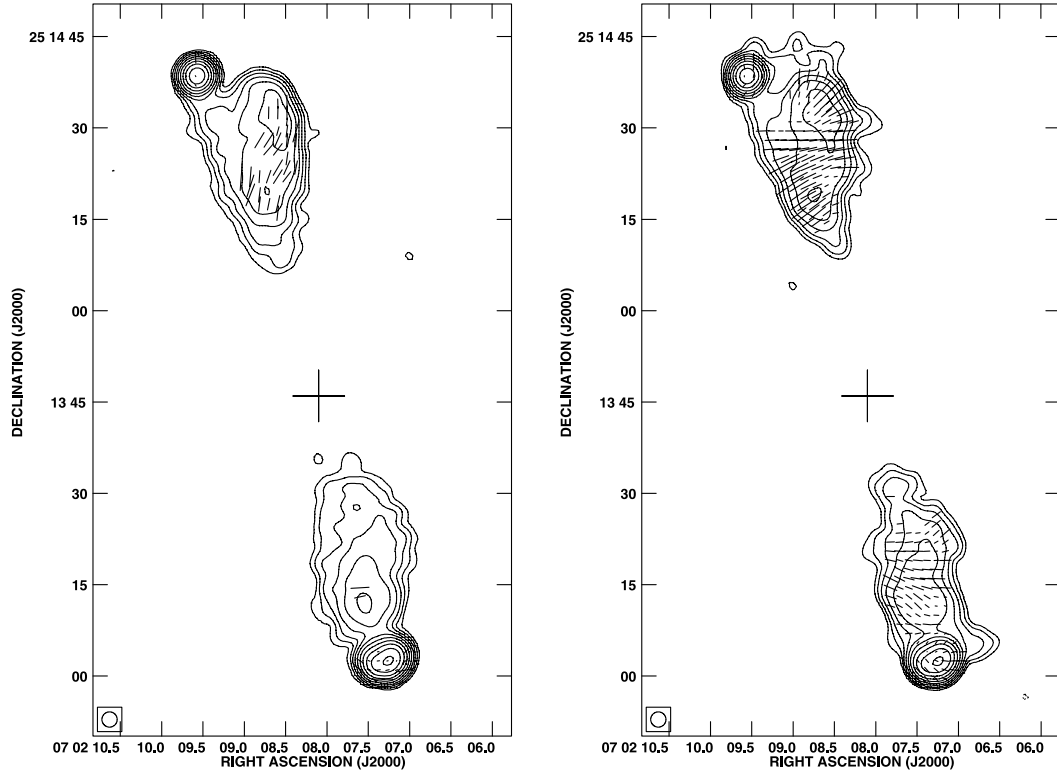


FIG. 38.— Total intensity image of 3C 172 at (*left*) 1.66 GHz and (*right*) 4.86 GHz, at a resolution of $2.5''$ with fractional polarization vectors superimposed. The peak surface brightness and contour levels increasing in steps of 2 are (*left*) $478.1 \text{ mJy beam}^{-1}$, $(-0.17, 0.17, \dots, 90)\%$ of peak brightness, $1''$ vector = 10% polarization, (*right*) $153.7 \text{ mJy beam}^{-1}$, $(-0.17, 0.17, \dots, 90)\%$ of peak brightness, $1''$ vector = 11% polarization.

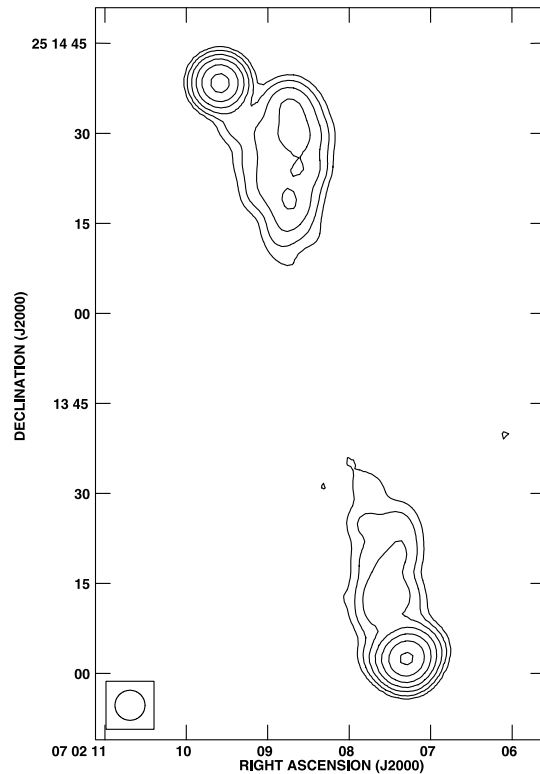


FIG. 39.— Total intensity image of 3C 172 at 327.6 MHz. The peak surface brightness and contour levels increasing in steps of 2 are 2.3 Jy beam^{-1} , $(-1.4, 1.4, \dots, 90)\%$ of peak brightness.

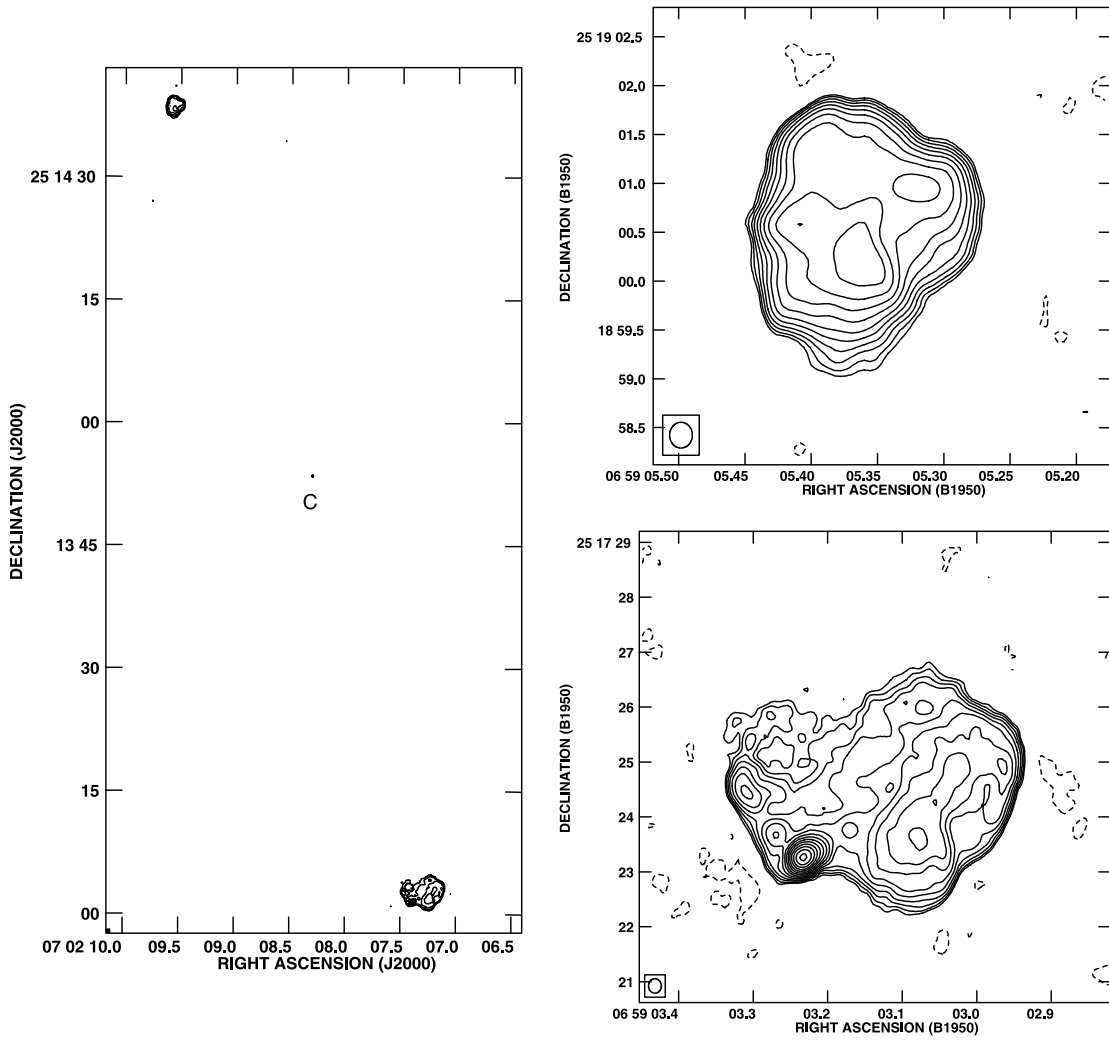


FIG. 40.— Total intensity image of 3C 172 at 8.4 GHz. The peak surface brightness and contour levels increasing in steps of $2 (\sqrt{2})$ (for the closeup views of the hot spot regions) are $11.9 \text{ mJy beam}^{-1}$, $(-1.4, 1.4, \dots, 90)\%$ of peak brightness. The lowest contour level in the hot spot blowup is 1% of the peak brightness.

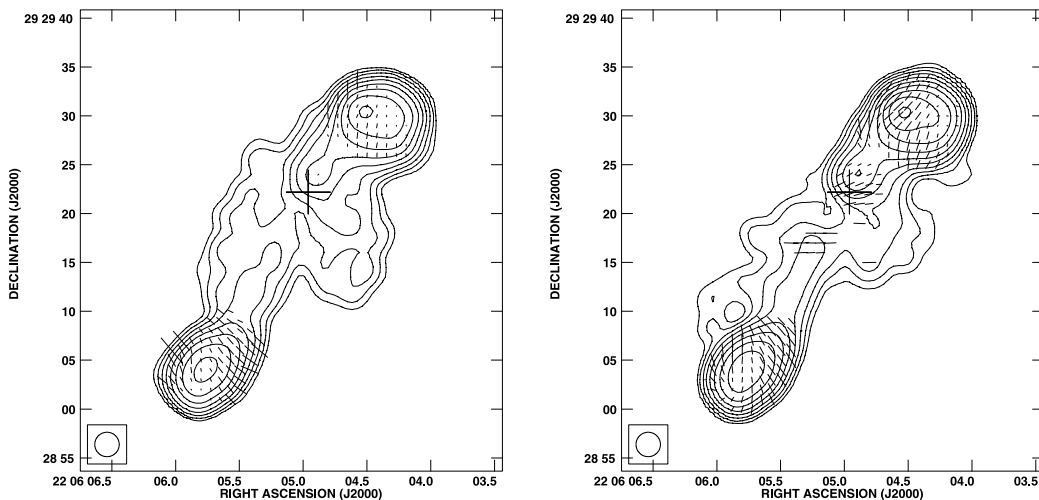


FIG. 41.— Total intensity image of 3C 441 at (left) 1.34 GHz and (right) 4.86 GHz, at a resolution of $2.5''$ with fractional polarization vectors superimposed. The peak surface brightness and contour levels increasing in steps of 2 are (left) $420.1 \text{ mJy beam}^{-1}$, $(-0.35, 0.35, \dots, 90)\%$ of peak brightness, $1''$ vector = 20% polarization, (right) $184.8 \text{ mJy beam}^{-1}$, $(-0.17, 0.17, \dots, 90)\%$ of peak brightness, $1''$ vector = 20% polarization.

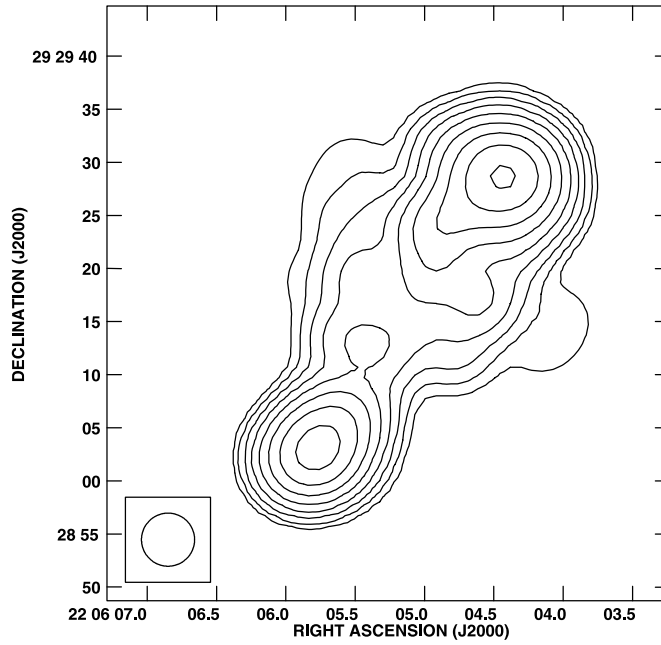


FIG. 42.—Total intensity image of 3C 441 at 327.6 MHz. The peak surface brightness and contour levels increasing in steps of 2 are 2.8 Jy beam^{-1} , $(-0.35, 0.35, \dots, 90)\%$ of peak brightness.

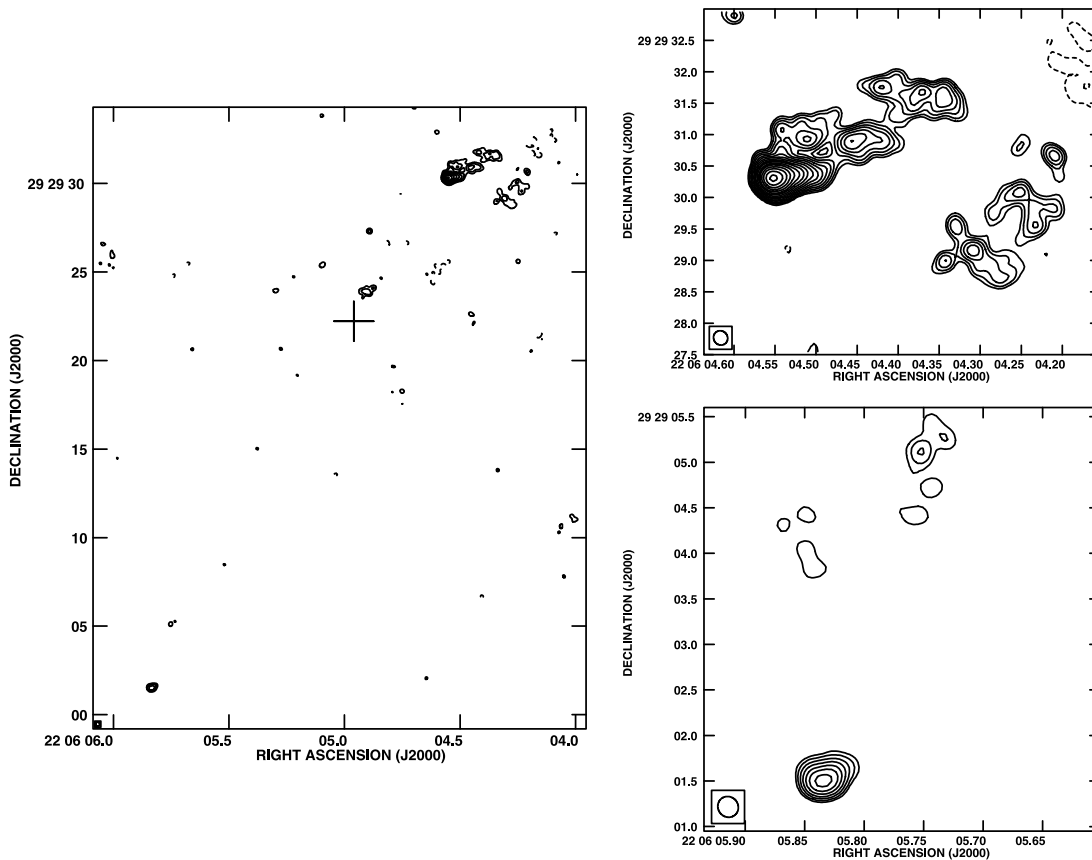


FIG. 43.—Total intensity image of 3C 441 at 8.4 GHz. The peak surface brightness and contour levels increasing in steps of $2(\sqrt{2})$ for the closeup views of the hot spot regions are $33.9 \text{ mJy beam}^{-1}$, $(-0.7, 0.7, \dots, 90)\%$ of peak brightness. The lowest contour level in the hot spot blowup is 0.5% of the peak brightness.

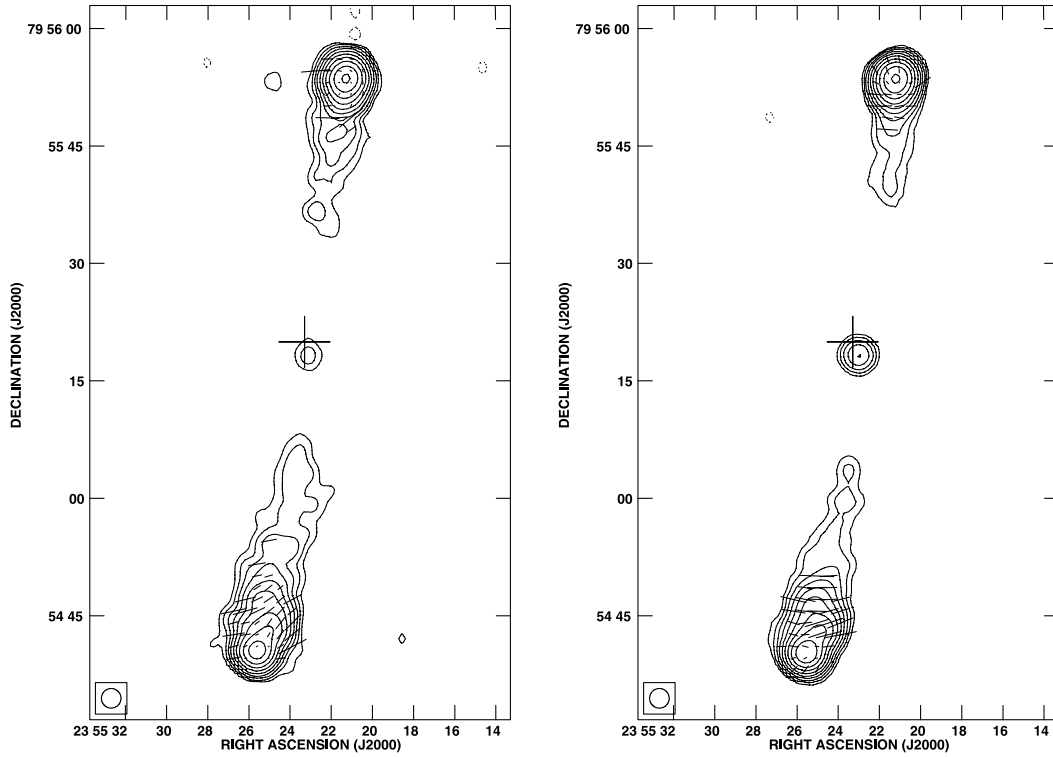


FIG. 44.— Total intensity image of 3C 469.1 at (*left*) 1.34 GHz and (*right*) 4.86 GHz, at a resolution of $2.5''$ with fractional polarization vectors superimposed. The peak surface brightness and contour levels increasing in steps of 2 are (*left*) $559.2 \text{ mJy beam}^{-1}$, $(-0.17, 0.17, \dots, 90)\%$ of peak brightness, $1''$ vector = 12.5% polarization, (*right*) $131.7 \text{ mJy beam}^{-1}$, $(-0.17, 0.17, \dots, 90)\%$ of peak brightness, $1''$ vector = 7% polarization.

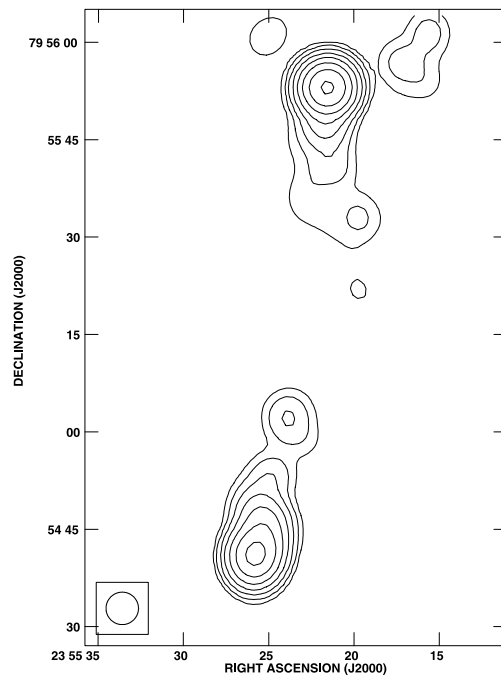


FIG. 45.— Total intensity image of 3C 469.1 at 327.6 MHz. The peak surface brightness and contour levels increasing in steps of 2 are 2.9 Jy beam^{-1} , $(-0.7, 0.7, \dots, 90)\%$ of peak brightness.

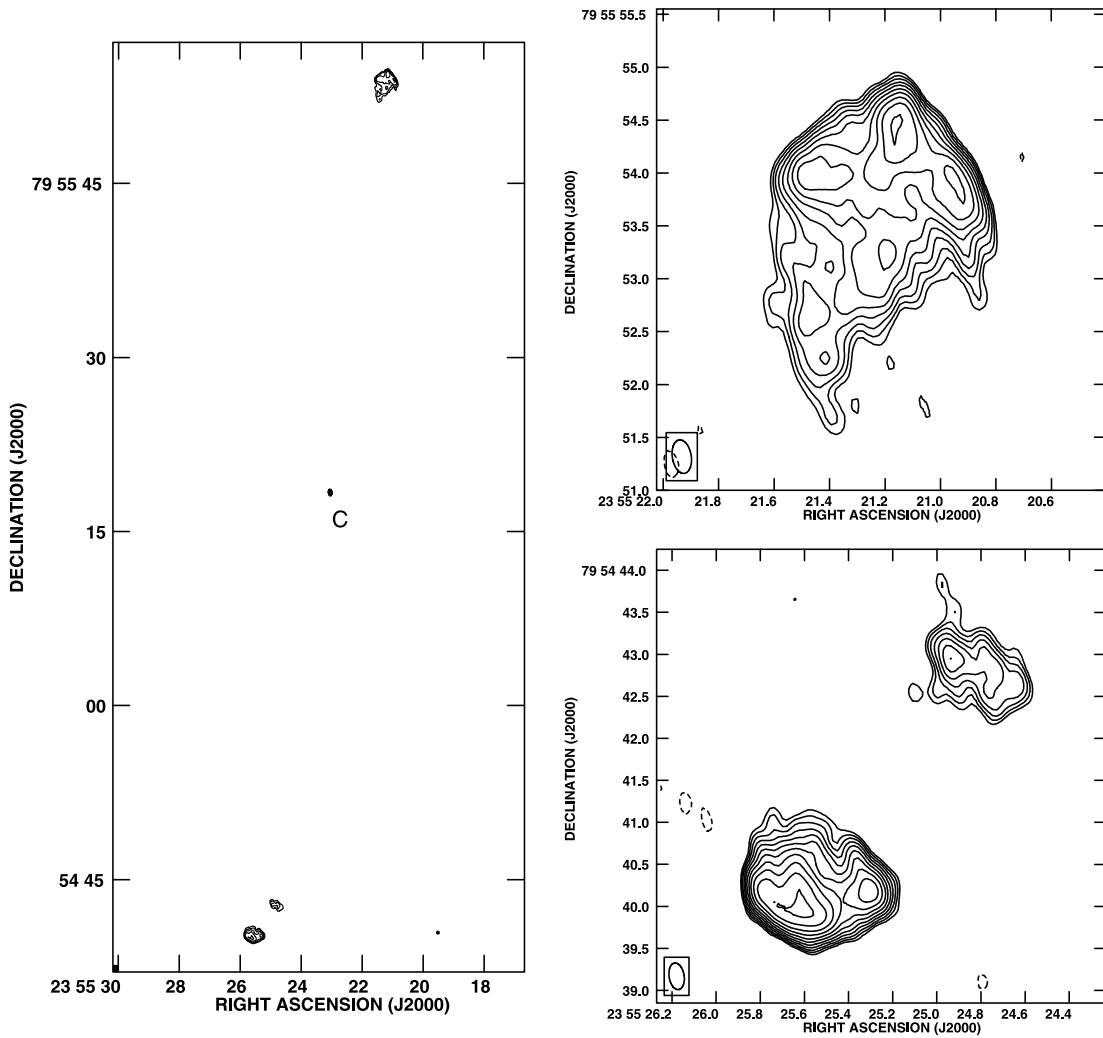


FIG. 46.— Total intensity image of 3C 469.1 at 8.4 GHz. The peak surface brightness and contour levels increasing in steps of $2(\sqrt{2})$ for the closeup views of the hot spot regions) are $4.0 \text{ mJy beam}^{-1}$, $(-5.6, 5.6, \dots, 90)\%$ of peak brightness. The lowest contour level in the hot spot blowup is 2.8% of the peak brightness.

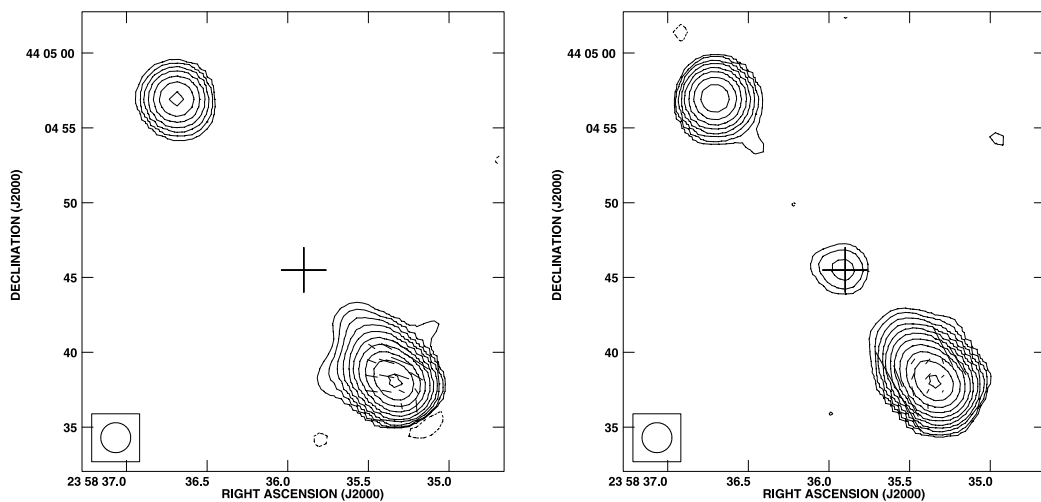


FIG. 47.— Total intensity image of 3C 470 at (*left*) 1.34 GHz and (*right*) 4.86 GHz, at a resolution of $2''$ with fractional polarization vectors superimposed. The peak surface brightness and contour levels increasing in steps of 2 are (*left*) 1.2 Jy beam^{-1} , $(-0.17, 0.17, \dots, 90)\%$ of peak brightness, $1''$ vector = 7.7% polarization, (*right*) $318.8 \text{ mJy beam}^{-1}$, $(-0.085, 0.085, \dots, 90)\%$ of peak brightness, $1''$ vector = 14% polarization.

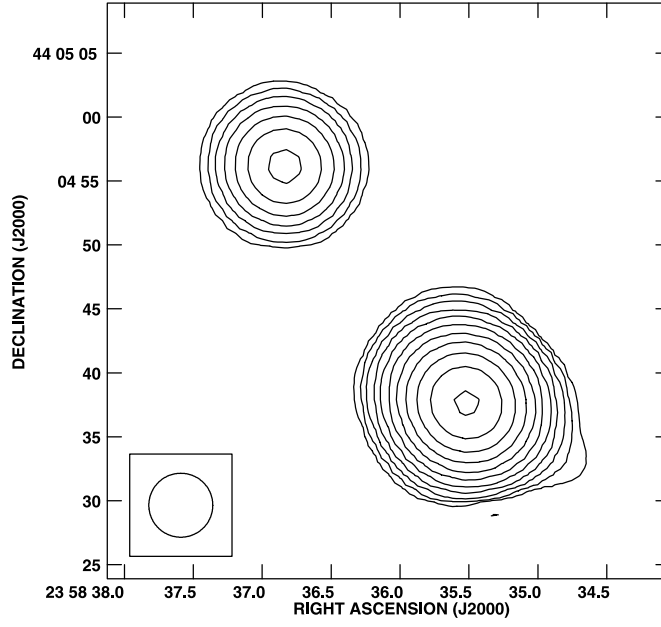


FIG. 48.— Total intensity image of 3C 470 at 327.6 MHz. The peak surface brightness and contour levels increasing in steps of 2 are 5.9 Jy beam^{-1} , $(-0.085, 0.085, \dots, 90)\%$ of peak brightness.

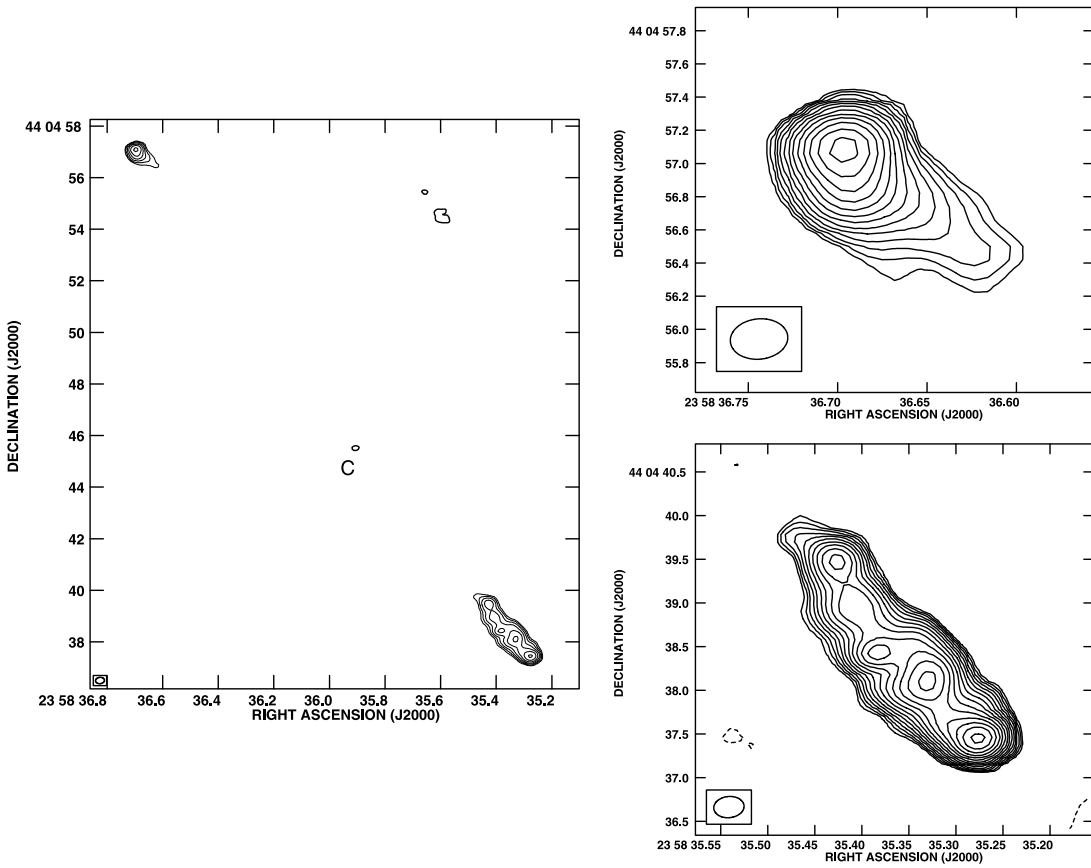


FIG. 49.— Total intensity image of 3C 470 at 8.4 GHz. The peak surface brightness and contour levels increasing in steps of $2(\sqrt{2})$ for the closeup views of the hot spot regions) are $39.9 \text{ mJy beam}^{-1}$, $(-1.4, 1.4, \dots, 90)\%$ of peak brightness. The lowest contour level in the hot spot blowup is 0.7% of the peak brightness.

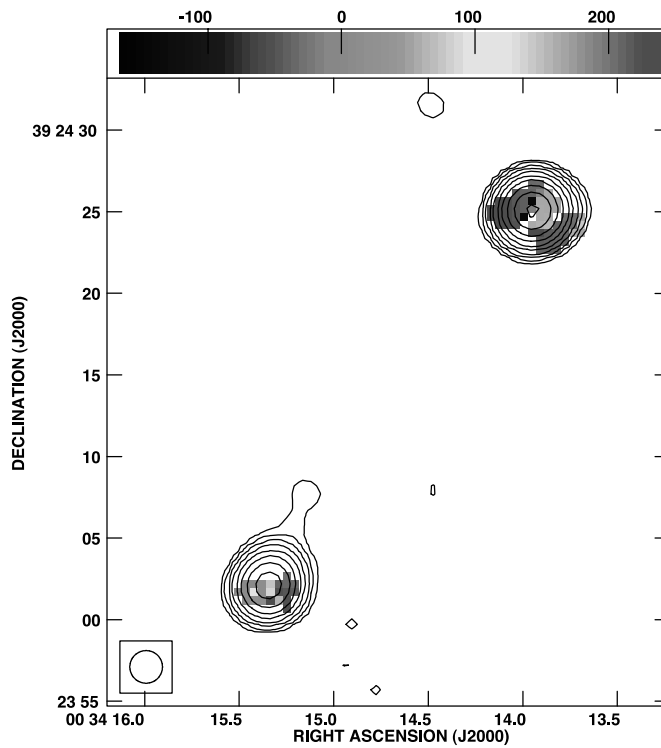


FIG. 50.1

FIG. SET 50.—Rotation measure image in color superimposed by 5 GHz radio contours for 3C 13. The RM was obtained from polarization maps at 1.4 and 5 GHz. The color-scale units are in rad m^2 . [See the electronic edition of the Supplement for Figs. 50.1–50.11]

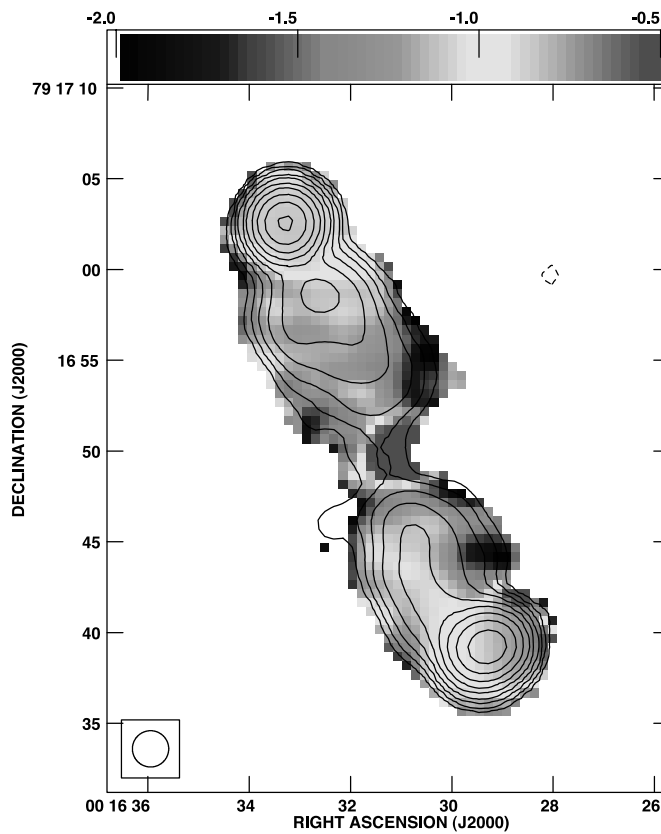


FIG. 51.1

FIG. SET 51.—Spectral index image in color superimposed by 1.4 GHz radio contours at a resolution of $\sim 2''$ for 3C 6.1. The spectral index image was obtained with 1.4 and 5 GHz data. [See the electronic edition of the Supplement for Figs. 51.1–51.24.]

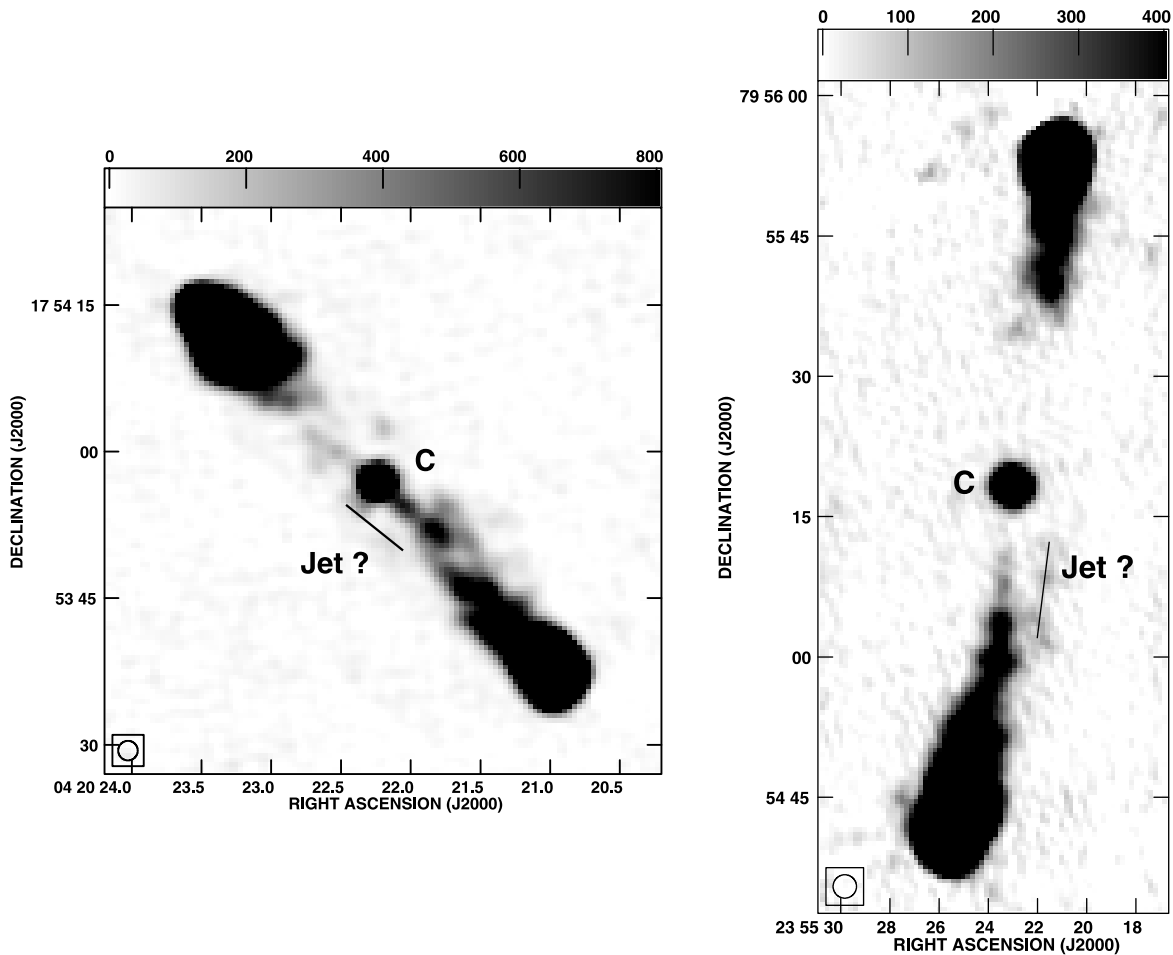


FIG. 52.—The 5 GHz gray-scale image of (left) 3C 114 and (right) 3C 469.1, showing the jetlike feature.

position indicated by the brightest hot spot. The bridge seems to exhibit a type LW3 lobe morphology. The 5 GHz gray scale image shows a jetlike feature extending toward the northern hot spot.

3C 469.1.—The *HST* observations of McCarthy et al. (1997) find that the host galaxy of 3C 469.1 shows a double structure at P.A. 95° , not aligned with the radio axis. We detect a bright radio core in this source but not sufficient radio bridge emission (Fig. 44). The source is at a redshift of $z = 1.336$, and more sensitive observations are needed to observe the full bridge region in the source. 3C 469.1 shows a jetlike feature extending toward the southern hot spot in the 5 GHz image.

3C 470.—Best et al. (1998) find that the host galaxy of 3C 470 is slightly extended in both the optical and the *K*-band images, with the elongation being highly misaligned (by 80°) with the radio axis. We find that the radio bridge in 3C 470 is partly visible only on the southern side (Fig. 44). This is the highest redshift object in our sample ($z = 1.653$). Therefore, more sensitive observations are required to observe the full bridge region. We detect a radio core at the position R.A. = $23^{\text{h}}58^{\text{m}}35.9063^{\text{s}}$, decl. = $44^\circ04'45.5180''$. 3C 470 shows a slight extension in the radio core toward the southern hot spot in the 5 GHz image.

REFERENCES

- Alexander, P. 1987, *MNRAS*, 225, 27
 Alexander, P., & Leahy, J. P. 1987, *MNRAS*, 225, 1
 Athreya, R. M., & Kapahi, V. K. 1999, in *The Most Distant Radio Galaxies*, ed. H. J. A. Röttgering, P. N. Best, & M. D. Lehnert (Amsterdam: R. Netherlands Acad.), 453
 Baars, J. W. M., Genzel, R., Pauliny-Toth, I. I. K., & Witzel, A. 1977, *A&A*, 61, 99
 Baldwin, J. E., & Scott, P. F. 1973, *MNRAS*, 165, 259
 Barthel, P. D., & Miley, G. K. 1988, *Nature*, 333, 319
 Begelman, M. C., Blandford, R. D., & Rees, M. J. 1984, *Rev. Mod. Phys.*, 56, 255
 Begelman, M. C., & Cioffi, D. F. 1989, *ApJ*, 345, L21
 Bennett, A. S. 1962, *MmRAS*, 68, 163
 Best, P. N., Bailer, D. M., Longair, M. S., & Riley, J. M. 1995, *MNRAS*, 275, 1171
 Best, P. N., Longair, M. S., & Röttgering, H. J. A. 1997a, *MNRAS*, 292, 758
 ———. 1997b, *MNRAS*, 286, 785
 ———. 1998, *MNRAS*, 295, 549
 Best, P. N., Röttgering, H. J. A., & Longair, M. S. 2000, *MNRAS*, 311, 23
 Blundell, K. M., Rawlings, S., & Willott, C. J. 1999, *AJ*, 117, 677
 Bogers, W. J., Hes, R., Barthel, P. D., & Zensus, J. A. 1994, *A&AS*, 105, 91
 Bridle, A. H., Hough, D. H., Lonsdale, C. J., Burns, J. O., & Laing, R. A. 1994, *AJ*, 108, 766
 Carilli, C. L., Perley, R. A., Dreher, J. W., & Leahy, J. P. 1991, *ApJ*, 383, 554
 Carvalho, J. C., O’Dea, C. P. 2002a, *ApJS*, 141, 337
 ———. 2002b, *ApJS*, 141, 371
 Chambers, K. C., Miley, G. K., & van Breugel, W. J. M. 1990, *ApJ*, 363, 21
 Daly, R. A. 1990, *ApJ*, 355, 416
 De Breuck, C., van Breugel, W., Röttgering, H. J. A., & Miley, G. 2000, *A&AS*, 143, 303
 Dennett-Thorpe, J., Bridle, A. H., Laing, R. A., & Scheuer, P. A. G. 1999, *MNRAS*, 304, 271
 Dennett-Thorpe, J., Bridle, A. H., Scheuer, P. A. G., Laing, R. A., & Leahy, J. P. 1997, *MNRAS*, 289, 753
 Fanaroff, B. L., & Riley, J. M. 1974, *MNRAS*, 167, 31P

- Fernini, I., Burns, J. O., & Perley, R. A. 1997, *AJ*, 114, 2292
- Garrington, S. T., Conway, R. G., & Leahy, J. P. 1991, *MNRAS*, 250, 171
- Garrington, S. T., Leahy, J. P., Conway, R. G., & Laing, R. A. 1988, *Nature*, 331, 147
- Gilbert, G. M., Riley, J. M., Hardcastle, M. J., Croston, J. H., Pooley, G. G., & Alexander, P. 2004, *MNRAS*, 351, 845
- Goodlet, J. A., & Kaiser, C. R. 2005, *MNRAS*, 359, 1456
- Goodlet, J. A., Kaiser, C. R., Best, P. N., & Dennett-Thorpe, J. 2004, *MNRAS*, 347, 508
- Gopal-Krishna. 1988, *A&A*, 192, 37
- Gopal-Krishna, & Wiita, P. J. 2004, preprint (astro-ph/0409761)
- Gower, J. F. R., Scott, P. F., & Wills, D. 1967, *MmRAS*, 71, 49
- Hardcastle, M. J., Alexander, P., Pooley, G. G., & Riley, J. M. 1998, *MNRAS*, 296, 445
- Hes, R., Barthel, P. D., & Fosbury, R. A. E. 1996, *A&A*, 313, 423
- Hough, D. H., & Readhead, A. C. S. 1989, *AJ*, 98, 1208
- Inskip, K. J., Best, P. N., Rawlings, S., Longair, M. S., Cotter, G., Röttgering, H. J. A., & Eales, S. 2002, *MNRAS*, 337, 1381
- Ishwara-Chandra, C. H., & Saikia, D. J. 2000, *MNRAS*, 317, 658
- Ishwara-Chandra, C. H., Saikia, D. J., McCarthy, P. J., & van Breugel, W. J. M. 2001, *MNRAS*, 323, 460
- Jackson, N., & Rawlings, S. 1997, *MNRAS*, 286, 241
- Johnson, R. A., Leahy, J. P., & Garrington, S. T. 1995, *MNRAS*, 273, 877
- Kaiser, C. R., & Alexander, P. 1997, *MNRAS*, 286, 215
- Kapahi, V. K., & Kulkarni, V. K. 1990, *AJ*, 99, 1397
- Kapahi, V. K., & Saikia, D. J. 1982, *J. Astrophys. Astron.*, 3, 465
- Klamer, I. J., Ekers, R. D., Bryant, J. J., Hunstead, R. W., Sadler, E. M., & De Breuck, C. 2006, *MNRAS*, 371, 852
- Krolik, J. H., & Chen, W. 1991, *AJ*, 102, 1659
- Kronberg, P. P., Conway, R. G., & Gilbert, J. A. 1972, *MNRAS*, 156, 275
- Kuehr, H., Witzel, A., Pauliny-Toth, I. I. K., & Nauber, U. 1996, *VizieR Online Data Catalog*, 8005, 0
- Lacy, M., Hill, G. J., Kaiser, M. E., & Rawlings, S. 1993, *MNRAS*, 263, 707
- Laing, R. 1989, *Hot Spots in Extragalactic Radio Sources (Lecture Notes in Phys. 327; Berlin: Springer)*, 27
- . 1981, *MNRAS*, 195, 261
- . 1988, *Nature*, 331, 149
- . 1993, in *Sub-Arcsecond Radio Astronomy*, ed. R. J. Davis & R. S. Booth (Cambridge: Cambridge Univ. Press), 346
- . 1996, in *IAU Symp. 175, Extragalactic Radio Sources*, ed. R. D. Ekers, C. Fanti, & L. Padrielli (Dordrecht: Kluwer), 147
- Laing, R. A., & Peacock, J. A. 1980, *MNRAS*, 190, 903
- Laing, R. A., Riley, J. M., & Longair, M. S. 1983, *MNRAS*, 204, 151
- Law-Green, J. D. B., Leahy, J. P., Alexander, P., Allington-Smith, J. R., van Breugel, W. J. M., Eales, S. A., Rawlings, S. G., & Spinrad, H. 1995, *MNRAS*, 274, 939
- Leahy, J. P. 1987, *MNRAS*, 226, 433
- Leahy, J. P., Muxlow, T. W. B., & Stephens, P. W. 1989, *MNRAS*, 239, 401
- Leahy, J. P., & Williams, A. G. 1984, *MNRAS*, 210, 929
- Liu, R., & Pooley, G. 1991a, *MNRAS*, 249, 343
- . 1991b, *MNRAS*, 253, 669
- Liu, R., Pooley, G., & Riley, J. M. 1992, *MNRAS*, 257, 545
- Longair, M. S. 1975, *MNRAS*, 173, 309
- MacDonald, G. H., Kenderdine, S., & Neville, A. C. 1968, *MNRAS*, 138, 259
- Macklin, J. T. 1981, *MNRAS*, 196, 967
- McCarthy, P. J. 1993, *ARA&A*, 31, 639
- McCarthy, P. J., Miley, G. K., de Koff, S., Baum, S. A., Sparks, W. B., Golombek, D., Biretta, J., & Macchetto, F. 1997, *ApJS*, 112, 415
- McCarthy, P. J., Spinrad, H., & van Breugel, W. 1995, *ApJS*, 99, 27
- McCarthy, P. J., & van Breugel, W. 1989, in *Extranuclear Activity in Galaxies*, ed. E. J. A. Merus & R. A. E. Fosbury (Garching: ESO), 55
- McCarthy, P. J., van Breugel, W., & Kapahi, V. K. 1991, *ApJ*, 371, 478
- Morris, D., & Tabara, H. 1973, *PASJ*, 25, 295
- Mullin, L. M., Hardcastle, M. J., & Riley, J. M. 2006, *MNRAS*, 372, 113
- Myers, S. T., & Spangler, S. R. 1985, *ApJ*, 291, 52
- Napier, P. J., Thompson, A. R., & Ekers, R. D. 1983, *IEEE Proc.*, 71, 1295
- Neff, S. G., Roberts, L., & Hutchings, J. B. 1995, *ApJS*, 99, 349
- Orr, M. J. L., & Browne, I. W. A. 1982, *MNRAS*, 200, 1067
- Pederty, J. A., Rudnick, L., McCarthy, P. J., & Spinrad, H. 1989, *AJ*, 97, 647
- Perley, R. A., & Taylor, G. B. 1991, *AJ*, 101, 1623
- Perucho, M., Martí J. M. 2003, *Publ. Astron. Soc. Australia*, 20, 94
- Pooley, G. G., & Henbest, S. N. 1974, *MNRAS*, 169, 477
- Privon, G. C., O'Dea, C. P., Baum, S. A., Axon, D. J., Kharb, P., Buchanan, C. L., Sparks, W., & Chiaberge, M. 2008, *ApJS*, in press
- Rees, M. J., & Setti, G. 1968, *Nature*, 219, 127
- Riley, J. M., & Pooley, G. G. 1975, *MmRAS*, 80, 105
- Roger, R. S., Costain, C. H., & Bridle, A. H. 1973, *AJ*, 78, 1030
- Scheuer, P. A. G. 1982, in *IAU Symp. 97, Extragalactic Radio Sources Morphology and Power of Radio Sources*, ed. D. S. Heeschen & C. M. Wade (Dordrecht: Reidel), 163
- Schilizzi, R. T., Kapahi, V. K., & Neff, S. G. 1982, *J. Astrophys. Astron.*, 3, 173
- Schwab, F. R. 1980, *Proc. SPIE*, 231, 18
- Simard-Normandin, M., Kronberg, P. P., & Button, S. 1981, *ApJS*, 45, 97
- Simonetti, J. H., Cordes, J. M., & Spangler, S. R. 1984, *ApJ*, 284, 126
- Spinrad, H. 1986, *PASP*, 98, 269
- Strom, R. G., & Conway, R. G. 1985, *A&AS*, 61, 547
- Strom, R. G., Riley, J. M., Spinrad, H., van Breugel, W. J. M., Djorgovski, S., Liebert, J., & McCarthy, P. J. 1990, *A&A*, 227, 19
- Tribble, P. C. 1991, *MNRAS*, 250, 726
- Wardle, J. F. C., & Kronberg, P. P. 1974, *ApJ*, 194, 249
- Wellman, G. F., Daly, R. A., & Wan, L. 1997, *ApJ*, 480, 96
- Williams, A. G., & Gull, S. F. 1985, *Nature*, 313, 34